

**THE DEVELOPMENT AND FABRICATION OF PARTICLE
DETECTORS USING FUSED DEPOSITION MODELLING
TECHNIQUES**



SAMUEL JAMES FARGHER
MPHYS

Supervisor: Prof. Lee F. Thompson

Department of Physics and Astronomy
The University of Sheffield

A thesis submitted in fulfilment of the requirements for the degree of
Doctor of Philosophy in Physics

October 2019

Acknowledgements

First and foremost, I would like to express my immense gratitude to Professor Lee Thompson, who took me on as a summer project student in 2014 assembling particle detectors, sparking my interest in the field of HEPP instrumentation, and has been my supervisor ever since; in both my Master's project and throughout this PhD. Lee has consistently presented me with exciting opportunities to pursue; supported and encouraged new ideas to be investigated; and has displayed an unbelievable amount of patience and understanding throughout all. Without Lee I would not be the physicist I am today and I am excited to continue working with him in the future.

A special thank you goes to Patrick Stowell, who I have had the greatest pleasure of working alongside this past year. Patrick has been an incredible source of inspiration, collaboration and, most importantly, general mischief. Together we have exchanged knowledge; conceived new detector concepts; and significantly distracted each other with exciting, new ideas. The research in this thesis would not have reached the stage it has without him.

While the majority of the work in this thesis has been completed in a solo effort, I must acknowledge the support, advice and contributions from Andrew Parnell in the developments made towards a printable plastic scintillator. Andy's knowledge, expertise and sheer willingness to help others has proved invaluable and, for this, I am truly grateful.

Many thanks are given to my friends, housemates and fellow PhD students, both old and new. You have provided me with the most amazing times, social affairs and general support. I have had some incredible experiences throughout my PhD, many of them shaping who I am today, and you're all partially responsible; it is appreciated! Honourable mentions go to Jack, Jake, Dom, Charlotte, Henry, Ross, Ellie, Joe, Katie, Joe, Jess, Mary, RT, Pfitz, Jordan and Tammy for being there through it all.

Next, I would like to express how grateful I am to Emma, for being an amazing source of much-needed distractions, for the endless laughter she provides, and for the undeniable influence she has had on myself. I can only hope to support her through her thesis as she has done for me through mine.

Last but not least, I would like to give thanks to my family for their unconditional love and support throughout my life. I am especially thankful to my parents, who have always strived to provide me with the best opportunities possible and never pushed me in any direction; allowing me to follow my own interests and to chose my own path, but consistently being there to help guide me along the way. Thank you.

The work in this thesis was funded by AWE, plc.

Ministry of Defence ©British Crown Owned Copyright 2020/AWE

Abstract

The recent developments made in Additive Manufacturing (AM) technologies, and the printable materials available, have increased the scope of AM fabrication techniques beyond merely producing prototype models and towards manufacturing viable, operational devices. Fused Deposition Modelling (FDM), an AM technique available at The University of Sheffield, has been investigated as a means of producing simple particle detectors, with the aim to create a method of 3D printing operational Single Wire Gaseous Detectors (SWGDs) which minimises the need for human interference. Multiple FDM printers and thermoplastics have been assessed as viable options for this work with open-source, large-scale printers, such as the Gigabot from re:3D, deemed the most appropriate, and uncoloured Polylactic Acid (PLA), lacking excessive additives, found to be the best option currently available. An investigation into the available techniques for creating cathode structures has been performed, with conductive PLA used to produce cylindrical cathodes, as well as some development towards novel detector designs, i.e. a tessellating, triangular gaseous detector for muon tracking. Four SWGDs have been produced using the FDM process, and were successfully operated over a range of applied bias voltages to detect cosmic ray muons and β -particles from a strontium-90 source. A selection algorithm was created to determine signals from the detectors, and analyse the data, enabling the responses of the detectors to be characterised. Initial steps towards the fabrication of a printable plastic scintillator have been completed, as has some work towards 3D printed readout patterns. Work in these fields could yield interesting, novel designs, however, development in these areas is still in its infancy.

Contents

1	Introduction	1
1.1	The Foundations of HEPP Instrumentation	1
1.1.1	Detector Development	1
1.1.2	Gaseous Detectors	4
1.1.3	Scintillators	5
1.2	Motivation for Low-Cost Solutions to HEPP Instrumentation	8
1.2.1	3D Printing Detectors	8
1.3	Summary: Aims of this Thesis	13
2	Theory of Detection	15
2.1	Gaseous Detectors	15
2.1.1	Principles of Operation	15
2.1.2	Types of Gaseous Detectors	21
2.2	Plastic Scintillators	26
2.2.1	Principles of Operation	26
3	3D Printed Gas-Tight Enclosures: Printers and Plastics	31
3.1	Makerbot: Enclosure Geometries	31
3.2	Makerbot: Introducing Anode Wires	36
3.3	Makerbot: Printer Limitations and The Requirements For Change	40
3.4	Gigabot: Enclosure Geometries	41
3.4.1	Tessellating, Triangular Tubes	44
3.4.2	Nozzles, Resolutions and The Volcano	46
3.5	Gigabot: Introducing Anode Wires	48
3.5.1	Alternative Thermoplastics	50
3.6	Low Background PLA: Gamma Spectroscopic Analysis	53
3.7	Gigabot: Gas-Tight Enclosures	57

3.7.1	Wired Gas-Tight Enclosure	64
3.8	Chapter Summary	65
4	Operational Detectors: The First 3D Printed Single-Wire Gaseous Detectors	67
4.1	The First Single-Wire Gaseous Detectors	67
4.1.1	Detector V1: Design and Data Collection	68
4.1.2	Detector V1: Results	72
4.2	The Upgraded SWGD	72
4.2.1	Detector V1.1: Design and Data Collection	73
4.2.2	Python: Selection Algorithm	77
4.2.3	Detector V1.1: Results	81
4.3	Chapter Summary	87
5	Operational Detectors: Cathode Development and Cylindrical Geometries	89
5.1	Available Techniques for Cathode Development	89
5.1.1	Technique Assessment	90
5.1.2	Conclusion	92
5.2	Printing With Conductive PLA	94
5.2.1	Preliminary Cathode Structures	96
5.3	Cuboidal-Cylindrical Cathodes	99
5.3.1	Detector V2: Design and Data Collection	99
5.3.2	Detector V2: Results	103
5.3.3	Detector V2: Muon Detection Results	107
5.3.4	Detector V2: Detector Summary	110
5.4	Triangular Insert, Cylindrical Cathode	113
5.4.1	Detector V3: Design and Data Collection	113
5.4.2	Detector V3: Results	116
5.4.3	Detector V3: Detector Summary	118
6	Operational Detectors: Novel Triangular Cathode Design and The Muon Tracker	121
6.1	Muon Tracker: Concept Design	121
6.2	Triangular Inserts, Graded Cathodes	124
6.2.1	Detector V4: Design and Data Collection	124

6.2.2	Detector V4: Results	128
6.3	Initial Tracking Tests	132
6.3.1	Tracker Test: Results	134
6.4	Chapter Summary	134
7	Thermoplastic Scintillator Filament and Other Additional Gaseous	
	Detectors	137
7.1	Thermoplastic Scintillator Filament	137
7.1.1	Initial Developmental Stages	138
7.1.2	Flexible Plastic Scintillator	142
7.1.3	Flexible Scintillator Summary	148
7.2	Time Projection Chambers, Readout Strips and Resistive Plate	
	Chambers	149
8	Concluding Remarks	151

Chapter 1

Introduction

The nuclear decay of radon in the air we breathe, the passing of cosmic ray muons through our bodies, the pair-production and subsequent annihilation of an electron-positron pair created from the sea of gamma-rays that constantly surround us; the vast majority of natural phenomena in the world goes widely unnoticed and, prior to the late 19th century, were extensively unknown. Only through the invention and development of particle detectors and instrumentation have the mysteries of the subatomic realm been discovered and investigated, leading to the current state of particle physics.

1.1 The Foundations of HEPP Instrumentation

1.1.1 Detector Development

The beginning of modern particle physics is commonly attributed to W.C. Röntgen. In 1895, Röntgen accidentally discovered x-rays emitting from a Crookes tube after noticing flashes of fluorescence from a square of cardboard coated with Barium Platinocyanide [1]. Röntgen continued to experiment with x-rays finding calcium sulphide, uranium glass, Iceland spar and rock-salt also fluoresced when exposed and photographic plates would darken; these were the first particle detectors, leading Röntgen to win the first Nobel Prize in Physics in 1901, and instigated further research into x-rays to discover other scintillating compounds and the development of discharge tubes. The former leading to Thomas Edison to develop the fluoroscope after discovering Calcium Tungstate as a scintillator in 1896 [2], and the latter leading to the invention of the Cathode Ray Tube, by Ferdinand Braun in 1897 [3]

and the subsequent discovery of the electron by J. J. Thomson in the same year [4].

In 1896, following W.C. Röntgen's discovery, Henri Becquerel accidentally discovered natural radioactivity. Becquerel had observed photographic plates darken after being exposed to potassium uranyl sulphate and, unknowingly at the time, detected the decay products of the uranium in the compound; initiating future investigations into radioactivity, the structure of the atom and the development of particle detectors [5].

Many physicists, including Becquerel, investigated the newly discovered radioactivity using phosphorescent materials, photographic plates (leading Paul Villard to discover gamma rays in 1900 [6]) and electrometers. Electrometers are detectors adapted from the gold-leaf electroscope, invented by Abraham Bennet in 1787 [7]. These devices measured electric charge via the level of repulsion between two equally charged gold leaves. Becquerel discovered a loss of charge in an electrometer in the presence of radiation due to the ionisation of the gas within; the primary principle behind ionisation detector today.

The discovery allowed Pierre and Marie Curie to quantify radioactivity through the use of a Quartz Piezo Electrometer. The device, created by Pierre in 1898, combined the piezoelectric effect (discovered by Pierre and his brother, Jacques, in 1880) with the knowledge that radiation ionises air. By calculating the time taken to balance the pico-Coulombs of piezoelectricity produced from a quartz crystal by the charge produced in an ionisation chamber by a radioactive material, the radioactivity could be measured [5]. The Curies discovered the radioactivity and mass of uranium were directly proportional to one another. Becquerel and the Curies shared the Nobel Prize in 1903.

Julius Elster and Hans Geitel and, separately, Charles T. Wilson had developed the electrometer to increase the sensitivity of the device and, in 1901, discovered an electrometer still lost charge without exposure to radioactive material. Wilson suggested another type of highly penetrating radiation from outside the atmosphere may be responsible for the phenomenon, leading to the discovery of cosmic rays, or Höhenstrahlung, by Victor Hess in 1911 through the use of an electrometer [8].

In 1903, Sir William Crookes accidentally discovered zinc sulphide (ZnS) as a scintillator while investigating the radioactivity of radium bromide. The discovery led Crookes to invent the Spinharscope and ZnS is still widely used as a scintillator today [9].

Prior to 1908, quantifying radioactivity was carried out by equating charge to

activity. In an attempt to detect singular α particles from Radon, Hans Geiger invented the first proportional chamber. The detecting vessel of the apparatus consisted of a sealed brass cylinder (cathode) and a positively-charged, central thin insulated wire (anode), and exploited the knowledge that radiation ionised gases with a Townsend Avalanche, explained later in Subsection 2.1.1. Alpha particles ionised the gas and the applied electric field caused further ionisation to produce a detectable signal in the anode wire, registering single events [10]. Geiger modified this design in 1913, replacing the wire with a needle to produce the Tip Counter and the original device was further developed in 1928 by Geiger and Walther Müller in order to detect β particles and other ionising radiation, producing the Geiger-Müller tube (GM tube); becoming one of the most sensitive detectors for cosmic ray experiments and is still widely used in many radiation monitoring applications [11].

In the late 1800s, Wilson studied cloud formation and discovered a supersaturated state of water vapour would condense into a cloud around a nucleation point. Wilson used the knowledge that an ionised molecule would act as such a nucleation point and over many years developed the Cloud Chamber, finishing the device in 1911. The device was the first to show visible tracks of ionising radiation, long enough to be photographed and studied. In 1912, Wilson produced photographs for α particles, β particles and x-rays [12]. The cloud chamber proved to be one of the most valuable pieces of instrumentation in particle physics, winning Wilson the Nobel Prize in 1927 and leading to many particle physics discoveries. The cloud chamber was used by Arthur H. Compton in 1923 [13] to show the Compton recoil of an electron from an x-ray, aiding in the quantum theory of light. In 1932, Carl D. Anderson used a cloud chamber in a magnetic field and discovered the positron [14], giving rise to elementary particle physics and winning Anderson the Nobel Prize in 1936. Anderson and Seth Neddemeyer discovered the muon in 1936 using a cloud chamber during a cosmic ray shower [15], and in 1947 Cliff Butler and George Rochester discovered the kaon, also using a cloud chamber [16].

A significant leap in instrumentation was due to the work of Walther Bothe in 1924. Bothe created the coincidence method and applied it to GM tubes in 1929 with Werner Kolhörster to create the first cosmic ray telescope. The coincidence method inspired Bruno Rossi to build the first electronic coincidence circuit; the first practical AND circuit. Bothe won the Nobel Prize in Physics for the coincidence method in 1954 [17].

In 1933, Patrick Blackett and Giuseppe Occhialini combined GM tubes and the cloud chamber with a coincidence circuit, creating the first self-triggering coincidence detector for cosmic rays, allowing the confirmation of the discovery of the positron and discovering the process of pair-production and annihilation of electrons and positrons [18].

The above has described the general historical overview of the development of particle physics instrumentation, however, the following subsections will focus on the detectors pertaining to this thesis, i.e. gaseous detectors and plastic scintillator, and thus some important advances will be omitted, such as neutron detectors, Cherenkov detectors, liquid scintillator and solid state detectors. However, a moment is given to acknowledge Marietta Blau who pioneered the photographic emulsion technique from 1932 [19] and Donald Glaser who transformed the cloud chamber to the bubble chamber in 1952 [20]. Both detection techniques are now outdated but, at the time, revolutionised particle physics and led to many discoveries in the field.

1.1.2 Gaseous Detectors

The basic concept of the GM tube, i.e. having a gas-filled volume with electrode structures, was adapted into new electrode geometries, and often operated in different gain regimes, to develop a new category of detector; Gaseous Detectors (GDs). The first parallel-plate ionisation chamber (PPIC) was created by Bruno Zipprich in 1933 [21] and was developed by many physicists between the 1940s and 1960s into the spark chamber. Some of the most notable advances are attributed to Jack W Keuffel in 1949, who noticed a spark was produced between the parallel plates when an ionising particle passed through [22]; and Paul-Gerhard Henning who stacked multiple spark counters together and photographed coincidences in 1954 [23]. The spark chamber led to the discovery of the muon-neutrino by Leon Lederman, Melvin Schwartz and Jack Steinberger in 1962 [24] and the detector design has undergone many developments since, resulting in the Resistive Plate Chambers (RPCs) used today.

Parallel-plate cathode geometry detectors, combined with multiple anode wire readout, were also developed. The first Multi-Wire Proportional Counter (MWPC) was developed by Herbert Friedman in 1949 [25] and further developed by George Charpak in 1968 to include individual readout signal circuits [26]. This won Charpak the Nobel Prize in physics in 1992. The spatial resolution of the MWPC was limited

by the wire spacing and so risked large readout costs. The solution was to, somewhat, move backwards and readopt a signal wire readout but in a parallel plate geometry, measuring position from electron drift times. The drift chamber was created by Albert H. Walenta, Joachim Heintze, B. Schürlein in 1971 [27]. The multi-wire detectors continued to be used and the concept was developed by David Nygren in 1974 to produce the Time-Projection Chamber (TPC) [28].

Many detector designs have since branched off from the ionisation chamber design through creating new electrode geometries and associated instrumentation to produce detectors with greater positional resolution and higher rate capability. One of the main derivative detectors being the Time Projection Chamber (TPC). However, a lot is owed to those derived from the Micro-Strip Gas Chambers (MSGC) created by Anton Oed in 1988 [29]. The detectors were revolutionary to the field but were susceptible to radiation and spark damage. MSGCs were developed into alternative Micro-Anode structures to create a collections of detectors called Micro-Pattern Gas Detectors (MPGDs). Such detectors were the Micro-Gap, Micro-Dot and Micro-Wire Chambers. The development of these detectors also saw a need to increase the gain within the detectors, leading to the invention of the Gas Electron Multipliers (GEMs) by Fabio Sauli 1996 [30].

1.1.3 Scintillators

Aside from the two scintillators mentioned above, the bluish glow from a material due to radiation had been known well before Cherenkov investigated the phenomenon in the 1930's; even being noted by the Curies. However, using the light produced within a medium to detect particles did not progress much until the invention of the Photo-Multiplier Tube (PMT). The device exploits the photoelectric effect and secondary electron emission to convert photons into a measurable quantity of electrons, paving the way for scintillators to become the dominant counting detectors. There is much controversy surrounding who invented the PMT, with much of the credit going to Vladimir Zworykin, George Morton and Louis Malter for creating the first multi-stage PMT in 1936 [31], and Harley Iams and Bernard Salzberg creating the first single-stage PMT in 1930 [32]. However, Leonid Kubetsky supposedly created a multi-stage PMT in 1933 [33], but the device was not deemed practically useful and, with Kubetsky being a Soviet-era physicist, the invention went largely undocumented in the West.

Two categories of solid scintillators exist; organic and inorganic. Inorganic scintillators are high-density crystals that are intrinsic scintillators, whereby the luminescence comes from the lattice structure, but may require the addition of fluorescent ions such as Thallium or Cerium. As this thesis does not investigate inorganic scintillators, and noting each discovery made in inorganic scintillator detectors throughout the past century would be an arduous undertaking, the discoveries are briefly depicted in Figure 1.1.

Organic scintillators comprise of aromatic hydrocarbon (mainly containing benzenoid rings). The fluorescence within these materials arise from energy level transitions of these individual molecules, rather than from the structure of the bulk material, and thus organic scintillators scintillate in any physical state (e.g. in solution, liquid, polycrystalline material, etc.). A deeper discussion into the theory of scintillation within organic scintillators will be made in Section 2.2.

The first organic scintillator was a Naphthalene crystal, discovered by Hartmut Kallmann in 1947 [35]. Kallmann noticed Naphthalene was transparent to the scintillation light it produced and, after attaching the crystal to a PMT, observed the scintillation pulses were extremely short compared to a GM tube. In the few years

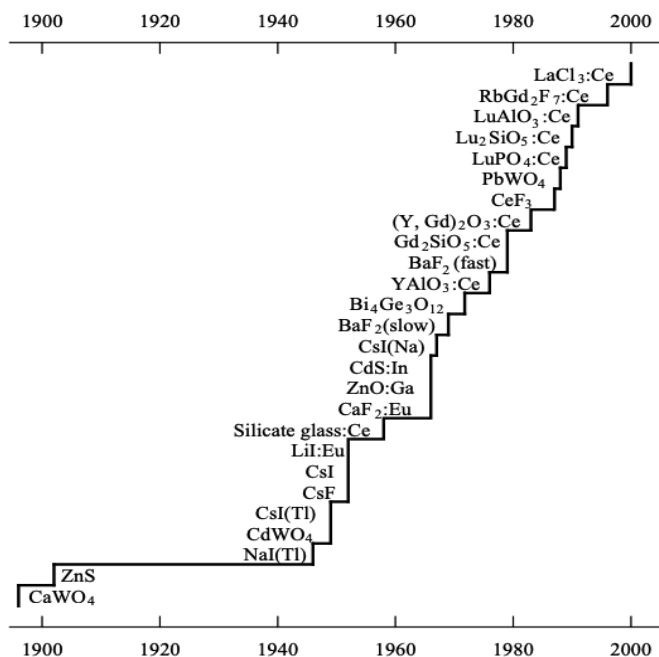


Figure 1.1: Brief history of the discovery of inorganic scintillators. Figure from [34].

following, many, more efficient, organic scintillators were discovered through experimentation with various aromatic hydrocarbons: an anthracene crystal was first used by P. R. Bell in 1948 [36], followed by a stilbene crystal by W. S. Koski and C. O. Thomas in 1949 [37].

Anthracene held many advantages, being transparent to the large scintillation pulses it produced, however, growing anthracene in large crystals posed difficulties, unlike with Naphthalene. In 1950, J. B. Birks created the first crystal solution organic scintillator by growing a naphthalene crystal with 9% anthracene to create an organic scintillator with the advantages of both [38]. Many more organic crystal scintillators followed, as did the creation of organic scintillators in liquid solutions, and by 1955 over 55 pure organic compounds had been identified [39].

In this time, the most significant discovery, within the scope of this thesis, was by Marvin G. Schorr and Franklin L. Torney in 1950. Schorr and Torney combined terphenyl, and *trans*-stilbene, in various percentages with polystyrene (PS) to create the first "Solid Non-Crystalline Scintillation Phosphors", or plastic scintillators [40].

Without the need to produce pure scintillator crystals, organic or inorganic, plastic and organic liquid scintillators dominated the scintillator counter field. By matching absorption and emission spectra, efficient scintillation mixtures were created and the compositions were tuned through experimentation to increase detection efficiency and light yield.

Today, plastic scintillators still follow the same basic formula, using one or more scintillators, or fluors, in a polymer matrix, such as PS or Poly(methyl methacrylate) (PMMA). While organic liquid or crystal scintillators hold many advantages over plastic scintillator, such as light yield and, consequently, energy resolution, the main advantages of plastic scintillators are chemical stability; having a high degree of optical homogeneity; cheap production methods; and, the most important with respect to this thesis, the plastic can be easily machined or moulded into various shapes.

1.2 Motivation for Low-Cost Solutions to HEPP Instrumentation

Many of the milestones of discovery described in Section 1.1 initiated new areas of physics to investigate, new theories to postulate and new experiments to conduct. In each case, the progression of particle physics has emanated from either the invention, development or adaptation of instrumentation to satisfy the experimental needs of the time; often utilising advances in other fields and, in an increasing number of cases, opening the doors to commercialisation.

In the current scientific climate, particle physics, like many fields, is subject to constraints in funding and project timescales, but specialised equipment is expensive to purchase from industry, or time consuming to build from scratch. The demand for particle detectors, outside of research, is growing rapidly in the world, with the overlap between academia and industry constantly increasing. The desire for low-cost detectors is present and modern solutions are required.

1.2.1 3D Printing Detectors

Many industries have a need for constant radiation monitoring, such as homeland security organisations, law enforcement authorities, the nuclear industry and bio-medicine fields. To achieve this level of surveillance, a large number of radiation detectors are required, leaving the end user with excessive expenditure, especially when developing novel solutions to new or existing problems. A method of producing large numbers of reliable detectors in a cost-effective and timely manner is required, and by exploiting the recent developments made in Additive Manufacturing (AM), this technology is explored as a viable solution within this thesis.

AM is a technique used to fabricate 3D models from CAD files by the addition of successive layers of material; a process that opens up the ability to fabricate unusual geometries which are beyond the limits of conventional machining and yield interesting properties, such as the gyroid structure [41]. AM was developed in the 1980's as a method of producing basic prototypes of models, however, the available processes were expensive and slow.

Recent years have seen new technologies and developments occur in many fields, such as engineering and control systems, which have extended the scope of AM greatly. Improved speed and accuracy of AM processes have enabled fast production

of high quality, fully-functioning end products, and an increase in the range of materials that can be used in AM processes has allowed more complex designs and geometries to be fabricated. The commercialisation of AM products has also allowed Rapid Prototyping (RP) to become a cost-effective and accessible technique widely used in Research and Development projects. RP is an iterative process of designing a model, fabricating the product, testing the product against functional requirements, and altering the model to further meet those functional requirements. The process ends when the product meets or surpasses the requirements. AM is now a convenient production method already being utilised in many fields, such as the 3D printing of replacement bones in the medical industry [42] and printing strong, lightweight aerospace structures [43].

Motivation for Additive Manufacturing in HEPP Instrumentation

In 2013, M. Hohlmann issued a white paper posing a “Grand Challenge” to those in the HEPP instrumentation field:

‘The aggressive development of additive manufacturing, also known as 3D-printing, for the production of particle detectors in collaboration with industry.’ [44]

In the paper, Hohlmann outlines the AM capabilities required to 3D print complete GDs, such as MPGDs (containing GEMs), for HEPP experiments requiring high spatial resolution; and includes Table 1.1 that compares these to the actual AM capabilities of the technology at the time. The comparison shows that, despite the advancements made, there were still large discrepancies between the two sets of values, and these discrepancies still held in 2015 when the work in this thesis began. It should be noted that now, in 2019, AM technologies could potentially be capable of printing MPGDs, however, the machines needed to fabricate such detectors are very advanced and are still too expensive to be a valid cost-effective solution. Regardless, the disparities outlined by Hohlmann were only in reference to the complete fabrication of a fully-functional GDs of intricate design, but AM technology could still be utilised within the HEPP instrumentation field to produce GDs of simpler designs, such as Single-Wire Gaseous Detectors (SWGDS), and the R&D of new GD geometries. The paper also only applies to the 3D printing of GDs, and with the range of printable materials ever increasing, AM technology could be utilised in the

	Capability (2013)	Performance goal
Printing resolution in x-y	$\sim 75 \mu\text{m}$	$\sim 1 \mu\text{m}$
Layer thickness in z	$\sim 50 \mu\text{m}$	$\sim 1 \mu\text{m}$
Print speed	10 cm/s	$> 100 \text{ cm/s}$
Materials	Either polymers or metals	Polymer-metal composites
Object size	$(50 \times 50 \times 50) \text{ cm}^3$	$(200 \times 100 \times 10) \text{ cm}^3$

Table 1.1: A table comparing commercial AM capabilities to the performance needed to 3D print complete Gaseous Detectors such as MPGD (containing GEMs), for high spatial resolution detectors required in HEPP experiments. Adapted from [44].

R&D of other detector types, such as the production of new scintillator shapes and arrangements for novel applications.

The possibilities that AM presents to HEPP instrumentation are vast. Concerning only GDs, AM would allow for the production of cheap modular detector arrays that can have broken modules easily printed and replaced, allowing for less experimental downtime. Fast production times could be utilised to fabricate prototype detectors to test front-end and readout electronics, allowing both detectors and electronics to be created in parallel more easily. Concerning both GDs and plastic scintillator, AM offers ease of design alteration within CAD software to allow simple modification, customisability and scalability; meaning basic detector designs could become unique and application specific; and the ability to fabricate uncommon shapes, allowing for the investigation into new detector geometries. The increasing availability and access to AM technology could also open up detector production for many outreach applications, further engaging schools and the public in HEPP.

Fused Deposition Modelling

Many different AM techniques exist, such as Aerosol Jet Printing, Metal Powder Sintering and Stereolithography, however, the technique most available at the University of Sheffield, and for the work carried out in this thesis, is Fused Deposition Modelling (FDM). Most AM techniques follow the same initial processes, i.e. a 3D model is designed using CAD software (to produce an stl file), the design is processed through specific software to produce slices of the 3D model and finally the slices are passed to the 3D printer to create the model. In FDM, the 3D printing process consists of extruding molten thermoplastic onto a baseplate to produce a

single x-y layer. The baseplate is then lowered in the z-direction and a subsequent layer is printed on top of the previous, thermally fusing the two layers together upon contact. The process is repeated for each successive layer until the model is complete. Figure 1.2 illustrates this process.

The quality of a 3D printer, and the associated AM technique, can be measured by many criteria, however, the most important are:

- Build Size
- Resolution
- Range of Print Materials
- Price
- Reliability
- Software/Community
- Build Speed
- Ease of Use
- Upgradability

FDM may be one of the crudest AM techniques available, lacking in build speed and the highest resolution, but FDM still offers many desirable advantages. FDM printers are some of the easiest printers to use and the cheapest printers to buy, especially when relating build size to price due to the simplicity of the design. This has resulted in FDM being the most commonly used technique and has the largest user community for support and open-source software. The simple design also means FDM printers have the greatest upgradability, often with the new parts able to be printed on the same machine.

The current range of print materials available to FDM is poor in comparison to other AM techniques. Aerosol Jet Printing, for example, can print almost any nano-particle suspension in a suitable solvent, such as metals, semi-conductors, insulators, ferrites or polymers [45], however, different post processing techniques are required. FDM prints only thermoplastics filaments, such as Acrylonitrile Butadiene Styrene (ABS), Polylactic Acid/Poly lactide Resin (PLA), High Impact Polystyrene (HIPS) and PMMA, but composite materials are constantly under development. Electrically conductive, ferro-magnetic, dissolvable and super-flexible filaments are already widely available and the need for post processing is rare. Many thermoplastics are also relatively moisture, heat and chemical resistant, and have minimal shrinkage or warpage upon cooling, making them ideal detector build materials. The thermoplastics men-

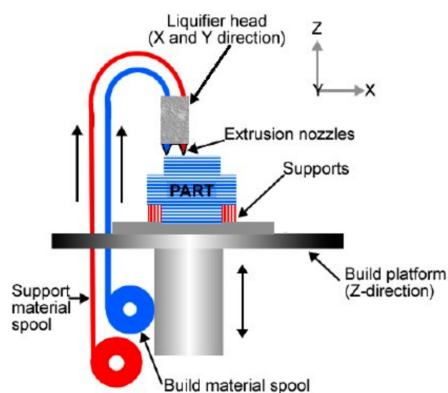


Figure 1.2: Schematic of the FDM process. Figure from [46].

tioned above offer the possibility to print airtight GD enclosures and the electrically conductive filament can be used for electrode structures. As previously discussed, plastic scintillator requires a polymer matrix such as PMMA or PS, which are already available thermoplastic materials, and FDM has already been used to produce transparent models in ABS [47].

3D Printers

Two different FDM printers were available to this thesis project: The Makerbot Replicator 2X - Experimental Printer, and the Gigabot GB3 from re:3D. Initially, the Makerbot was the only printer available and so initial work was performed using this printer. The Makerbot is capable of dual extrusion, can achieve a layer height and width resolution of 100 and 400 microns, respectively, and can print most thermoplastics due to the available heated print bed. The Makerbot does come with many disadvantages as it is has relatively small print volume of dimensions 246 mm x 152 mm x 155 mm ($x \times y \times z$), and can only print 1.75 mm diameter filaments, resulting in low print speeds. The Makerbot can only process model stl files with



Figure 1.3: Picture of the re:3D Gigabot GB3 at The University of Sheffield.

Makerbot slicing software, Makerware, which produces binary .x3g print files that cannot be edited, and the Makerbot has been made almost impossible to upgrade, by purposeful design by the company.

The Gigabot is a large-scale commercial printer with a much larger print volume of dimensions 590 mm x 600 mm x 600 mm ($x \times y \times z$). Like the Makerbot, the Gigabot is a dual extrusion, FDM printer that can achieve the same height and width resolutions, however, the Gigabot can process 3 mm diameter filament, meaning much quicker print speeds. Two more important key features of the Gigabot are the cooling fans placed next to the extruders, which cool the thermoplastic immediately after extrusion (the importance of this is discussed later) and the Gigabot is compatible with most slicing software to produce gcode files. Gcode is a text based language that uses commands to instruct the printer; each line in a gcode file is a separate command and therefore by understanding the language, the file can be understood and edited. The designs used throughout this thesis are made in OpenSCAD [48]. OpenSCAD is a free, script-only based modeller, using a description language specific to the software which uses various functions and basic shapes to produce complex 3D models that can be easily edited.

1.3 Summary: Aims of this Thesis

Given the above overview of the Additive Manufacturing (AM) technology available at The University of Sheffield and the possible advantages that AM present to High Energy Particle Physics instrumentation, this thesis will discuss the work performed throughout this PhD to assess the viability of 3D printing as a means of producing particle detectors, mainly Gaseous Detectors (GDs); with the aim to reduce the human element of production, while minimising any chance of error during the fabrication process.

As mentioned, Single Wire Gaseous Detectors (SWGDs) are GDs of the simplest design and, thus, the production of such detectors will be the main focus throughout this thesis; the required components of these detectors will be discussed further in Chapter 2. By continually investigating and assessing the limitations of Fused Deposition Modelling, and the various available thermoplastics on the market, a method of successfully 3D printing these components, and assembling them, into a fully functioning detector will be developed.

Once the possibilities of the technology are understood, and a working detector is created, the aforementioned benefits of AM will be utilised to develop a novel detector design. Additionally to SWGDs, investigation into the use of FDM to produce other GD's will also be discussed.

The development of a FDM printable, scintillating plastic filament will also be discussed; initially designed to complement the 3D printing of GDs by allowing a scintillating trigger panel to also be printed. Such a filament would lead to far more possibilities, as FDM would be able to produce novel scintillator geometries, which would otherwise be impossible or difficult to produce.

Chapter 2

Theory of Detection

The following chapter will briefly discuss the principles of detection in both Gaseous Detectors (GDs) and plastic scintillator; from the point at which energy is deposited within the detection medium to the point of signal detection.

2.1 Gaseous Detectors

2.1.1 Principles of Operation

As outlined in Section 1.1, GDs have been, and still are, widely used in HEPP experiments to measure the position or trajectory of charged particles. A GD is comprised of 2 main parts: the drift gas, as the ionisation medium, within an airtight enclosure, and the electrodes to produce an electric field. Charged particles ionise the gas to produce ion pairs and, under sufficient electric field, these ion pairs drift towards corresponding electrodes, causing further ionisation, and induce a signal. Charge or timing measurements are used to reconstruct the position or trajectory of the incident charged particle, with some energy resolution possible.

Track Production

As a charged particle propagates through the gas-filled volume of the GD, Coulomb interaction occurs between the incident particle and bound atomic electrons, resulting in the transfer of energy. If enough energy is transferred from the incident particle to the electrons, ionisation of the gas medium can occur along the path of the particle.

The ionisation of the gas occurs randomly, however, the average distance between ionisations can be characterised by a mean free path, λ . This value is inversely proportional to the density of electrons in the gas, N_e , and the average ionisation cross-section of the gas, σ_I , which is dependent on the Lorentz factor, γ , of the incident particle. The mean number of primary ion pairs is therefore given by L/λ , where L is the distance travelled through the gaseous volume.

$$\lambda = 1/N_e\sigma_I \quad (2.1)$$

As each ionisation is independent of the previous, the frequency distribution is a Poisson distribution (Eqn 2.2). The fluctuation in the number of ionisations over L is given by the square root of the average number of ionisations, $\sqrt{L/\lambda}$.

$$P(L/\lambda, N) = \left(\frac{L/\lambda}{N!}\right)^N \exp(-L/\lambda) \quad (2.2)$$

Primary ionisation occurs via interactions with the incident particle, however, the majority of ion pairs are created through secondary ionisation. Secondary ionisation occurs when electrons from primary ionisation have enough kinetic energy to further ionise the gas or, in gas mixtures, via the Penning Effect [49]. This effect can occur if one component of the gas can be excited to a long-lived, metastable excitation state, and another component has an ionisation energy lower than that of the excitation energy, $E_{Ex}^A > E_I^B$. Collisions between the two components can then liberate an electron.

The energy lost by the incident particle as it propagates through the drift gas is not all spent on ionisation, as energy is lost through other mechanisms, such as Bremsstrahlung. This results in the average energy loss per ion pair (W) being greater than the average ionisation energy of the drift gas. W depends on the gas used and the incident particle, however, it is independent of the initial energy of the incident particle above a certain threshold (electrons: $E_i \sim$ few keV; alpha particles: $E_i \sim$ few MeV), whereby the ionisation cross-section decreases rapidly and other energy loss mechanisms become dominant.

Drift gases are mainly comprised of noble gases, for which W has a typical range of 22 - 46 eV, however, adding a small concentration of polyatomic gas, known as a quench gas, can decrease W as these have lower ionisation energies. This also results in the quench gas tending to be the dominant source of positive ions, as

charge transfer occurs between positive ions and neutral gas molecules with a lower ionisation energy.

δ -electrons can also be produced in the secondary ionisation mechanisms, whereby the secondary electrons produced have enough kinetic energy to travel a significant distance from the initial ionisation region; producing secondary tracks which are distinctly separate from the primary track.

If a significant electric field is not present in the gas volume, recombination of electrons and positive ions can occur causing UV photon emission. The UV photons can cause further ionisation of the gas or liberate a photoelectron from the surrounding electrodes, resulting in an ionised region separate to the initial track. An organic quench gas tends to be used as these have strong UV absorption to significantly reduce this effect.

Electron attachment can also occur within the gas, whereby a neutral molecule captures a free electron to produce a negative ion. These negative ions are detrimental to a fast signal production due to the low mobility of ions. Noble gases and hydrocarbons are typically used in GDs as they have low electron attachment coefficients, unlike halides, water and oxygen which must be removed from the detector to efficient operation.

Charge Drift

To detect the incident particle, the ion pairs must travel to/from the electrodes to induce a signal. A potential difference is applied between electrodes to produce an electric field, or drift field, E_d ; the arrangement of the electrodes is specific to the type of detector and will be discussed further in Subsection 2.1.2. As the electrons accelerate towards the closest anode, they collide with molecules in the drift gas and scatter isotropically, randomising the direction of velocity. The scattered electrons then accelerate towards the anode again. The repeated process of acceleration and scattering allows the electrons to be modelled as having a constant drift velocity, v_d , allowing timing measurements to be performed in drift chambers. The drift velocity of a charged particle (electron or ion) is dependant on many factors, such as the applied drift field; drift gas composition, density and temperature; and the particle mass and charge. Despite the many determinants, the drift velocity can be characterised by the mobility of the particle within the drift gas, μ , given the applied drift field, whereby $v_d = \mu E_d$.

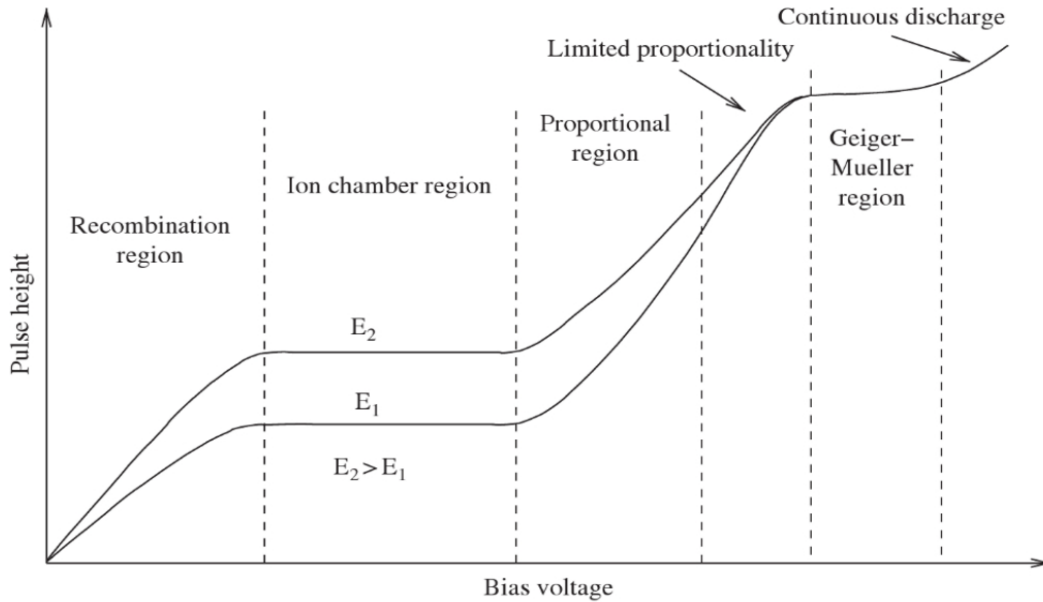


Figure 2.1: Typical signal heights with respect to bias voltage applied between anode and cathode [50].

To minimise the loss of kinetic energy during collisions, a drift field is used such that the energy gained by an electron between collisions isn't sufficient to excite or further ionise the drift gas. A quench gas can significantly increase the achievable drift velocity as collisional energy is absorbed into rotational modes. As ions are heavier, ion mobility is significantly less than electron mobility ($\mu_e \sim 1000 \mu_{ion}$), thus ions experience lower acceleration and do not scatter isotropically.

Charge and Signal Production

Figure 2.1 shows the operational regions of GDs, which are dependant on the potential difference, or bias voltage, applied to the electrodes. In the recombination region, the bias voltage is low enough such that recombination can still occur, ranging from zero to the bias voltage at which negligible recombination occurs. The magnitude of secondary ionisation also increase throughout this range. The resulting signal from operating in this region has some dependency on the energy deposited within the GD, however, detectors do not tend to operate within this region, especially as recombination can produce UV photons, which can degrade the detector.

Operating in the ion chamber region, the efficiency of charge collection on the

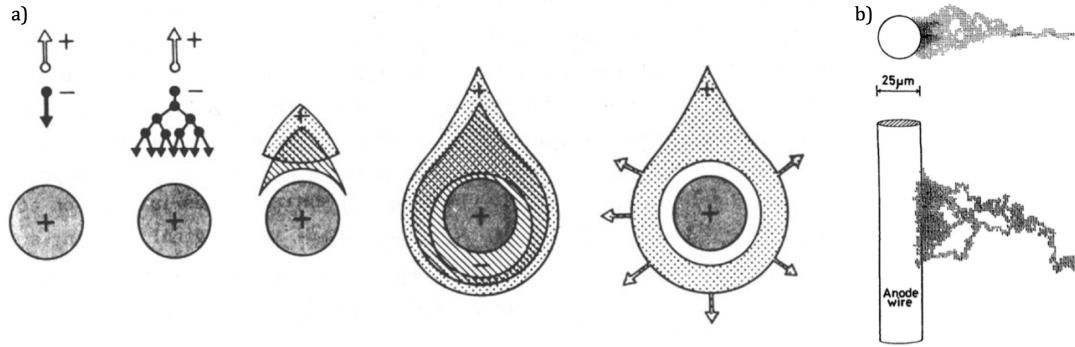


Figure 2.2: (a) Ionisation process around an anode wire [51]. (b) A Monte-Carlo simulation of the electron avalanche that occurs close to an anode wire [52].

electrodes is maximised and remains constant with bias voltage, although some recombination can still occur. The induced signal is proportional to the initial energy deposited by the incident particle. This region operates at a bias voltage between the upper limit of the recombination region and the bias voltage, at which the electrons gain sufficient energy to cause exponential secondary ionisation close to the anode. Detectors that operate in this region are called ionisation chambers.

In the proportional region, the bias voltage is sufficient enough to accelerate electrons to energies greater than the ionisation energy of the drift gas, causing further ionisation to occur close to the anode ($\sim 50 - 100 \mu\text{m}$). These ionisation electrons are then also accelerated to these ionising energies in the large electric field, causing further ionisations to occur; this process is known as Townsend Avalanche [50]. Figure 2.2 (b) shows a Monte-Carlo simulation of the process. The avalanche allows for a larger signal to be induced, whereby the charge multiplication is proportional to the initial energy deposited by the incident particle, and the magnitude of the electric field. Detectors that operate in this region are called proportional counters and require a quench gas to limit avalanche runaway.

In the limited proportionality region, the same process occurs as in the proportional region but to a higher degree. As the positive ions produced in the avalanche have a lower mobility than the electrons, the positive ions form a positive cloud around the anode, shielding the electric field and limiting the avalanche, shown in Figure 2.2 (a). The signals produced from operating in this region are no longer proportional to the energy deposited by the incident particle and thus detectors are not operated in this region.

In the Geiger-Müller region, the bias voltage used is large enough such that each incident particle results in a severe avalanche occurring. Shielding produced by the accumulation of positive ions is significant and recombination occurs producing UV photons, which cause ionisation throughout the detector. The signal produced is independent of the deposited energy and much greater than the noise level [53], thus every incident particle is detected. The large number of ion pairs produced results in this operational mode having a large dead-time, as the accumulation of positive ions significantly reduces the effective electric field. The dead-time ends once the positive ions have been neutralised by the cathodes.

In the continuous discharge region, the bias voltage applied is great enough to cause breakdown of the drift gas. Primary ionisation causes secondary ionisation throughout the gas and the detector discharges producing electric arcs between electrodes, such as in spark chambers. Operating in this region can cause permanent damage to the detector, as shown in Figure 2.3.

The signals created are not produced by the collection of charges at the electrodes, but are induced via the movement of the charges towards and away from the electrodes. In proportional counters, the electrons created in the avalanche reach the anode in < 1 ns and result in a small, sharp signal which accounts for 1 – 2% of the overall induced signal. The remaining 98 – 99% of the signal is induced by ion movement, as positive ions have a much lower mobility, the time taken for these ions to reach the cathode is of the order of 1 ms and results in the induced signal having a large ion tail which dominates the induced signal.

The amplification, or gain, due to avalanche is dependant on many factors, such as drift gas composition, electrode shape (e.g. anode wire radius) and, mainly, the applied electric field. As mentioned, operating in the Geiger-Müller region results in significant amplification and produces signals much greater than the noise level, and so can be easily measured. Operating at lower bias voltages produces significantly smaller signals, with operation in ion chamber region producing signal close to the noise level [53], and even smaller signals from the recombination region.

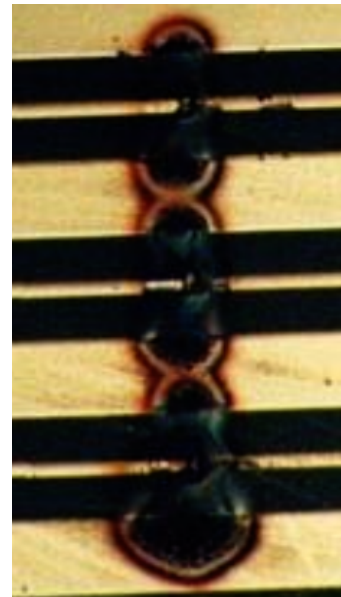


Figure 2.3: A photograph of a MicroStrip Gas Counter (MSGC) damaged by discharges. Adapted from [54].

Consequently, to measure signals from operation in these regions require further amplification. Preamplifiers (preamps) and amplifiers are both typically used for this. Preamp are, ideally, connected as close to the detector as possible, to minimise noise pickup and, to a lesser degree, minimise signal attenuation. Amplifiers often output signals of a characteristic shape making further analysis easier, however, this is typically a bi-product of noise reduction within the amplifier.

2.1.2 Types of Gaseous Detectors

Single Wire Gaseous Detectors

Single Wire Gaseous Detectors (SWGDs) are the simplest of GDs; consisting of drift gas, a single anode wire and an airtight enclosure - usually comprised of a surrounding cathode structure. The applied electric field is typically of the order of a few 100 V/cm, but the actual value is dependent on the electrode configuration and drift gas.

The most commonly used geometries of SWGDs are planar and cylindrical. Planar SWGDs (shown in Figure 2.4) are typically used as drift chambers. The drift chambers consist of 2 parallel cathode plates separated by \sim few cm, to allow for sufficient propagation length through the drift gas, and a high tension anode wire, $r_a \sim 10 \mu\text{m}$, running equidistant between the cathode plates. The two parallel plates create a uniform electric field along the detector for constant drift velocity,

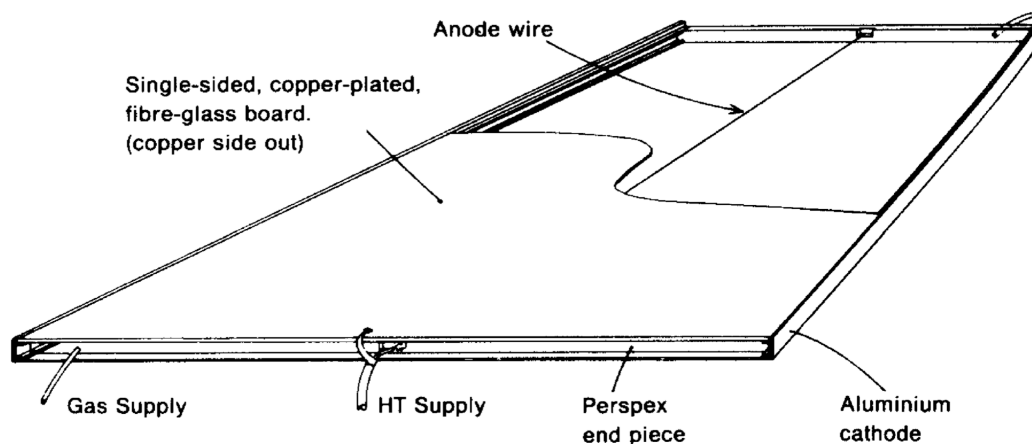


Figure 2.4: Schematic of single wire drift chamber, showing the major components [52].

only altering around the anode wire for avalanche to occur. Drift chambers are used in conjunction with trigger panels to determine the position of a particle; the drift time (the time difference between the detector trigger signal and the first electrons to arrive at the anode) multiplied by the characteristic drift velocity gives the position of the particle path orthogonal to the wire. These planar designs tend to be large area, with many stacked above another, often in orthogonal layers, to allow tracking to be performed. The positional information from the stacked detectors is used to reconstruct the trajectory of the particle.

Cylindrical SWGDs, or *Ionisation Tubes*, operate in the similar way as the planar geometry but, instead of the 2 parallel cathode planes, a single cylindrical cathode tube is used with a central anode, creating a radial electric field. Ionisation tubes can either be used individually, such as GM Tubes, or arranged in a hexagonal packing configuration (Figure 2.5), such as Drift Straws, with coincident signals from multiple tubes used to reconstruct the particle trajectory. The isochrone produced, characterised by the drift time and drift velocity, is a cylinder centred around the anode wire. By fitting a line to fit multiple isochrones, the particle trajectory can be reconstructed.

The resolution of the reconstructed trajectory increases as more layers of SWPCs are added/hit, as the error on the incident angle is reduced. While timing measure-

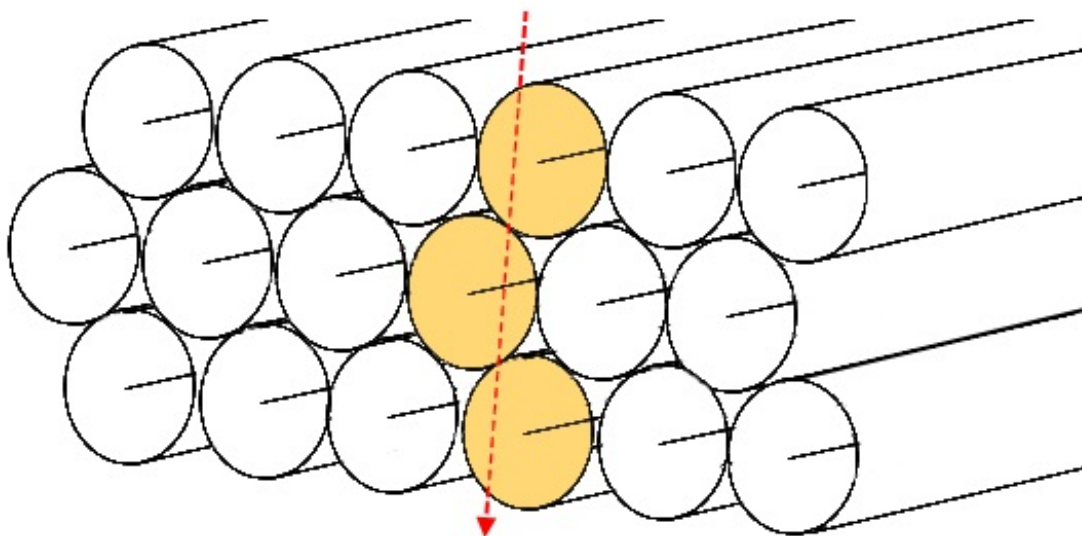


Figure 2.5: Schematic of cylindrical SWPCs in a hexagonal packing configuration to allow for charged particle tracking.

ments are used predominantly, the total charge induced in each tube can be related to the path length of the incident particle through the tube and could give more information on the particle trajectory through the detector; although the number of primary ion-pairs produced in the gas is subject to large fluctuations resulting in large errors. The tube diameter can range from a few mm to a few cm and up to a few metres in length [55][56].

Limited Streamer Tubes (LSTs), *or Iarocci Tubes*, are a somewhat simplified version of an Ionisation Tube, whereby the cathode tube is replaced by plastic tubing (mainly PVC) with a thin, uniform layer of resistive graphite coated on the inside; the anode wire usually has a larger radius $\sim 100 \mu\text{m}$ [57]. The signal usually detected by the cathode tube is instead read out by x-y strips or by a pixel array detector (PAD) readouts located outside the tubes.

The LSTs can operate in proportional mode, however they are usually operated in self-quenching streamer (SQS) mode, located between the limited proportionality and Geiger-Müller regions seen in Figure 2.1. SQS mode is achieved by using a bias voltage located in the Geiger-Müller region, however, the runaway ionisation usually produced in Geiger-Müller mode is extinguished within $\sim 1 \text{ cm}$ by using a higher ratio of quench gas. The localised runaway ionisation causes a thin plasma filament, called a streamer, to develop from the anode wire towards the resistive cathode. The streamer causes a large dead-time, but only for the length of anode wire close to the streamer allowing the rest of the detector to operate normally. The more quench gas used, the shorter the streamers and the lower the dead-time. LSTs can have a wide voltage plateau ($\sim 700 \text{ V}$); large, noiseless signals are produced; and are cheap and easy to mass produce for large detectors.

MulWire Proportional Counters (MWPCs)

MWPCs are similar in construction to SWGDs but consist of multiple wires, usually separated by $2 - 5 \text{ mm}$. MWPCs tend to be in planar geometries, with the wires equidistant between segmented cathode planes (Figure 2.6), or use cathode wires to shape the electric field around the anode wires. MWPCs, like ionisation tubes, do not rely on timing measurements to determine the position of the incident particle, but instead use the ratio of signal amplitudes induced on the anodes and cathodes. Like SWGDs, many MWPCs are stacked to allow tracking to be performed, however a trigger panel is not required.

MicroPattern Gas Detector

MicroPattern Gas Detectors (MPGDs), operate similarly to the MWPCs but wires are rarely used, unless to further shape the electric field. A MPGD is typically comprised of an upper cathode plane and a segmented lower plane, consisting of various possible electrode configurations.

Many different variations of the MPGD exists, Figure 2.7 depicts 2 different types; a Pixel Array Detector, or PAD, and a Micro-Strip Gas Detector, or MSGD. In the PAD each electrode can be read out individually or via resistive charge division. The anode pixels are usually $\sim 10 \mu\text{m}$ wide to allow for accurate spatial measurements. Again, many of these detectors are stacked to allow for tracking.

The MSGD consists of alternating anode and cathode strips, which are of the order of $100 \mu\text{m}$ and $10 \mu\text{m}$ in width, respectively. Having alternating anode/cathode strips results in an increased electric field near to the anode (Figure 2.8), allowing avalanche formation and, consequently, a larger induced signals. Another read out plane can be placed under the alternating anode-cathode plane, separated by a dielectric material (e.g. ceramic). This plane consists of only anode strips, which run orthogonal to the alternating anode-cathode strips to provide spatial measurements in the x-y plane. The strips can be read out individually, but are usually read out by resistive charge division.

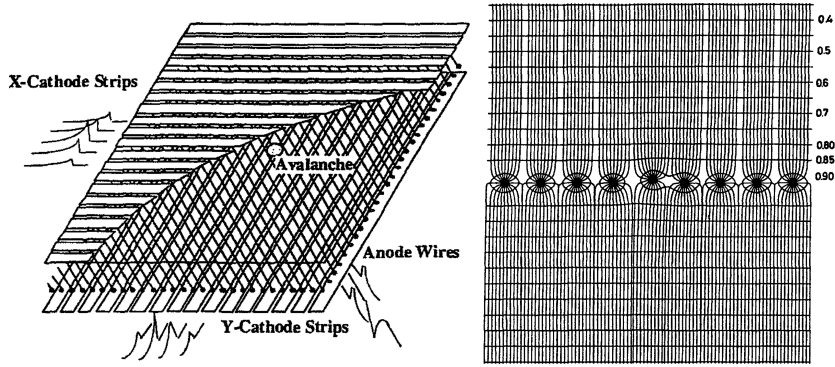


Figure 2.6: (Left) Diagram of MWPC, showing segmented cathodes for increased spatial resolution [58]. (Right) Schematic of the electric field present in MWPC. Adapted from [59].

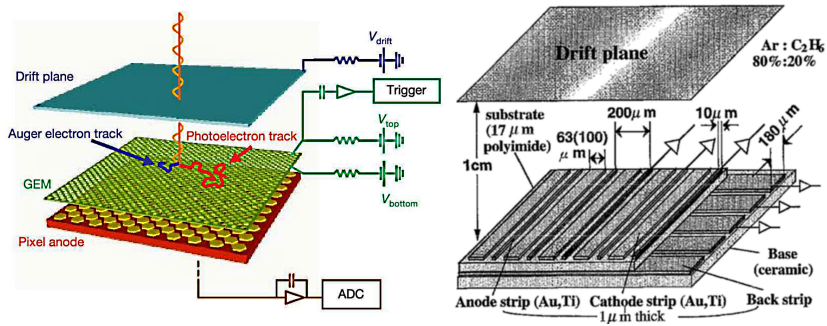


Figure 2.7: (Left) Diagram of a Micro-Pattern Gas Detector, including a Gas Electron Multiplier (GEM) [60]. (Right) Schematic of Micro-Strip Gas Detector with alternative cathode-electrode strips and a lower segmented cathode layer running orthogonal. Figure from [61].

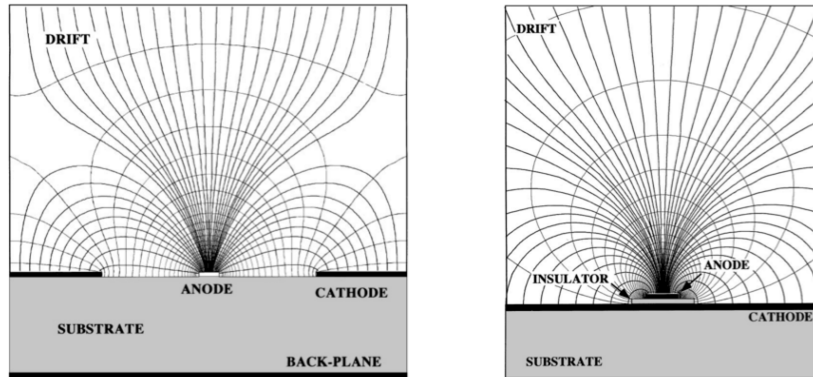


Figure 2.8: Computed field lines and equipotentials due to near anode-cathode geometries in MPGDs; (Left) MSGD, (Right) MicroGap Chamber. Figure from [62].

2.2 Plastic Scintillators

2.2.1 Principles of Operation

As described in Subsection 1.1.3, organic scintillators are benzene-containing hydrocarbons which supply the π -electron structure vital for the scintillation mechanism. Plastic scintillators are made by adding one or more organic scintillators, or fluors, to a convenient base, which is then polymerised. The majority of the plastic scintillator composition is the polymer base, with fluors taking up only 1 – 2% by weight.

Scintillation Mechanism

When charged particles are incident on an organic scintillator, the particle loses energy within the medium, mainly via Coulomb interactions with bound electrons. Gamma rays may also interact with the medium via 3 mechanisms: the photoelectric effect, Compton scattering off an orbital electron, or e^+e^- pair-production. Each of the mechanisms produce energetic particles (mainly electrons) within the medium which interact with the bound electrons via Coulomb interactions.

The above interactions excite the bound electrons from the S_0 ground state to any of the S_1 (or higher) states, i.e. the excited S_1 state (S_{10}) or any of the vibrational excited states (S_{11} , S_{12} ...), as shown in Figure 2.9. The instability in the system due to the S_1 vibrational states being occupied results in these electrons being forced into the S_{10} excited state via radiationless internal conversion in the order of 100 ps. From S_{10} , electrons will fall to the S_0 ground state via 2 mechanisms.

The first mechanism is to decay to the S_0 via photon emission. The decay time is a few ns and the emitted photon is usually in the UV spectrum. This fast emission is Fluorescence. In the second mechanism, the electrons transition to the T_1 triplet state via inter-system crossing - a non-radiative state change whereby the spin of the excited electron is reversed - and then decay to the S_0 state via photon emission. The T_1 state is stable and long-lived and decay can only occur due to indirect interaction with another molecule; the typical decay time is 100 ms. This delayed emission is Phosphorescence [63]. These two decay mechanisms are depicted in Figure 2.9 (*Left*). The time dependent light intensity is depicted in Figure 2.9 (*Right*) and described by Equation 2.3 [50], where τ_1 and τ_2 are the lifetimes of the S_1 and T_1 states, respectively.

$$I = I_0(e^{-t/\tau_1} + e^{-t/\tau_2}) \quad (2.3)$$

Wavelength Shifting

As described above, the energy absorbed by a fluor molecule is often greater than the energy emitted, as electrons move to excited vibrational states but do not radiatively decay from them. The difference in absorbed and emitted energy is described by Stoke's Law, which states the fluorescence wavelength is greater than absorption wavelength. While this is true for the corresponding peak wavelengths, the spectra are broad and thus overlap does occur. The difference between the peak wavelengths is known as the Stoke Shift. The larger the Stoke Shift, the more light will be emitted from the scintillator and less will be re-absorbed [50].

When a charged particle or gamma ray is incident on plastic scintillator, the majority of the energy deposited is within the polymer base, leaving the polymer in an excited state. Some polymer bases, such as PS will scintillate, however this fluorescence is in the UV (typically 300-350 nm) and has an attenuation length of a

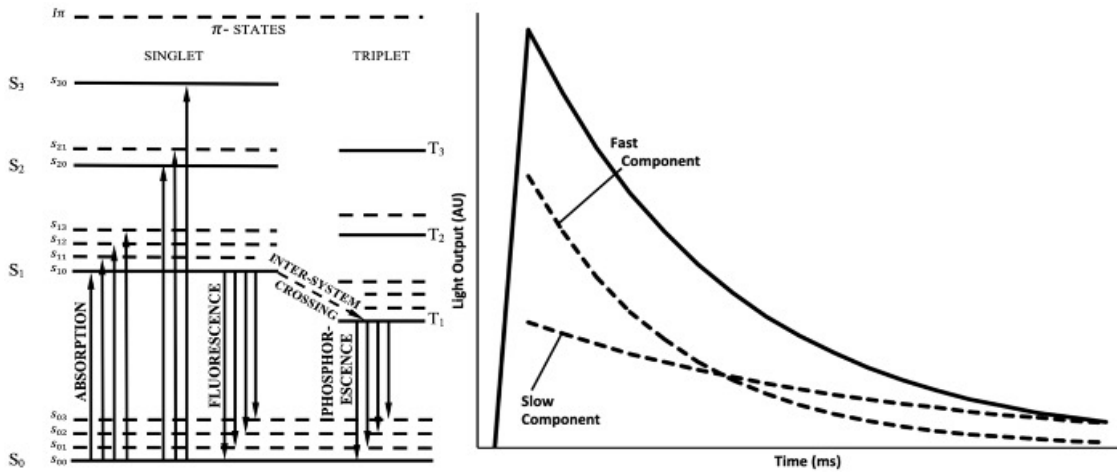


Figure 2.9: (Left) Typical energy levels for a benzenoid π -electron structure in a fluor molecule, with vibrational sub-levels shown as dashed lines. Figure from [64]. (Right) Typical time dependence of the light output from an organic scintillator with fast and slow components illustrated. Fast component due to the rapid $S_1 \rightarrow S_0$ decay (Fluorescence). Slow component due to the delayed $T_1 \rightarrow S_0$ decay (Phosphorescence). Adapted from [63].

few mm - a small Stoke Shift - and the majority of the light will be reabsorbed. The vast majority of the deposited energy is transferred to fluor molecules - via non-radiative dipole-dipole coupling or Förster Transfer [65] - which then scintillates. These primary fluors emit photons at a longer wavelength than the polymer base, increasing the Stoke Shift and the attenuation length.

Usually another fluor is also used, called a secondary fluor or *Wavelength Shifter*. These secondary fluors absorb the emissions of the primary fluors and re-emit the light at a longer wavelength. This shift in wavelength increases the attenuation length even further, allowing more light to propagate through the entire scintillator without reabsorption. The wavelength shift also typically results in greater coupling to the photodetector used; the detection efficiency of the photodetector is wavelength dependant and typically peaks at lower wavelengths than the primary fluor emission. This process is depicted in Figure 2.10 along with the component composition.

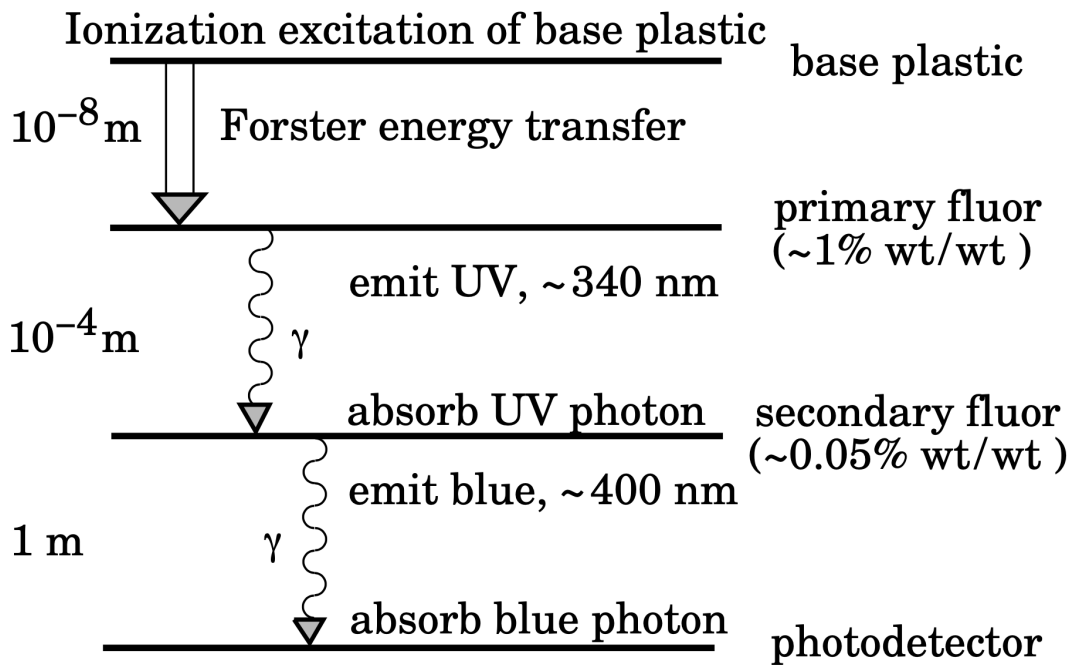


Figure 2.10: The scintillation mechanism of plastic scintillator consisting of a polymer base and two fluors; a primary fluor and a wavelength shifter. Includes typical concentrations, emission wavelengths and transfer lengths [66].

Photodetection

As mentioned, a photodetector is required to turn this wavelength shifted light into a measurable electronic signal; examples of such photodetectors are Photomultiplier Tubes (PMTs) or Silicon PhotoMultipliers (SiPMs). The scintillator is optically coupled to the detection area of the photodetector, typically via a waveguide and/or optical coupling gel, which have a similar refractive index to the scintillator and detection area (e.g. the borosilicate glass of the PMT) to minimise any large changes in refractive index between the 2 components. While the process of light detection in the aforementioned photodetectors is quite different, the same overruling principle applies to both: an incident photon liberates a charge within the detector which is then amplified. This amplified charge is the electrical signal which is measured.

As mentioned in Subsection 1.1.3, the PMT creates an electrical signal from scintillation photons via the photoelectric effect and secondary electron emission; the principle of which will be discussed as an example. The first mechanism of liberating a photoelectron occurs when a scintillation photon is incident on the active area of the PMT, which is coated in a thin layer of a semi-transparent photocathode, typically a bialkali material. The quantum efficiency of this process can be as high as 50% [9] but is usually lower at $\sim 25\%$. This value is limited by the photocathode material currently available and the maximum possible thickness of the applied photocathode layer - the thicker the layer, the higher the photon-to-photoelectron conversion efficiency but a thicker photocathode means more photoelectrons will get reabsorbed. The process of applying the photocathode to the inside of PMT usually means a non-uniform thickness occurs over the active area, resulting in the quantum efficiency varying over the active area, typically decreasing radially from the centre. The quantum efficiency also varies with incident photon wavelength, specific to the photocathode material.

Once a photoelectron is liberated from the photocathode, which is usually held at a high negative potential, the photoelectron is accelerated within the evacuated glass tube of the PMT due to an applied electric field. A focussing electrode is typically used to accelerate the photoelectrons towards the first in a series of dynodes, each at a more positive electrical potential than the previous via a series of potential dividers. The metal dynodes are usually made from beryllium copper with the surfaces oxidized or coated in an alkali antimonide layer, which have high secondary emission coefficients. Upon each primary photoelectron striking this layer, multiple

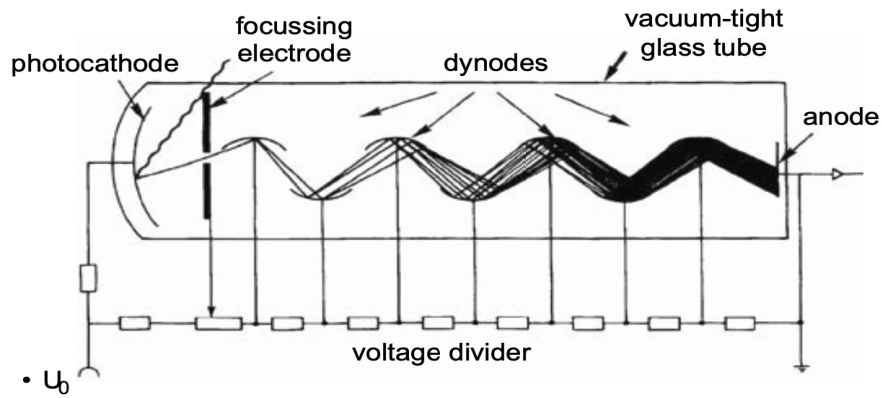


Figure 2.11: The working principle of a Photomultiplier Tube [9].

secondary electrons are emitted from the dynode, typically 3-20 per initial electron [67], depending on the surface layer composition. These secondary electrons are then accelerated, in the applied electric, into the next dynode, with each electron causing more secondary electrons to be emitted. This process is continued for each dynode in the series, multiplying the number of electrons at each stage, until the incoming charge is finally collected at the anode. The process results in a signal photoelectron being amplified into a detectable signal, with the PMT producing gains between $10^3 - 10^8$ [67]. This process can be seen in Figure 2.11.

Chapter 3

3D Printed Gas-Tight Enclosures: Printers and Plastics

The following chapter will discuss the initial work carried out for the 3D printing of Gaseous Detectors (GDs). As discussed in Section 2.1, the most simple design for a GD is the SWGD, with the essential components being: an airtight enclosure; a taut anode wire; and a surrounding cathode structure to produce an electric field. The work carried out in the chapter will discuss the initial focus concerned printing an airtight enclosure, with 3 requirements to ensure:

1. The printed enclosure is rigid and hollow;
2. A central anode wire can be incorporated, and remains taut; and
3. The enclosure is airtight to maintain a constant drift gas composition

all while leaving the possible options to include a cathode structure, later in the process development, unhindered.

3.1 Makerbot: Enclosure Geometries

As previously discussed in Subsection 1.2.1, this initial design and fabrication work was carried out using the Makerbot Replicator 2X - Experimental Printer, and using the associated software, Makerware. The printer had many limitations but was suitable for the initial investigation into viable enclosure shapes, assessing the two main thermoplastic filaments available for use with the Makerbot; ABS and PLA.

ABS was the first thermoplastic to be investigated, as the filament was already widely available at The University of Sheffield. ABS is a primary printing material for the Makerbot, and has many beneficial properties for GD enclosures. ABS is a polymer made of Acrylonitrile, Butadiene and Styrene, with each monomer providing desirable characteristics. Acrylonitrile contributes chemical resistance, heat stability, and high tensile strength, resulting in enclosures that can withstand ageing and degradation; Butadiene contributes toughness and high impact resistance, for robustness; and Styrene provides rigidity for inflexible enclosures, that can resist deformation under possible higher gas pressures.

Taking into account the requirements mentioned above, and after becoming familiar with the limitations and strengths of the FDM process, various methods of producing a 3D printed SWGD were assessed, with the most viable process consisting of the following steps:

1. Create a 3D printed frame, in which an anode wire can be secured at the correct tension;
2. Print the enclosure in an orientation, such that the anode wire is placed in horizontally, due to the vertical nature of the FDM printing process; and
3. Allow for the wire frame to be introduced mid-print, such that the remaining enclosure can be printed around the wire and is held in place when cut free of the frame.

This process was chosen as it would allow for the anode wire to be easily included and reduces the need for additional post-print procedures, with the justification being that a process that requires too many post-print steps negates the objectives of 3D printing a GD and the associated advantages. Unfortunately, this process requires the enclosure to be printed such that the upper "ceiling" layers must be printed over the hollow gas-volume of the SWGD.

A major disadvantage of the FDM process is the difficulty in printing sections over empty space (referred to as overhangs), as the thermoplastic needs to be extruded onto enough support to remain in the correct position. Without these supports, the molten thermoplastic would fall to the baseplate or sag if not supported at each end of the printed length; especially true for ABS due to the high viscosity and slow cooling rate of the molten plastic. This problem is usually negated by the slicing software through the inclusion of an option to add support structures.

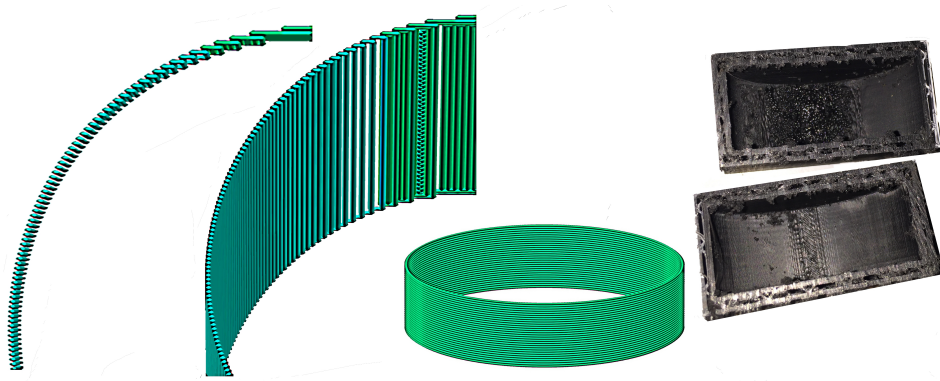


Figure 3.1: (*Far and Middle Left*) Previews of the extruder toolpath for a cylinder printed horizontally. (*Middle Right*) Preview of the extruder toolpath for a cylinder printed vertically. (*Far Right*) Cylindrical enclosure printed horizontally, with the failed ceiling shown.

These are auto-generated, low-density pillars that replace the empty space below an overhang to support the development of the printed overhang. These supports are then cut away post-print or, if multiple extruders are available, dissolvable filament, such as Polyvinyl Alcohol can be used.

Unfortunately, as the gas-volume needs to be unobstructed and fully enclosed, printing support structures within the SWGD is not feasible; and adds considerable constraints to the enclosure geometries achievable. These constraints were yet unknown as predicting the "printability" of a design is not always trivial. The first set of experiments conducted were, thus, the design and fabrication of various possible enclosure geometries to investigate which designs could print correctly and reproducibly; a necessity to ensure each printed detector is consistent and uniform.

As mentioned in Subsection 2.1.2, there are two typical enclosure geometries for SWGDs; planar and cylindrical. The planar geometry, tending to be for drift chambers and large area systems, would require large overhangs to be printed; not possible given the lack of support structures. 3D printing a cylinder is elementary if printed vertically, however, printing horizontally without supports proves complicated as vertical compression often occurs, resulting in oval cross-section; poor wall development; or, more commonly, considerably sagging overhangs. This is due to the only possible toolpath an extruder can take to print a horizontal cylinder. Every slice is a rectangle of the same length but of varying width. Each length of the rectangular slice must print on the previous offset length and thermally fuse. If the extruded length does not print on a previous length, or does not fuse successfully,

the length will fall and sag. This flaw is shown in Figure 3.1.

Given the issues with both planar and cylindrical geometries, many new detector geometries were investigated. Each design was printed in various orientations in attempts to maximise printability. This section will focus mainly around the more successful geometries investigated, namely the designs which took inspiration from the barrel muon system in the CMS detector, shown in Figure 3.2. A small, narrow enclosure was chosen to be printed first, with outer dimensions of $45 \text{ mm} \times 45 \text{ mm} \times 11 \text{ mm}$, using the CMS enclosure dimensions as a rough guideline; the depth of the enclosure was kept to a minimum as this would not effect the formation of the enclosure overhang. A fully flat ceiling wasn't possible using the Makerbot, and thus the first enclosures consisted of a slightly sloped overhang with a smaller flat section and a curved overhang (Figure 3.3). The design was printed with layer height and resolutions of 100 and 300 microns, respectively.

Each enclosure design was printed and cut in half to investigate whether the designed internal structure was printed correctly. The enclosure could have been printed without front and back walls, however it wasn't clear if these would aid in ceiling formation. Enclosure 1 was unsuccessful as the flat section of the ceiling sagged. Enclosure 2 was also unsuccessful as sagging occurred during a large central section of the ceiling, but less so than Enclosure 1. Enclosure 2 was then altered to have a smaller radius of curvature, resulting in smaller vertical portions of the side walls. This was rotated 90° and printed vertically. This resulted in a better print, however some sagging still occurred.

After more failed alterations, it was apparent that a curved or flat ceiling was not possible with the available equipment and thermoplastic. New designs were created that consisted of purely sloped ceilings such that the hollow volume represented a diamond or hexagonal faced prism (Figure 3.4). The height of the printed enclosure was increased to accommodate for this new design as the minimum overhang angle possible was found to be 34° ; calculated from the layer height, line width and the minimum required overlap for overhang formation - found through experimentation. Both these designs printed correctly, however the enclosure with the hexagonal hollow volume was chosen as the appropriate shape to continue with, due to the increase in gas volume that could be achieved and the shape represents a low-poly¹ cylindrical enclosure more closely than the diamond enclosure.

¹A common 3D printing term describing a shape that has been reduced to a polygon with a lower number of faces, e.g. a low-poly sphere could be a dodecahedron.

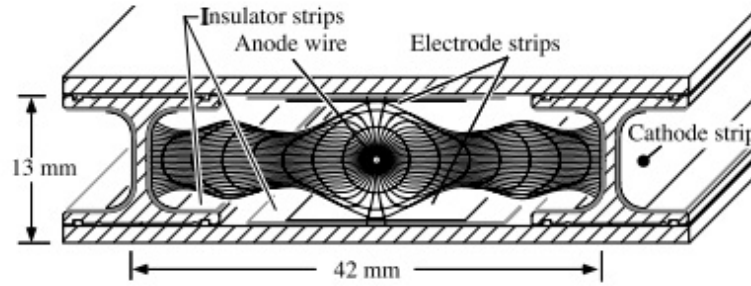


Figure 3.2: Schematic of a SWGD in the barrel muon system of the CMS detector. The dimensions and electric field lines are shown. Figure from [68].

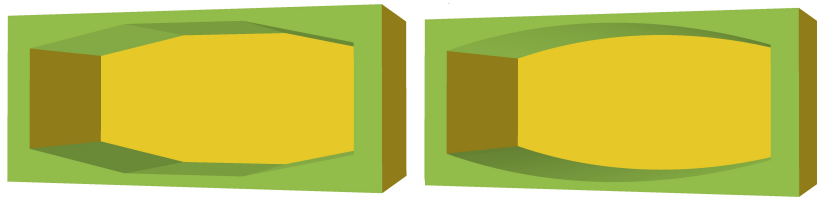


Figure 3.3: Enclosure 1 (*Left*) - Cross-section of the model for the sloped ceiling with small flat section. Enclosure 2 (*Right*) - Cross-section of the model for a curved ceiling.

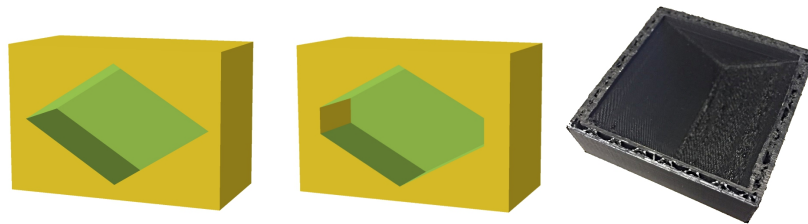


Figure 3.4: Enclosure 3 (*Left*) - Cross-section of the OpenSCAD model for diamond-shaped gas volume. Enclosure 4 (*Middle*) - Cross-section of the OpenSCAD model for a hexagon-shaped gas volume. (*Right*) Top half section of Enclosure 4, printed in ABS using the Makerbot.

3.2 Makerbot: Introducing Anode Wires

The next stage was to incorporate an anode wire running centrally through the enclosure. As mentioned, the best solution was to print a frame that would hold a wire at high tension, running horizontally at half the height of the enclosure. Halfway through printing the enclosure, the print would pause and the baseplate would lower. The frame would be placed onto the baseplate, in the correct position such that the wire runs centrally down the enclosure, and the baseplate would then raise back to the previous position to resume printing. If the enclosure walls are thick enough, sufficient thermoplastic should be deposited to hold the wire in place and, once printing is complete, the wire can be cut free from the frame leaving an enclosure complete with anode wire at the correct tension.

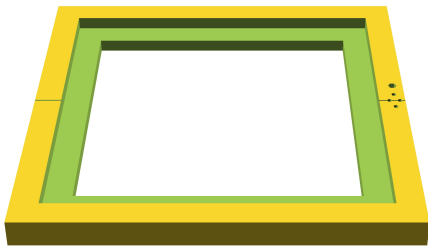


Figure 3.5: The final wire frame design, created in OpenSCAD. The inner "step" is to improve rigidity when applying tension across the frame.

The frame must, therefore, hold a wire at half the height of the enclosure, able to hold the wire at the necessary tension, and ensure the wire is held in the correct position, as wire placement within wired GDs can greatly affect the electric field, and hence detector performance. Many iterations of frame design were created, finally settling on the design shown in Figure 3.5. The main features shown are the vertical holes and horizontal groove. One end of the wire would be inserted into the frame through the holes shown, and secured in the groove using Araldite epoxy resin.

While the resolution of printed features is limited to the extruder nozzle diameter, the resolution of features created by the absence of material is determined by the more accurate stepper motors which control movement of the extruder along the axes, allowing a fine groove to be achieved. The finest, reproducible groove achieved was printed with the Gigabot, at $400 \pm 35\mu\text{m}$ measured between the same points of 2 neighbouring extrusion lines. As each extrusion width is $\sim 400\mu\text{m}$, and given the groove shape created by the extrusion, this actually relates to the ability to hold a $30\mu\text{m}$ diameter wire in the correct position. It should be noted, creating a printed model with this achievable groove resolution is not as simple as removing the desired size groove from the CAD model. There is more complex relationship between

model design and print outcome when concerning absence of material, found through trial and error. This relationship has a heavy dependence on many interlinked factors, such as the printer used, nozzle diameter, layer height (print resolution), print settings (e.g. print speed, nozzle temperature, etc.), slicing software and even the shape of the groove used.

Once one end of the wire was secured, the free end could extend over the frame, placed within the opposite groove, and attached to a load. This load applied an appropriate tension to the wire, corresponding to half the ultimate tensile stress of the wire. The free end wire would then be fully secured onto the frame.

The wire frame was printed and a 100 μm diameter stainless steel wire was attached using the above method. It should be noted that, typically, gold-plated tungsten is the anode wire of choice due to the high tensile strength of the tungsten, and the high conductivity and low reactivity of the gold. The diameter of anodes wire used in SWGDs are also usually much smaller, of the order of 10 μm , for a greater electric field and subsequent avalanche. Despite these facts, stainless steel was suitable for the initial investigations to test whether the FDM process could hold an anode wire in place.

To ensure the wired frame was inserted in the correct position, 4 "pegs" were added to the enclosure model. These pegs were positioned such that each one corresponded to an inner corner of the printed wire frame, ensuring that the frame could only be placed in the correct position.

Although the aforementioned issues, e.g. poor enclosure formation ability, were greatly problematic for the project, one of the greatest downfalls of the Makerbot is the systems dependence on using the MakerWare software and only accepting .x3g print files. The software imposed restrictions on many features which would make the outcome of printing enclosures easier to control, but the use of .x3g hindered the project the most. As the print must be paused midway through to insert the wire frame, control over the print is required. Typically, a printer uses the gcode file format which is a series of commands for the printer to execute, and so the file can be easily edited by added new commands in the appropriate place within the file. The .x3g file format is binary and cannot be edited, leaving only one option; to manually pause the print at the appropriate time, requiring the print to be monitored continuously, manually lower print bed before inserting the wire frame and return the print bed to the correct level to resume the print. This process is unsatisfactory as it caused many issues, as if the correct height was not achieved, the extruder

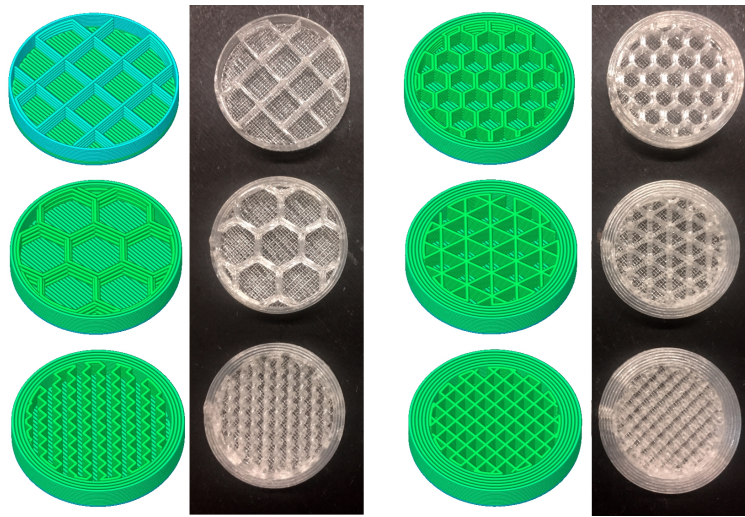


Figure 3.6: Depiction of the different infill percentages and wall number that can be used in FDM and some possible infill styles. Each pair is comprised of the sliced model and the printed counterpart (in PLA). (*Left, top to bottom*) 10%, 1 wall, Rectilinear; 20%, 2 walls Fast Honeycomb; and 40%, 4 walls, Wiggle. (*Right, top to bottom*) 30%, 3 walls, Full Honeycomb; 50%, 5 walls, Triangular; and 60%, 6 walls, Grid.

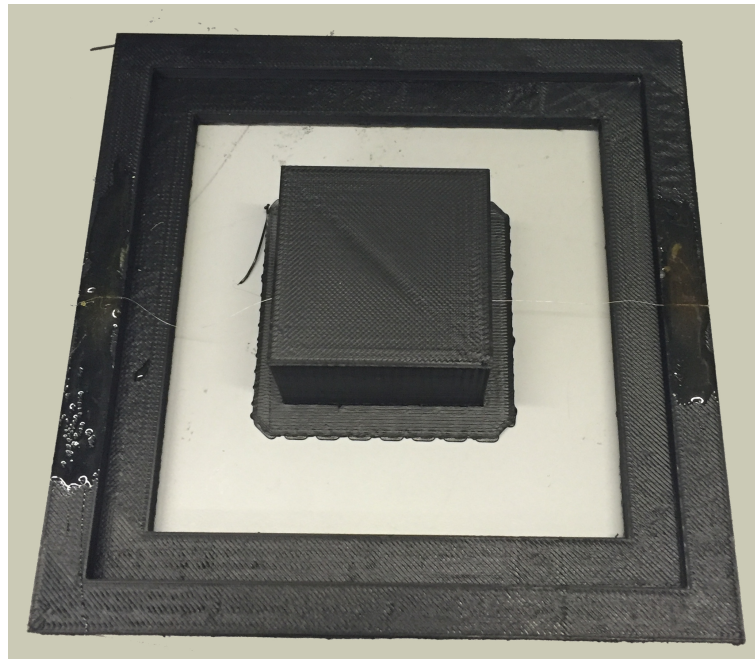


Figure 3.7: The first enclosure to finish printing around an anode wire, although the anode wire has not remained taut. The enclosure is printed on a raft to increase adhesion to the print bed and reduce the chance of warping.

nozzle would move too close to the anode wire, moving it from the correct position and often causing the wire to snap. The task was not impossible and few enclosures were printed around an anode wire but the rate of failure was too high, $> 50\%$, once again negating the reasons to 3D print GDs.

When using FDM, many different settings can be adjusted in the slicing software to alter the print quality, print time and quantity of material used; with two of the most commonly adjustable settings being infill percentage and number of walls. The number of perimeter walls determines the number of continuously printed perimeters along any model boundary, i.e. any wall that separates "solid" model from the environment. Infill percentage determines the amount of thermoplastic printed between these walls, and can be printed in a variety of patterns. Figure 3.6 illustrates different infill percentages, infill patterns and numbers of walls.

Figure 3.7 shows the first enclosure printed around a wire did not grip the wire sufficiently, with the wire able to slide through the enclosure with ease; likely due to the fact that the enclosure was printed with a 15 – 20% infill pattern and, thus, not enough plastic was extruded to supply sufficient friction to secure the anode wire. A new enclosure was printed with 100% infill (the hollow central volume remaining), such that the enclosure walls were solid, and the anode wire was successfully gripped, although this could be freed with a small force. This was sufficient proof that an anode wire could be secured in a printed enclosure, with obvious improvements such as increasing wall thickness still to be investigated.

Unfortunately, requiring 100% infill and relatively thick walls to grip the anode wire is far from ideal, as this increases print speed and the quantity of thermoplastic used. Inspection of the higher infill enclosure also revealed poor enclosure "ceiling" formation and, through observing repeated prints, was found to be caused by the solid thermoplastic mass retaining more heat; staying molten for longer. This resulted in the excessive amount of thermoplastic sagging and deforming away from the desired design. As a greater infill is required to grip the anode, yet adversely effects the print quality, the solution is to print the enclosure using a low infill up until the layers that would be printed directly below and above the wire, which would be 100% infill, then the lower infill would continue; a solution impossible for the Makerbot.

3.3 Makerbot: Printer Limitations and The Requirements For Change



Figure 3.8: A wire frame printed using ABS on the Makerbot, showing the extent of the warping issue. The wire frame should be polygonal, with the base flat to the surface.

While the method outlined above was developed using the iterative process of rapid prototyping, through sensible observation and appropriate redesign, the success of the project was also dependent upon the performance of the printer used, and the limitations of the Makerbot had become evident and detrimental to the progress of the project. Given the decision to print an enclosure using two different infill percentages, as discussed above, the issues with MakerWare and printing .x3g files arose again. The inability to edit print files meant combining two different print settings into the same print file was impossible and thus any further development using the Makerbot would be difficult.

As well as the issues with the associated software, the Makerbot prints were inconsistent. Almost all the models created were subject to serious warping from the bottom corners (Figure 3.8). This is a limitation of ABS and is due to the high temperature ($\sim 250^{\circ}\text{C}$) required to print the material and the subsequent cooling; the quicker the cooling, the more exaggerated the warping. The use of a heated bed (above 100°C) and printing a raft is a typical solution to this problem. The heated bed reduces the rate of cooling and also allows the ABS to remain attached to the print bed and not peel away. The raft is an optional additional structure which is printed before the model. The raft has a larger surface area to allow for increased adhesion to the print bed, and the model is subsequently printed onto this raft and removed after printing (Figure 3.7). The Makerbot struggled to achieve printing

models without significant warping, due to poor thermoplastic-print bed adhesion, even after many different print configurations and temperature setting combinations were tested, resulting in irregular prints that did not resemble the initial design.

Another shortcoming of the Makerbot was the small print area, however, this is project-specific. With all SWGDs, the field must be relatively constant along the anode wire to ensure consistent signal production independent of position. Unfortunately, this is not the case close to the edges of the enclosures of GDs where the geometry, and thus the electrode distribution, changes abruptly. With the makerbot, the longest SWGD possible was 246 mm, however, with the plan to introduce a wire frame midway through the print, the maximum length was reduced significantly, posing the risk of major operational problems with any 3D printed SWGD.

3.4 Gigabot: Enclosure Geometries

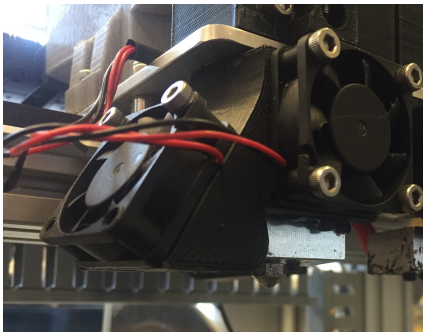


Figure 3.9: The additional cooling fans direct air down onto the thermoplastic immediately after extrusion, causing faster cooling.

The decision was made to replace the Makerbot with another FDM printer which had a large print volume and used firmware that would print gcode files. After researching the large-scale commercial printers in the market, the Gigabot was chosen due to achievable resolution and the relatively low cost, as well as many other appealing features. The Gigabot, like the Makerbot, is a dual extrusion, FDM printer that can achieve the same height and width resolutions, however, the Gigabot cannot print in ABS and instead prints mainly PLA. Printing with PLA

does come with many advantages for GD enclosures as PLA produces models with no, or very little, warping and has significantly less outgassing than ABS; $\sim 40\%$ less outgassing [69]. The Gigabot has the capability of having wider extrusion nozzles fitted so that the rate of extrusion is dramatically increased, meaning larger prints require less time, and the purchase of the Gigabot came with a license to the Simplify3D software. An important feature of the Gigabot is the cooling fans placed next to the extruders (Figure 3.9), which cool the thermoplastic faster and immediately after extrusion, the importance of which will be discussed later.

As the 3D printer, slicing software and thermoplastic had been replaced, too many variables had changed to rely on previous results; thus it was necessary to reproduce, or redevelop, the work carried out so far. As with all thermoplastics used throughout this thesis, the initial step of using a new thermoplastic is to find the optimal print settings required to successfully print any designed models. This is a lengthy process, requiring the fine tuning of a multitude of print settings, such as print speed, temperature, mass flow, etc..

Once the optimal print settings for PLA were found, the same initial steps were taken to narrow down the best geometry for the enclosure. As with the Makerbot/ABS, a horizontally printed cylinder was not possible due to this being a flaw with the FDM process rather than that of the printer and thermoplastic.

Some initial angle tests were carried out to determine the limit at which the Gigabot can print and form overhangs, with the resulting print shown in Figure 3.10. 45°, 40°, 35°, and 30° overhangs (from horizontal) were printed with almost perfect overhang formation occurring and every angle, with only slight deformation at the steepest angle. This matched the performance of the Makerbot, but did not require the need for any additional print features to prevent warping. The same enclosure models which were printed on the Makerbot were successfully reproduced on the Gigabot, with a far lower fail rate (< 5%) and the enclosures could be printed much longer. A comparison of the "ceiling" formation from the Makerbot in ABS and the Gigabot in PLA can be seen in Figure 3.12.

The hexagonal volume design was initially going to be kept as the primary enclosure, however, a surprising discovery was made regarding horizontal overhangs (0°) while investigating other designs. As discussed earlier in this section, a key feature of the Gigabot is the cooling fans placed next to the extruders, which allows the thermoplastic to be cooled faster after extrusion.

A major downfall of the Makerbot in the printing of an enclosed enclosure was the inability to print flat enclosure "ceilings" as the ABS would sag. By altering the settings of the Gigabot, such as flow rate and cooling fan speed, PLA can be extruded such that the thermoplastic is heated to the temperature required for extrusion, but is then cooled sufficiently to reduce the viscosity after extrusion to prevent almost all sagging. This allows the PLA to be printed between two supporting structures to form a horizontal "ceiling"; an important discovery for more planar geometries to be possibly printed.

A test model was designed to investigate the maximum distance at which the

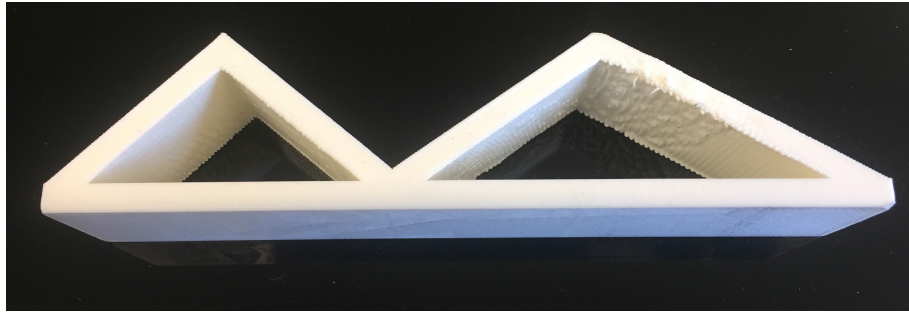


Figure 3.10: Overhang formation test printed in PLA on the Gigabot. The angles tested are 45° , 40° , 35° , and 30° (decreasing from left to right).



Figure 3.11: Horizontal overhang test, printed in PLA on the Gigabot. (*Top, left to right*) 10 mm, 30 mm, 50 mm, 70 mm, and 90 mm. (*Bottom, left to right*) 50 mm, 80 mm, 60 mm, 40 mm, and 20 mm. The 50 mm distance is repeated on both sides, but only to complete the length.

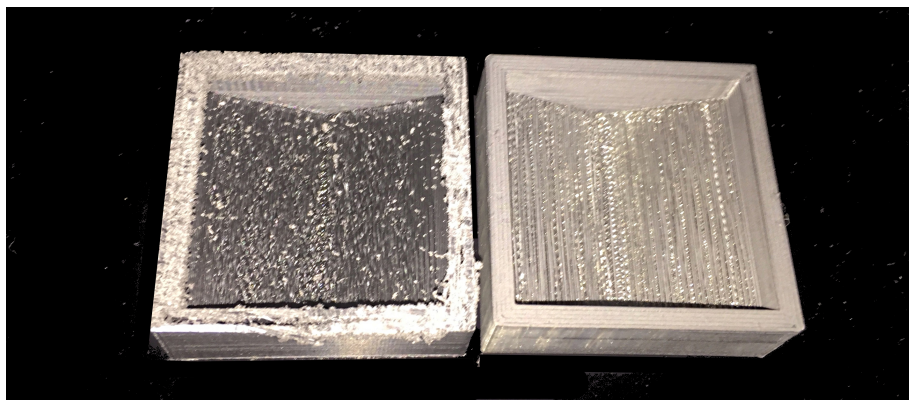


Figure 3.12: (*Left*) "Ceiling" of hexagonal volume enclosure printed by the Makerbot in ABS at 100% infill. (*Right*) "Ceiling" of hexagonal volume enclosure printed by the Gigabot in PLA at 100% infill.

Gigabot could fully form a horizontal overhang. The distances tested were 10 mm-90 mm, increasing in 10 mm intervals, and the resulting print is shown in Figure 3.11. As can be seen, horizontal overhangs can form up to 80 mm with the only significant sagging occurring at 90 mm, although it should be noted some slight sagging has occurred at 20 mm but not at greater distances.

3.4.1 Tessellating, Triangular Tubes

As mentioned in Subsection 1.2.1, one of the possibilities that comes with 3D printing detectors is the ability to investigate new geometries and, as mentioned in Subsection 2.1.2, GD geometries are typically, solely planar or cylindrical/tubular in design, depending on the application and method of determining particle position, i.e. drift time or simple trigger, respectively. Throughout the investigation into printable enclosure geometries, it had become apparent that the focus should be on tubular designs, as these will be simpler to print and have a larger scope for more interesting designs.

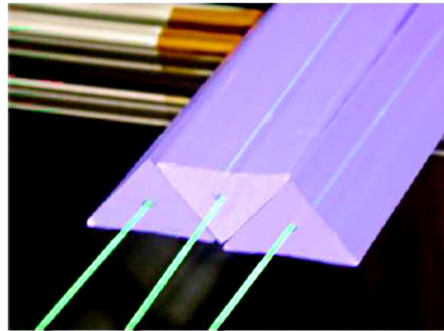


Figure 3.13: Triangular, tessellated scintillating bar used in the MINER ν A experiment.

Arrays of cylindrical GDs, for applications such as muon tracking (as illustrated in Figure 2.5) are built up of many layers (possibly in x-y super-layers), but where only one trigger per muon per layer can occur, and thus positional resolution is limited by the number of detector layers. In Subsection 2.1.1, the principles of GD operation are discussed, whereby it is shown that total number of primary ion pairs, created by a charged particle transversing through a GD, is proportional to the path length of the charged particle through the detector volume.

This phenomenon is paralleled by the passage of a charged particles through scintillator, whereby the amount of scintillation, or equally the final signal amplitude, is proportional to the path length of the charged particle through the scintillator; a property which has already been exploited by the MINER ν A detector [70] and Electron-Muon Ranger at the MICE experiment [71]. These detectors use an array of tessellating, triangular scintillating bars as a tracking calorimeter that allows for

track reconstruction, see Figure 3.13. In this array, multiple bars per layer can be triggered, and the ratio of signal amplitudes between the triggered bars gives the ratio of the path lengths travelled by the charged particle in each bar, increasing the positional information acquired from each layer.

With the possibility to 3D print new detector geometries and complex cathode designs, this tessellating, triangular tracker could be paralleled by GDs using the same property that signal magnitude is proportional to charged particle path length. A triangular tubular enclosure was designed using OpenSCAD, complete with gas-flow holes and was successfully printed without errors, see Figure 3.14. It should be noted, the printed enclosure in Figure 3.14 is a cross-sectional print, and not a complete print that has been cut in half post-print. A complete print was originally printed, and cut, to show successful triangular formation, however, the process of cutting an enclosure in half causes considerable frictional heat which melted the PLA along the cut walls. This resulted in poor photographs and so a cross-sectional print has been inserted as a replacement to show the correct formation, which was consistent between the prints.

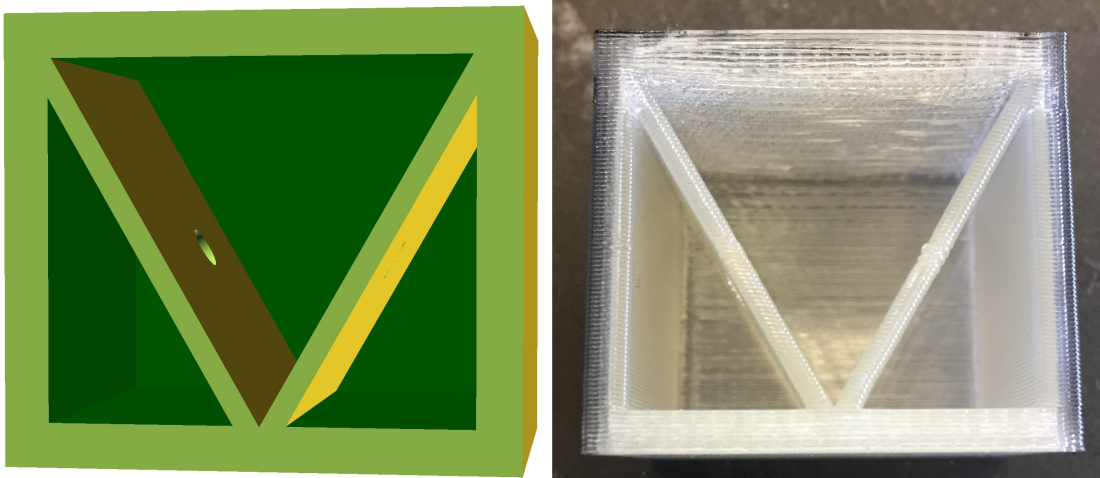


Figure 3.14: *(Left)* Cross-section of the OpenSCAD model for the triangular enclosure. *(Right)* A 3D printed cross-section of the design to show the internal structure has printed successfully.

3.4.2 Nozzles, Resolutions and The Volcano

Hitherto the main focus on enclosure geometries has been based around the shapes capable of being printed by each printer and the FDM process, however, the various print settings that can be chosen have been largely omitted from discussion. Print settings such as printer temperature, print speed, fan speed, etc. have been constantly varied and fine tuned, throughout the work previously discussed, to ensure the best possible prints and the importance of certain settings will be discussed later in the chapter when considering gas-tight enclosures, however, some variables should be brought to attention now, mainly extruder nozzle size and printer resolution.

Resolution, within the realms of 3D printing, refers to the printed layer height of each 3D printed slice and is generally dictated by the minimum step able by the z-axis motor, but is controlled through the slicing software, in this case Simplify3D. Simplify3D has 3 preset resolutions, given as Standard (0.3175 mm), Higher (0.2223 mm) and Highest (0.1510 mm) resolution, although almost any value can be manually entered. It should be noted that an increase in print resolution also increases the print time as more layers are required for each print.

Nozzles are the metal extruder ends, where the molten thermoplastic exits the printer hot-end. These nozzles can be easily replaced or upgraded, usually being swapped for tougher materials due to wear, but do also vary in nozzle diameter to control the thickness of the extruded material. The standard nozzle diameter for most printers is 0.4 mm, however, much finer nozzles (down to 0.15 mm) can be used, as can much thicker nozzles (up to 1.2 mm) by upgrading the printer hot end to The Volcano - a hot-end created by E3D which features a much longer heater block, designed to heat thermoplastics at a higher rate, allowing for much faster print speeds but at the cost of lower resolution [72].

Thus far, all designs have been printed using the standard nozzle size and resolution, which tend to be shared across most printers - it would be ideal for the final detector designs to be printable on most machines, without the requirements for upgrades or printers capable of low resolution prints. Nonetheless, for completeness, an experiment was carried out to observe the effect of resolution on enclosure printability, and the possibility of the much greater print speeds that come with using the Volcano should be investigated.

In this experiment, the same horizontal overhang test model used for Figure 3.11 was reprinted while varying the nozzle diameter and print resolution, with the

results seen in Figure 3.15. The first two overhang tests, (*Top and Middle*), were carried out with the same standard 0.4 mm diameter nozzle but printed using the Higher and Highest resolutions, respectively. From Figure 3.15, it can be seen that these increases in print resolution have resulted in much poorer overhang formation as not enough plastic has been deposited to self-support.

For the final overhang test, (*Bottom*), a Volcano extruder was attached to the Gigabot with a 1.2 mm nozzle. Using this new nozzle required many of the print settings to be re-tuned for successful printing to occur, such as filament feed-speed, print speed, extruder temperature, etc. with the main difficulty being in finding the new possible print resolutions, as all present resolutions were too low for the Volcano to print with.

From Figure 3.15 it can be seen that, despite the arduous task of re-tuning the printer settings, the best print possible could not match the overhang formation previously seen in Figure 3.11, however, did come close. The main issue seen from the Volcano prints though was poor line-line fusion, where the lines of filament printed to create a single layer would not fuse to neighbouring lines successfully, though layer-layer fusion was standard. The cause of this issue was found to be due to the larger extruded lines overlapping less and cooling differently than with smaller nozzle sizes. This would unfortunately prove problematic when creating airtight enclosures and thus the Volcano extruder was no longer used in the project.



Figure 3.15: Reprints of the horizontal overhang test seen in Figure 3.11 with (*Top*) 0.4 mm nozzle and a higher resolution of 0.2223 mm, (*Middle*) 0.4 mm nozzle and the highest resolution of 0.1510 mm, and (*Bottom*) 1.2 mm nozzle at standard resolution of 0.7350 mm.

3.5 Gigabot: Introducing Anode Wires

With the enclosure design recreated on the Gigabot, with greatly increased success rates and reproducibility, the next stage was to resume with the introduction of an anode wire. New wire frames were printed using the same design, again with a much higher success rate and with no warping. This is illustrated in Figure 3.17 as a comparison to Figure 3.8.

As mentioned in Section 3.2, the aim was to create a print file that would print an enclosure using a low infill up until the layers directly below and above where the wire would be positioned, when the printer would change to 100% infill. At the halfway point, the printer would pause, lower the baseplate and wait for the wire frame to be in place, before raising the baseplate again to continue the printing of the remaining layers, firstly at 100% and then again at the reduced infill percentage.

As the Simplify3D slicing software produced a gcode file that was a list of subsequent commands to be carried out by the printer, and the design is printed layer by layer, the first block of gcode corresponds to the first layer, the second block to the second layer, etc.. By altering the settings in Simplify3D, two sets of gcode were created; one for 20% infill and one for 100% infill.

After learning how to read gcode commands, the gcode corresponding to the 10 layers surrounding the anode wire were deleted from the 20% infill file and the corresponding layers from the 100% infill file were inserted. The combined file was then edited to allow the print to pause after the final layer before the wire needed to be introduced. Two commands were added; one to lower the baseplate by 200 mm and one to pause the print for 60 seconds - adequate time to insert the wire frame into the correct position.

The edited gcode file was executed and an enclosure was successfully printed around an anode wire. When cut free from the wire frame, the anode wire was held without moving and, thus, maintaining the wire tension inside. The end of the successfully printed wired enclosure is shown in Figure 3.16, again proving this could be accomplished with the new printer and plastic.

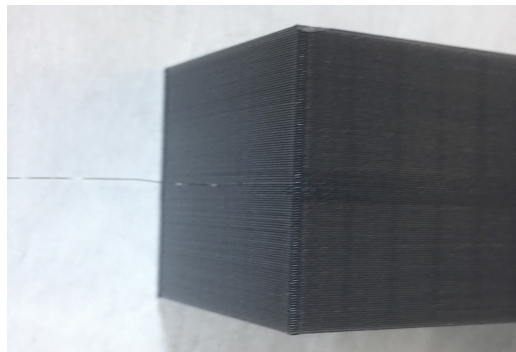


Figure 3.16: An enclosure successfully printed around an anode wire.

It should be noted at this point that the lower 20% infill used for the layers not immediately surrounding the anode wire was chosen simply to reduce the amount of thermoplastic used throughout the experiments but ensuring enough infill is used to ensure correct formation. It was foreknown that the many print setting variables, such as infill, would directly affect how gas tight the printed enclosures are, and the fine tuning of these parameters were being tested in parallel to find the optimal print parameters to maintain gas composition while maximising print speed and minimising material costs, and will be covered later in this section.

The enclosure printed was designed to have 3 mm thick walls (enclosure thickness) and appeared to sufficiently grip the wire in place, although through a small amount of force the wire could be removed. As this is not ideal, structures of varying thickness were printed around an anode wire to test the minimum enclosure thickness required to adequately grip an anode wire without the risk of the anode wire easily being removed. Test blocks, representing the enclosure walls, were printed with increasing thicknesses; ranging from 4 mm - 16 mm, in 2 mm intervals, and printed at 100% infill. The values chosen represent enclosure thicknesses of half the value, as the wire must be pulled away from both sides of the enclosure to be freed. A taut anode wire was introduced midway through printing as described previously, however, the stainless steel wire used previously had been replaced by tungsten wire of the same diameter, 100 μm . Each block was then held in place and a load was attached to the wire. The load was then increased, in discrete increments, until the wire was freed from the PLA.



Figure 3.17: A wire frame printed using PLA on the Gigabot, showing no warping. The slight curve in the corners is slight damage from the trouble removing the model from the print bed, due to the superior adhesion.

Block Thickness, mm	Minimum Force to Remove, N
4	Did not grip
6	< 0.98
8	2.70 \pm 0.25
10	3.68 \pm 0.25
12	6.62 \pm 0.25
14	6.62 \pm 0.25
16	6.62 \pm 0.25

Table 3.1: A table of results for the minimal force required to remove an anode wire from an enclosure.

The block of thickness 4 mm did not initially grip the wire and so yielded no results. The 6 mm block (equivalent total enclosure thickness of that of Figure 3.16), gripped the wire again but was removed with a small, applied load. As expected, the results show a positive correlation between the thickness (i.e. the amount of material holding the wire) and the minimum force required to remove the wire. The greater thicknesses do show the same load was required to remove the wire, however, this trend is most likely due to the discrete load values used in the experiment, with the true minimum force required lying between the value shown and the previous load. More accurate results were not required as the data collected was sufficient to move forward with the ideal enclosure design. From this point, a few solutions are available to maximising the grip on the anode wire. Any thickness above 5 mm (each side) should supply enough friction, and thus the enclosure ends could be made thicker as a whole; the enclosure ends could increase in thickness converging on the wire, see Figure 3.18 (*left*); or, alternatively, new materials could be tested to find a thermoplastics with larger coefficient of static frictions.

3.5.1 Alternative Thermoplastics

As the work concerning enclosures had already been redone with PLA, and having given positive results, this work was not going to be repeated again with other plastics, especially given the time required for the tests. Instead, a multi-material enclosure was designed, see Figure 3.18 (*right*), utilising the dual-extrusion capabilities of the Gigabot. In this design, PLA would be used for the majority of the enclosure, up until the point surrounding the anode wire, where the secondary plastic would be used to print a seal around the wire that would also not impinge on the gas-tightness of the enclosure. Unfortunately, most thermoplastics are designed

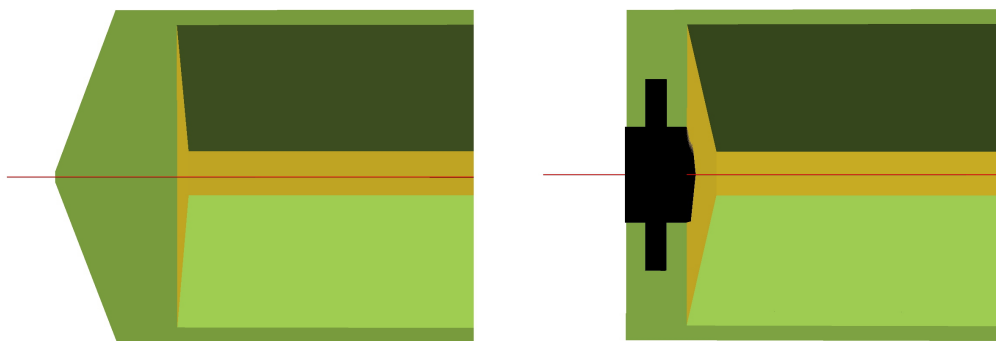


Figure 3.18: (*Left*) - Cross-section of the OpenSCAD model with a converging end, to be printed in PLA. (*Right*) - Cross-section of the OpenSCAD model with multi-material design.

to have a low coefficient of friction to allow for easier flow through the extruder and so a variety of different thermoplastics were selected.

NinjaFlex was the first, secondary thermoplastic to be tested. NinjaFlex is a flexible, rubbery Polyurethane (TPU) based thermoplastic designed by NinjaTek [73], created for the printing of seals, gaskets and shock absorbers. From initial assessments of the material, it was clear that NinaFlex would produce a higher level of friction to grip the anode wire, without compromising the later gas-tight studies. NinjaFlex was a desirable material to work with, as the successful integration of the rubbery plastic into enclosure prints would open up the possibility to printing larger area enclosures where unsupported "ceilings" could not be printed, but instead separate enclosure tops could be printed with a rubbery seal, to be attached after printing. Unfortunately, after little experience with the thermoplastic, the issues around printing with NinjaFlex were evident. Inconsistencies between prints were a regular occurrence, but the main issue that consistently arose was the difficulty in achieving constant extrusion, and finishing a print. NinjaFlex was tested using settings well-within and outside the manufactures guidelines for print speed and extruder temperature, however, even using a large temperature range and at print speeds 5-10 times slower than those given by NinjaTek, the rubbery filament would not feed into the extruder properly, see Figure 3.19, leading to a failed print.

The next secondary thermoplastic tested was the Alloy 910 by Taulman3D, a nylon based thermoplastic designed to have a high tensile strength, compared to other thermoplastics [74]. Nylon typically has a lower coefficient of friction compared

to other plastics, however, this thermoplastic was tested for wire grip as the Gigabot only has the capability of extruding 2 different thermoplastics per print, and Alloy 910 was being investigated, in parallel, as a means of printing stronger gas inlets; an issue discussed later. Unfortunately, the Gigabot struggled to maintain the much higher temperature required to print with Alloy 910 (250 – 255°C) and a higher percentage of prints failed due to thermal runaway. Due to this inconsistency, Alloy 910 was ruled out as a possible solution to both problems.

The final secondary thermoplastic to be tested was PolyMax™ PLA by PolyMaker, a "nano-reinforced" PLA created to print like PLA but have the impact strength of ABS [75]. As PolyMax™ is a variant of PLA, this was a desirable thermoplastic to test as it could replace the primary PLA altogether, freeing up the second print extruder for other print features to be developed in the future, such as cathodes made from conductive filament. The results, of the PolyMax™ tested, however, showed a significant decrease in friction, unable to grip the anode wire at the highest enclosure thickness.

This result initiated a new investigation into the various different PLA samples available, sourced from a range of manufacturers, to understand the inconsistency between different PLAs. The investigation found that all the PLA samples that failed to grip the anode wire completely all shared a common feature; the filaments had an increased smooth, glossy finish which significantly reduces the coefficient of friction of the PLA. The source of this inconsistency between plastics is due to the different thermoplastic compositions from each manufacturer. Some samples, such as the PolyMax™ PLA are actually polymer blends, containing < 30% acrylic polymers, while other samples contain high percentages of additives, which will be mentioned more in the next section.

The study into using a secondary, alternative thermoplastics for increased thermoplastic to wire friction ended with the conclusion that, despite the variety of

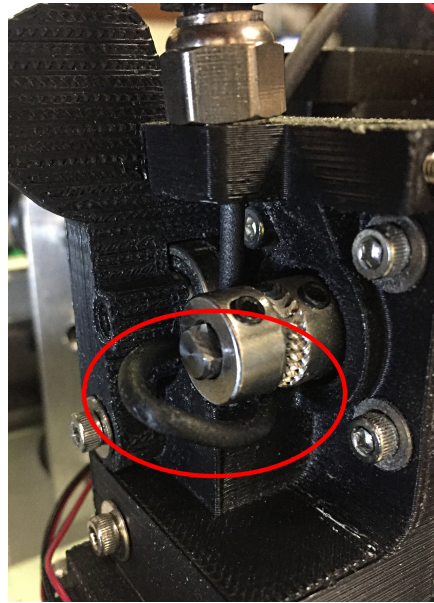


Figure 3.19: Photograph of the recurring issue with NinjaFlex. Failure to feed into extruder correctly, due to the rubbery nature of the material. The failed feed has been highlighted by a red circle.

thermoplastics available, using the initial PLA with a greater enclosure thickness would be far easier and create more consistent prints. The investigation into various PLAs also resulted in finding the PLA from e3D, the maker of the Gigabot, supplied the best thermoplastic-wire friction and became the primary supplier of all future PLA.

3.6 Low Background PLA: Gamma Spectroscopic Analysis

As PLA had been selected as the best thermoplastic available to produce enclosures, the next stage was to ensure the thermoplastic was relatively radio-pure, as building a detector from material with high gamma-emissions would increase background, and possibly damage the detector. There is high interest in radio-pure materials with regards to HEPP instrumentation, and being able to 3D print with a relatively radio-pure material could have great benefits to the field. While the PLA from re:3D is guaranteed to not contain any heavy metals, other gamma emitting isotopes could be present and should be investigated.

The first PLA to be tested was the silver coloured PLA, made by COEX but sold by re:3D. Approximately 503 g of PLA was printed as a Marinelli beaker, to fit around the Roseberry Ultra-Low Background Germanium detector located at Boulby Underground Laboratory. The Roseberry detector has a 900 g crystal and a relative efficiency of 60% ². Data was taken for almost 21 hours (75579 s) and the isotope peaks investigated, with the spectrum shown in Figure 3.20, background subtracted.

From analysing the spectrum, the majority of the peaks correspond to isotopes from the thorium and uranium decay chain, such as lead-214 and bismuth-214, which is expected to be observed. Contamination from these decay chains can come from many sources, with a notable possible contribution the tendency of a plastic to accumulate radon progeny from the air. The uranium and thorium in the rocks or mine walls is the source of this radon, as the inert gas has a high mobility and can easily diffuse out from the rocks.

²The figure-of-merit relative efficiency is in reference to the ratio of counts per second of the cobalt-60 1332.5 keV peak between the tested detector and a 3 x 3 inch NaI(Tl) detector, when a Co-60 source is placed 250 mm away, on the axis of the respective detectors [76].

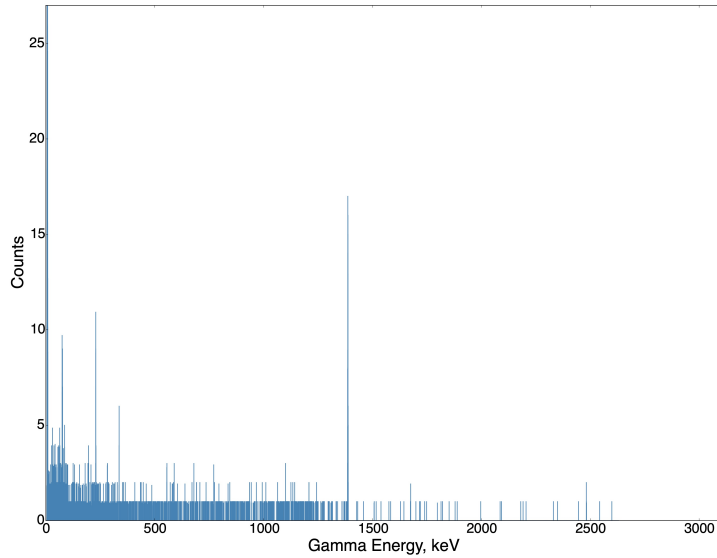


Figure 3.20: Results of the Roseberry ultra-low background gamma spectrometry graph of Silver PLA taken over 75579 seconds (background subtracted), with the potassium-40 peak at 1460 keV clearly seen.

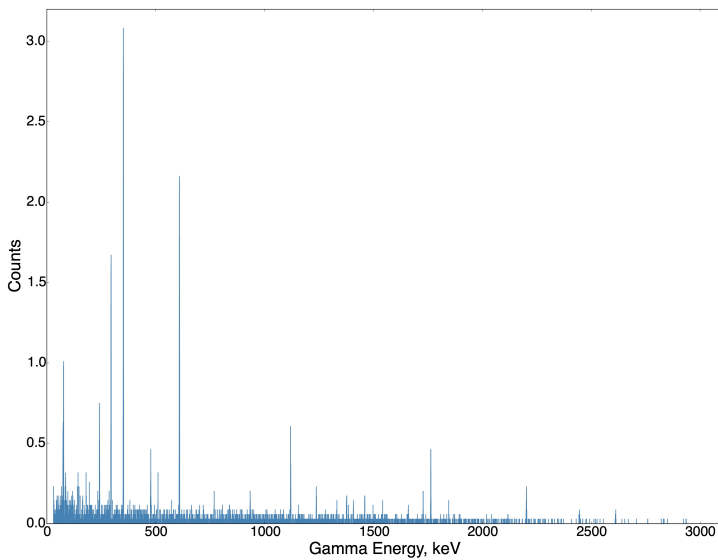


Figure 3.21: Results of the Merrybent ultra-low background gamma spectrometry graph of Natural PLA taken, normalised to 75579 seconds (background subtracted), with no potassium-40 peak observed. The majority of the strongest peaks are attributed to the uranium-238 decay chain, predominantly bismuth-214 and lead-214.

The only major peak observed is one corresponding to potassium-40, with the PLA being the only possible source. Using the data taken, the energy specific efficiency of the detector and the geometric efficiency (due to the shape of the Marinelli beaker), the potassium-40 component of the radioactivity was calculated to be 310.5 ± 53.1 mBq/kg of PLA. While still relatively low, this level of radioactivity is significant. Not necessarily high enough to rule out the silver PLA as appropriate detector material, however, a lower radioactivity replacement should be considered.

As can be seen from Figure 3.22, the chemical structure of PLA contains only carbon, hydrogen and oxygen, thus a large amounts of potassium must be come from another sources which is added to the thermoplastic. Many plastics, including thermoplastics, can contain $\leq 10\%$ additives beyond the basic polymer structure such as antistatic agents, stabilisers and flame retardants, which are required for the plastic to have the correct properties, however, some additives have only an aesthetic function, such as dyes and pigments.

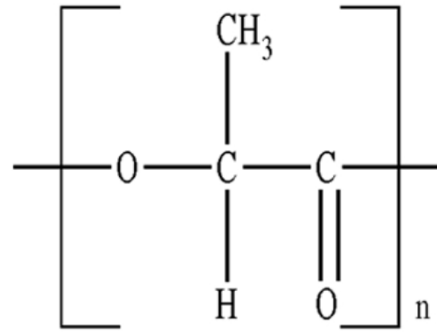


Figure 3.22: The skeletal structure of a repeating PLA monomer [77].

Unfortunately, the data sheet [78] provided for the PLA does not include any details on any additives used and so the source of the potassium is unknown. Research into other PLA compositions did provide some evidence to narrow down the potassium source, as the investigation revealed some of the most common PLA additives used as stabilisers and antistatic agents, e.g. N,N'-ethylene bis(stearamide), which do not contain any potassium. All mentions of pigments and dyes, however, are stated without any specificity in the data sheets, leading to the hypothesis that these additives are the source of the potassium in the tested silver PLA.

To determine whether the potassium is within the silver pigment added to the PLA, a reel of natural (uncoloured) PLA was purchased from re:3D and another beaker was printed. This time to save on plastic and time, a full Marinelli beaker was not produced, but instead only the inner section was printed to fully surround the Germanium detector; a geometry that yielded a geometric efficiency $\sim 2.5\times$ greater than that of a Marinelli beaker (using cobalt-60 at 1332.0 keV as the standard). The printed piece consisted of 144 g of natural PLA and gamma spectroscopic analysis was performed on the Merrybent Ultra-Low Background COAX Germanium

detector, also located at Boulby Underground Laboratory. The Merrybent detector is much larger than the Roseberry, with a 2 Kg crystal, and has a relative efficiency $\sim 2.67\times$ greater at 160%. Data was also taken for a significantly longer time, at almost 328 hours (1180462 s). The results from the run are shown in Figure 3.21, background subtracted.

As different detectors were used, direct comparison of activities is difficult, especially due to the different geometric and relative detector efficiencies. The counts in Figure 3.21 have been normalised to those in Figure 3.20 with regards to runtime and crystal mass to aid comparison, however, as the main consideration is the presence of isotopes, comparisons of activity is not paramount. Although, it should be noted that the Merrybent detector is more efficient overall, with a greater relative efficiency and geometric efficiency of the sample, and thus would be expected to yield a higher number of counts for potassium-40, which is not observed.

Analysis of the results shown in Figure 3.21 reveal no significant potassium peak, with the only peaks observed once again coming from uranium and thorium chains. More of these peaks are observed in the Natural PLA sample compared to the Silver PLA, however, the cause of this is attributed to higher exposure to contaminant prior to data being taken, as the initial Silver PLA Marinelli beaker was transported to the mine under more sterile conditions. Also, any additional peaks observed in the Natural PLA and not in the Silver PLA must be from contamination, as the only difference between these thermoplastics is the silver pigment. There is a small chance that the potassium peak seen in the Silver PLA sample could be due to contamination prior to the data acquisition, however, given the stringent printing and transport conditions of the initial sample, this is unlikely.

Given the spectra of the two samples, and the lack of potassium-40 in the Natural PLA, it can be stated with relative confidence that the pigment used in the Silver PLA is a considerable source of potassium-40; the only significant radioisotope observed and determined to be within the original composition of the sample. The Natural PLA sample exhibited significantly lower counts throughout the tested energy range, and possibly allowing Natural PLA to become a contender for cheap, low-activity detector materials in the future, however, further investigation is undoubtedly required. A notable distinction has been made between thermoplastics containing some additives, such as pigments, and those which do not, and so, the use of pigment-containing PLA within this work carried out in this thesis will cease and only Natural PLA will be used for the further development of 3D printed detectors.

3.7 Gigabot: Gas-Tight Enclosures

Using the Simplify3D slicing software, there are 5 main parameters which could directly affect the gas tightness of the enclosure. These are:

- enclosure thickness, i.e. barrier sizes;
- infill percentage, i.e gas cell sizes within the walls;
- number of walls (exterior and interior), i.e. number of completely printed walls;
- number of top and bottom layers, i.e. number of completely printed "floors" and "ceilings"; and
- infill overlap, i.e. level of gas tightness between gas cells and walls.

The first settings to be tested were enclosure thickness, infill percentage and number of walls. 30 small, hollow test cubes, with an internal void of 30 mm x 30 mm x 20 mm ($x \times y \times z$) were printed together to ensure all cubes were printed under the same conditions, i.e. no variations in print quality due to slight differences in initial print bed height, initial room temperature, etc.. The values used to investigate the effects of these parameters are:

Infill Percentage (%):	25, 50, 75, 100
Enclosure Thickness (mm):	2, 3, 4
Number of Walls:	2, 3, 4

As the number of walls no longer matter when 100% infill is used, only the enclosure thickness was varied and 3 walls were used. A subset of the test cubes are shown in Figure 3.23. It should be noted now, that during printing it was evident that all cubes with an enclosure thickness of 2 mm produced homogenous cubes, as the minimum of 2 interior and 2 exterior walls left little room for infill and, thus, were effectively all 100% infill. Only one cube of enclosure thickness 2 mm was used and tested. For each of the cubes, the remaining variables were kept constant, with 5 top and bottom layers being used to ensure a lower number would not effect the results, and 20% infill overlap was used as this is the default setting.

Each cube was printed with 2 gas ports, designed to fit 6 mm pneumatic tube fixtures. These inlets underwent several design modifications and were printed at 100% infill to ensure no leaking occurred from this feature and these inlets were



Figure 3.23: Subset of the printed small enclosures of constant internal volume and size, with varying wall thickness, perimeter number and infill percentage.

solid and sturdy; multiple failed attempts had previously been due to poor gas inlet formation or gas inlet fragility, whereby the inlet design allowed the inlet to be easily broken away, rendering the print unusable.

The same experimental procedure was executed to measure the gas-tightness of each cube. Each cube was separately flushed with Zero Grade argon ($> 99.999\%$), as the gas used in the final detectors would be an argon mixture, and the oxygen concentration of the gas composition exhausting from the cube was measured using the SGX SensorTech EC410 Oxygen Sensor [79]; placed within a purpose-made gas-tight box and calibrated using the same Zero Grade argon. It was previously known from experience with large area drift chambers (built for muon tomography

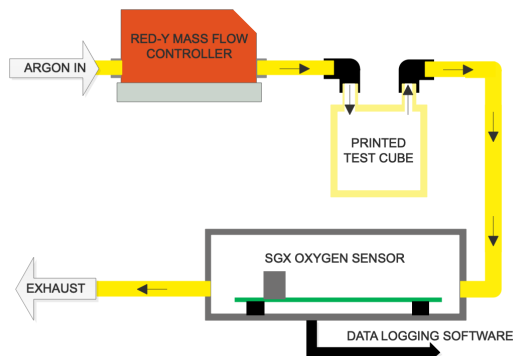


Figure 3.24: Experimental setup of the gas-tight enclosure tests.

applications) that an oxygen concentration < 300 ppm (parts per million) is required for consistent detector operation and so the minimum argon flow-rate required to hold each cube at an oxygen concentration below 300 ppm was used as a metric for gas-tightness. The argon flow-rate was controlled using a Red-y Smart Mass Flow Controller [custom model] from Vöegtlin [80], which could supply a flow between 0.0345 – 2 litres/min. The experi-

mental setup is shown in Figure 3.24. During the testing, it was observed that a high proportion of the cubes maintained well-below 300 ppm at this lowest flow-rate achievable by the mass flow controller and so the minimum oxygen concentration achieved at this flow-rate was also used as a metric.



Figure 3.25: View of a printed cube that has been printed using too much thermoplastic.

Initially, each cube was flushed with argon at 2 litres/min for several minutes, with the exhaust gas circumventing the oxygen sensor to reduce the time and argon required to purge the initial influx of oxygen from the oxygen sensor box, which has a much larger volume. The cube exhaust was then connected to the oxygen sensor box and the argon flow-rate reduced incrementally until the oxygen concentration remained just below 300 ppm over the course of many hours, or until the lowest flow-rate was achieved. A selection of the cubes were reprinted or re-tested to ensure reproducibility, with the values all remaining within a 20% of the values given in Table 3.2, which shows the lowest achievable results of the experiment, as these are the greatest potential gas-tightness possible from each of the settings.

The results show a clear trend that an increase in percentage infill and enclosure thickness result in a general increase in gas-tightness, with a clear exception; however, the increase from 3 walls to 4 does not necessarily increase the gas-tightness as expected, indicating a more complex relationship between the 3 varying parameters than previously thought. Inspecting the printed cubes revealed a possible reason; depositing too much thermoplastic can cause irregular wall formation, seen in Figure 3.25, which could result in errors in the print. From Table 3.2, it can be seen that the best possible combinations are: 2 walls, 3 mm thick and 75% infill; 3 walls, 4 mm thick and 50 – 75% infill; and 4 walls, 4 mm thick and 25% infill, i.e. thin walls, medium thickness and high infill; medium walls, high thickness and medium infill; or thick walls, high thickness and low infill. Maximising all the variables does not necessarily maximise gas-tightness. It should be noted that 3 walls, 4 mm thick and 100% infill has not been included as, although this is the most gas-tight, a similar

observation to Figure 3.25 occurred while looking at the print quality, and irregular printing can cause unpredictable issues.

Each re-tested cube reproduced the same level of gas-tightness with small variations in the actual reading, if the tests were performed under the exact same conditions. Some of the cubes were tested for extended periods of times, with measurements recorded up to 120 hours to ensure the level of oxygen would remain < 300 ppm when the final detectors operate constantly. Significant variations in the recorded measurements occurred throughout these longer tests, whereby the measured oxygen concentration would fluctuate by ± 15 ppm throughout the course of the day, with the lowest oxygen concentrations corresponding to the lowest ambient laboratory temperature. An investigation into the effect of ambient temperature on gas-tightness was also performed, whereby the oxygen concentrations of various cubes would be measured alongside the laboratory temperature, which was varied

Wall Number	Thickness mm	Percentage Infill, %			
		25	50	75	100
	2	0.095 ± 0.001 l/min			
2	3	0.055 ± 0.001 l/min	0.072 ± 0.001 l/min	105 ± 3 ppm	
	4	0.055 ± 0.001 l/min	250 ± 3 ppm	226 ± 3 ppm	
	2				
3	3	0.070 ± 0.001 l/min	200 ± 3 ppm	208 ± 3 ppm	289 ± 3 ppm
	4	0.046 ± 0.001 l/min	102 ± 3 ppm	90 ± 3 ppm	70 ± 3 ppm
	2				
4	3	0.050 ± 0.001 l/min	180 ± 3 ppm	161 ± 3 ppm	
	4	100 ± 3 ppm	210 ± 3 ppm	152 ± 3 ppm	

Table 3.2: A table of results for the minimal gas-flow required to maintain an atmosphere below 300 ppm argon, or the minimum oxygen concentration at the lowest flow rate of 0.0345 l/min.

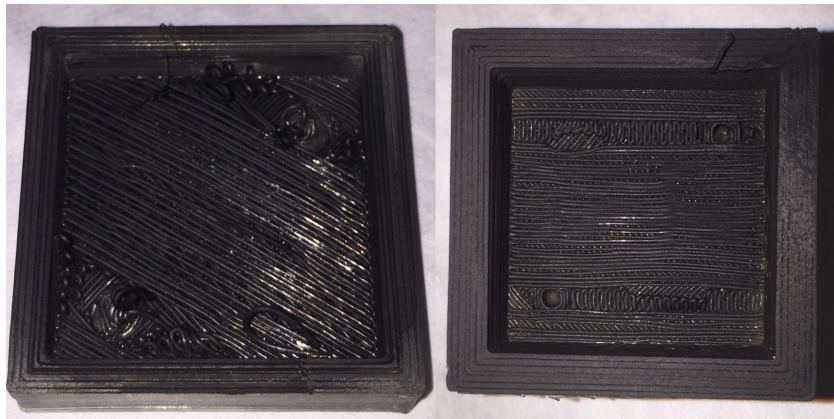


Figure 3.26: (*Left*) Poor ceiling formation due to unsupported print of gas inlets, highlighted in Figure 3.27. Both prints have been painted to aid visibility.

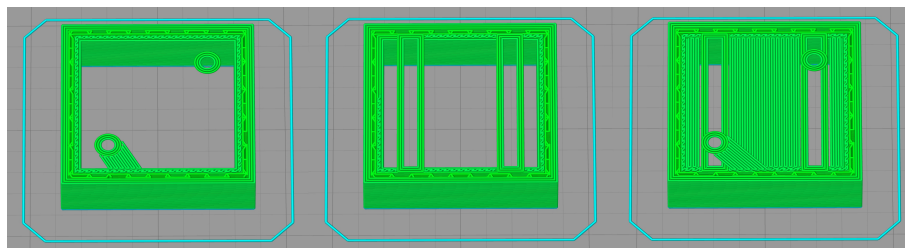


Figure 3.27: (*Left*) Print preview of the toolpath for the first cube design, highlighting the problem of the initial overhanging structures not being connected to any existing structures. (*Middle, Right*) Print previews of the toolpath for the second cube design, showing a design that forces 'bridge' structures to be printed first, allowing the first gas inlet layers to be supported.

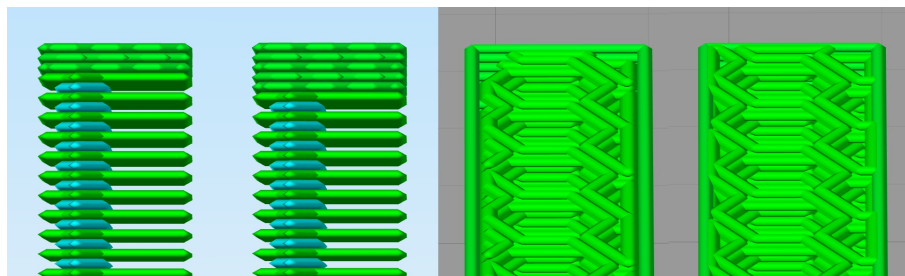


Figure 3.28: Previews of the extruder toolpath for: (*Far Left*) 3 complete enclosing, top layers; (*Middle Left*) 5 complete enclosing, top layers; (*Middle Right*) 0% overlap of infill and (singular) wall; and (*Far Right*) 75% overlap of infill and (singular) wall.

between 18 – 30°C.

Measurements from the cubes exhibited the same fluctuations with temperature, with the minimum oxygen concentration always occurring at the lowest temperature of 18°C and the highest concentration occurring at 30°C, increasing by approx 30 – 40 ppm of the initial concentration at 18°C. Unfortunately, due to the non-regular changes in ambient temperature, the specific relationship between ambient temperature and oxygen concentration could not be determined accurately, and so only the general trend can be reported on; an increase in ambient temperature results in an decrease in gas-tightness from the printed cubes. This does put some constraints on the possibilities of future detectors, such as operating 3D printed detectors underground laboratories where temperatures can reach upwards of 40°C.

As for the re-printed cubes, each cube was printed individually, instead of collectively as the first set were. 80% of the re-printed cubes performed equally well when tested, however, some significant differences were observed in some of the cubes, all with 3 mm enclosure thickness, with the largest difference occurring between cubes printed with 3 wall and 100% infill. After testing, these cubes were cut open to have the internal structures inspected for any inconsistencies between the prints, that could be the source of differences in gas-tightness.

The inspection showed varying print quality, but not in wall or base formation which were consistent between the prints. The significant differences occurred in the 'ceiling' formation, mainly due to some of the initial printed lines misprinting around the gas inlets and from further inspection of the gcode, the reason was clear, see Figure 3.26 and Figure 3.27 (*Left*), respectively. This effect was observed in the cubes of 4 mm wall thickness, however, the extra thickness of the ceiling meant that this initial poor formation did not affect the overall gas-tightness of the cube.

Initially, the gcode was edited to remove these initial structures and add in new lines of gcode to print support structures in the ceiling, however, this was a timely process required many toolpath commands to be calculated and replaced manually. A new design was then created to force the printing toolpath to print supports for these initial ceiling structures, as seen in Figure 3.27. This allowed for much better print quality and was used to retest a selection of the cubes, multiple times. The new design did not affect the maximum gas-tightness found from any of the different cube settings of the initial design but instead drastically reduced the variability in results between prints of the same print settings, ensuring that concordant results could be achieved with every print.

Now consistent prints could be created, the new design was used to test the other two print variables: number of top and bottom layers, and infill overlap. The differences caused by these parameters are shown in Figure 3.28. To test these settings, cubes of 4 mm thickness, 3 walls and 50% infill were used, as the previous results from this cube were of the best. To test the number of top and bottom layers, all settings were kept constant and 4 new cubes were printed with 1-4 top and bottom layers; 5 had already been tested but is included in the results. To test the effect of infill overlap, the same cube was used, with 5 top and bottom layers, and the infill overlaps used were 0%, 25%, 50%, 75%, and 99%, as 100% infill overlap is not possible. The results from the tests are shown in Table 3.3. It should be noted, the overlap experiments were performed at a higher laboratory temperature 32°C, and so the values shown are particularly high, however, the effect of the overlap can still be seen.

The results from varying top and bottom layers show an expected trend, that the gas-tightness of a cube increases as the number of complete top and bottom layers also increase. This print setting variable, with infill percentage second, has the most effect on gas-tightness, with 1 layer proving not gas-tight at all and increasing up until a plateau at higher values.

The results from varying infill overlaps did also show an increase in gas-tightness with overlap, however, at these higher infill overlaps (> 25%), the same defects as seen in Figure 3.25 occurs, where too much thermoplastic is forced into too small an area.

Layers	1	2	3	4	5
	Failure	0.042 ± 0.001 l/min	196 ± 3 ppm	104 ± 3 ppm	102 ± 3 ppm
Overlap	0%	25%	50%	75%	99%
	246 ± 3 ppm	144 ± 3 ppm	152 ± 3 ppm	129 ± 3 ppm	128 ± 3 ppm

Table 3.3: Results for the minimal gas-flow required to maintain an atmosphere below 300 ppm argon, or the minimum oxygen concentration at the lowest flow rate of 0.0345 l/min.



Figure 3.29: Picture of a 3D printed GD enclosure with vacuum flange attachment for vacuum seal test.

Vacuum Tests

From the results so far, it was determined that to maximise gas-tightness, while minimising thermoplastic usage and ensuring print reproducibility, the ideal print settings to use for enclosures are: 3 walls, 4 mm thickness, 50% infill, 4 top and bottom layer and 25% infill overlap. Throughout the previous experiments, it had been assumed that any 3D printed detector would require a constant flow of gas for correct operation, ensuring any contaminants are constantly removed. To determine whether a sealed enclosure is possible, the ideal print settings were used to create a small enclosure with a single inlet; a vacuum flange, as seen in Figure 3.30. This enclosure was connected to a vacuum pump via a pressure gauge, to measure the level of vacuum that could be achieved. Unfortunately, after many tested designs, each with a slightly varied vacuum flange to ensure a perfect seal, no measurable vacuum was achieved, confirming the previous assumption that any 3D printed GD would require a constant flow of gas to ensure correct, continued operation.

3.7.1 Wired Gas-Tight Enclosure

The final test in this series was to collect the designs, print settings and techniques discussed above and produce a final test cube that can print successfully, without error, hold a taut anode wire and still be gas-tight, as there were some initial concerns that the introduction of the anode wire would severely effect the gas-tightness of an enclosure.

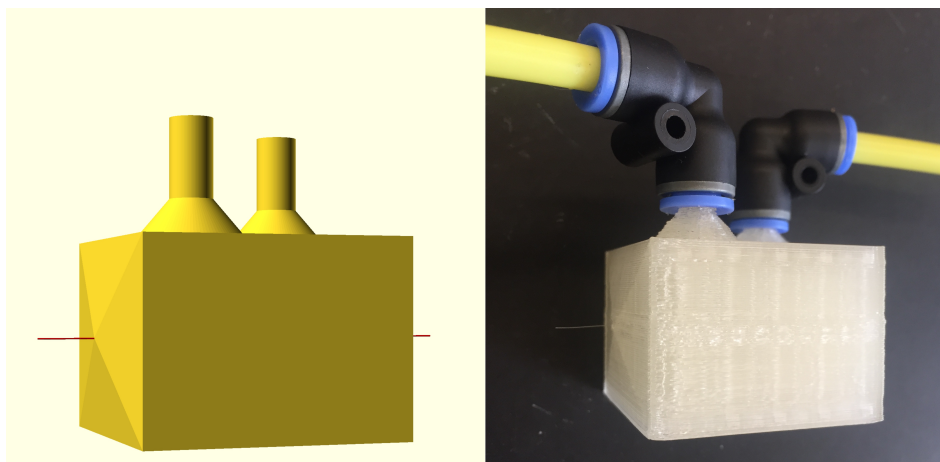


Figure 3.30: *(Left)* OpenSCAD model of the final gas-tight test cube, complete with extended ends to better grip the anode wire (added in red to better illustrate). *(Right)* Picture of the second printed gas-tight test cube, printed using the settings mentioned above, the anode wire can be seen in the central position where the extended end converges.

The design shown in Figure 3.18 *(left)* was printed using the "ideal" print settings, and the gcode edited to print 100% infill around the middle layers and pause half-way for the introduction of an anode wire. The final wired test cube was flushed with argon before reducing the flow rate to 0.0345 l/min and the oxygen level monitored, using the same procedure described at the beginning of this section. Six more identical wired cubes were printed and tested using the same methodology. The average result for the 7 cubes is 170.00 ± 5.18 ppm with a standard deviation of 24.04 ± 3.08 ppm.

3.8 Chapter Summary

Through experimentation with various commercially available thermoplastics, 3D printers, slicing software, enclosure geometries and print settings, a reliably printable, gas-tight enclosure, complete with taut anode wire has been successfully produced using the FDM process. PLA has continually proven to be the best thermoplastic available for the printing of GD enclosures with minimal warping, successful overhang formation (especially with horizontal ceilings), superior consistency

between prints and low-radioactivity in pigment-free PLA.

The Replicator 2X from Makerbot was deemed unfit as a 3D printer for the application of 3D printing GDs. High warping and extremely poor consistency between prints meant any investigations done using the Makerbot would be useless as differences caused by these factors would greatly outweigh those from the actual change in design and print settings. The small print volume greatly limited geometry development and the unaccommodating software restricted the exploration into the full scope of possibilities that come with additive manufacturing. The Gigabot, however, solved all these problems and also provided many desirable and useful properties and functions.

After extensive investigation into enclosure design, concerning mainly printability and reproducibility, the best designs came from hexagonal and triangular volumes, with the latter opening up possibilities to investigate whether increased functionality can come from new GD geometries, with the use of creative cathode structures to produce uniform electric fields, which will be discussed later in this thesis. The external geometry of these enclosures were also developed to sufficiently hold an anode wire at the correct tension, with minimal risk of the anode wires being pulled free, resulting in GD becoming useless.

Gas inlets were developed, both through design and print setting changes, to minimise loss of leakage from gas transfer from the pneumatic tubes to the enclosure while also minimising the risk of breakage, which was revealed as a significant issue and would render the prints, once again, useless.

Various print settings were investigated to maximise the gas-tightness of the printed enclosures while minimising the amount of thermoplastic used and avoiding poor print quality, due to the altered print settings effecting wall and ceiling formation. The enclosure design was altered slightly to improve consistency of ceiling formation between prints, limiting variability in gas-tightness across enclosures of the same design and print settings.

The results from this work are consolidated into a final product: a gas-tight, hollow volume enclosure which successfully holds a taut anode wire, and consists of gas inlets with high structural integrity; the design and print method of such resulting in consistent and reliable prints, removing all instances of initial print failure.

Chapter 4

Operational Detectors: The First 3D Printed Single-Wire Gaseous Detectors

Given the successful development of wired, gas-tight enclosures, as discussed in Chapter 3, the next stage of the detector development was to create a large scale version, with appropriate high voltage connectors, and investigate whether charged particles could be detected by a 3D printed gaseous detector (GD). In the first instances, the detectors contained only an anode wire as the source of the required electric field, while the design, fabrication and introduction of 3D printed cathode structures were still in development.

4.1 The First Single-Wire Gaseous Detectors

The techniques developed and enclosures designed, as discussed in Chapter 3, were used to print longer, tubular enclosures containing anode wires. This process involved the design and fabrication of longer and more structurally reinforced wire frames, able to hold the anode wires without bowing or twisting under the applied tension, which did initially present as a complication. When designing a new enclosure, the wire frame must always be printed first, to ensure the correct anode-wire height is achieved. As explained in Section 3.2, anode-wire placement is paramount to correct detector operation, and so the enclosure height is designed around the measured height of the printed wire frame.

4.1.1 Detector V1: Design and Data Collection

The first few attempts were printed using the hexagonal volume enclosure, with successful long tubular prints being accomplished, see Figure 4.1, scaling up the previous designs to 48 cm in length - the maximum length able to be printed on the Gigabot, while leaving room for the wire rig. Unfortunately, due to developments made while investigating possible 3D printable cathode structures (explained later in this chapter), this enclosure design was abandoned to the triangular design discussed in Subsection 3.4.1.

A major drawback that arose with these first tubes was at the exterior enclosure-anode boundary, where the anode wire was left quite brittle after being relieved of the applied tension, especially after the anode wire had been heated/cooled while attempting to solder the anode to additional component. This very often led to the anode wire breaking off at the exterior boundary, leaving the 3D printed tubes useless. Many avenues were explored to minimise the failure rate due to this issue with the easiest and most successful result simply coming from adding hot melt adhesive (HMA), a commonly used thermoplastic, to the exterior enclosure-anode boundaries before the wire was freed from the frame; removing all instances of anode wire breakage.

The new, triangular tubes were reduced in length to 145 mm, decreasing the print time and the amount of wire and plastic used per tube, which would be wasted if more critical issues arose. The internal geometry of the hollow volume consists of an equilateral triangle prism, with the triangle of side lengths of 28 mm. A new wire frame was printed such that the anode wire would sit centrally and equidistantly from the volume edges, rather than at half height. End caps were designed to fit

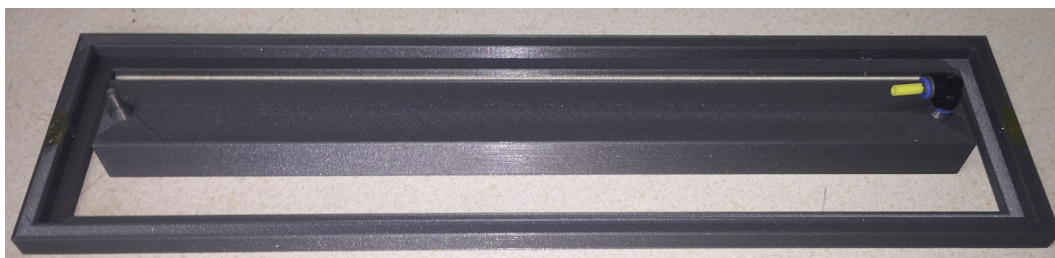


Figure 4.1: Picture of a long 3D printed tube complete with anode wire. The 3D printed wire frame is also shown around the drift tube.

around the ends of the tube, for housing of the bare anode wire, Safe High Voltage (SHV) connectors and any additional circuitry. These end caps were then printed, and the tube was fitted together, see Figure 4.2.

Initially, one end of the anode was connected to an SHV via a $1\text{ M}\Omega$ resistor, while the other end was connected straight to the other SHV connector. The tube was finished with a silver-coated copper screening compound; an aerosol spray to add protection against radio-frequency interference (RFI). A secondary purpose of the spray was to act, somewhat, as an external, grounded cathode to aid in creating the internal electric field, rather than having a single floating internal electrode. Both SHV connectors and the tube are connected via a relatively large gauge grounding wire to ensure a common ground runs along the entire detector, in case the conductivity of the RF shielding spray did not continue from one end to the other.

In the first attempt to detect charged particles with this tube, the resistor-free end of the detector was connected to a Tennelec TC 174 Low Noise Preamp, the output of which was passed to a Tennelec TC 243 Amplifier to add further amplification and shaping to the signals, which were then set to be observed using a Teledyne LeCroy WaveRunner 620Zi oscilloscope. A CAEN V6521P HV Power Supply Module was used to provide a low current, high voltage to the anode wire via the preamp.

P5 gas (5% methane, 95% argon) was used as the drift gas and the SensorTech

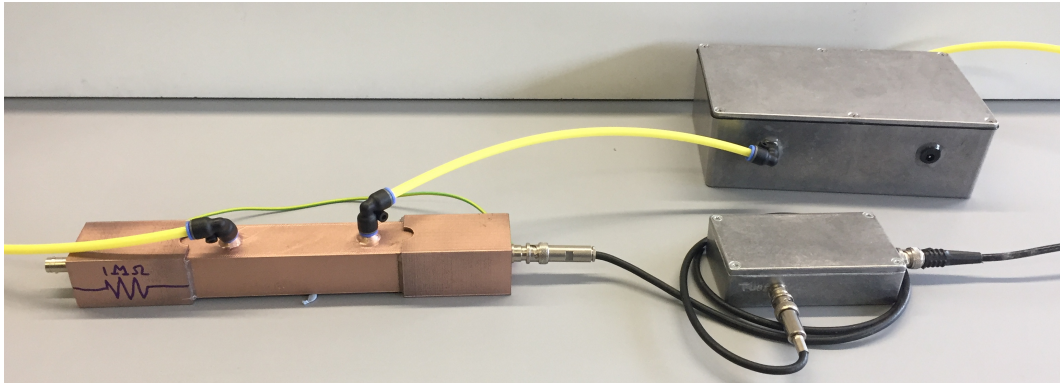


Figure 4.2: Picture of a long, tubular 3D printed SWGD, wire triangular interior structure and complete with end caps to connect to the anode wire. The small metal box contains the signal decoupling circuit shown in Figure 4.3 and the large metal box is an airtight housing for the SensorTech EC410 Oxygen Sensor.

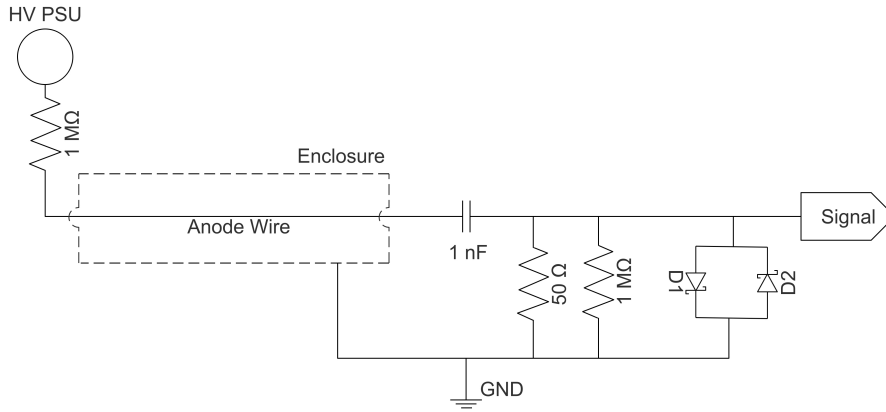


Figure 4.3: Circuit diagram of signal decoupling circuit. The $50\ \Omega$ resistor was included to better match the impedance of the signal output system. Components D1 and D2 are Schottky Diodes included as a precaution, to limit the signal amplitude and protect the oscilloscope electronics against any breakdown that could occur while exploring the bias voltage range.

EC410 Oxygen Sensor was used to monitor oxygen levels, which were maintained below 250 ppm. The temperature was recorded throughout the experiment, which remained at $297 \pm 2\ \text{K}$. Unfortunately, the TC 174 Preamp has a maximum voltage rating of 2 kV due to the ratings of components used and, even at this maximum voltage, no signals were observed from the detector.

The next stage involved supplying a bias voltage straight to the tube, via the $1\ \text{M}\Omega$ resistor and to capacitively decouple the signal from the high voltage at the other end of the tube. A rudimentary circuit was used initially while more advanced circuits were developed through simulations using LTspice, an electronic circuit simulator created by Linear Technology (now part of Analog Devices) [81].

The primary circuit used in this first instance is shown in Figure 4.3, however, it should be noted that all components except the initial $1\ \text{M}\Omega$ resistor were located in a metal grounded box connected to the tube via a SHV cable, see Figure 4.2. Initially, due to lack of access to a preamp at the time of testing, the raw output was measured with any signal above background noise being recorded. P5 was, again, used as the drift gas and the oxygen level recorded, kept below 250 ppm. The temperature was also recorded and remained at $299.0 \pm 1.5\ \text{K}$.

Cosmic ray muons (CRMs) were used as a source of high energy charged particles and at least 3000 events were recorded for each of the applied bias voltages. The

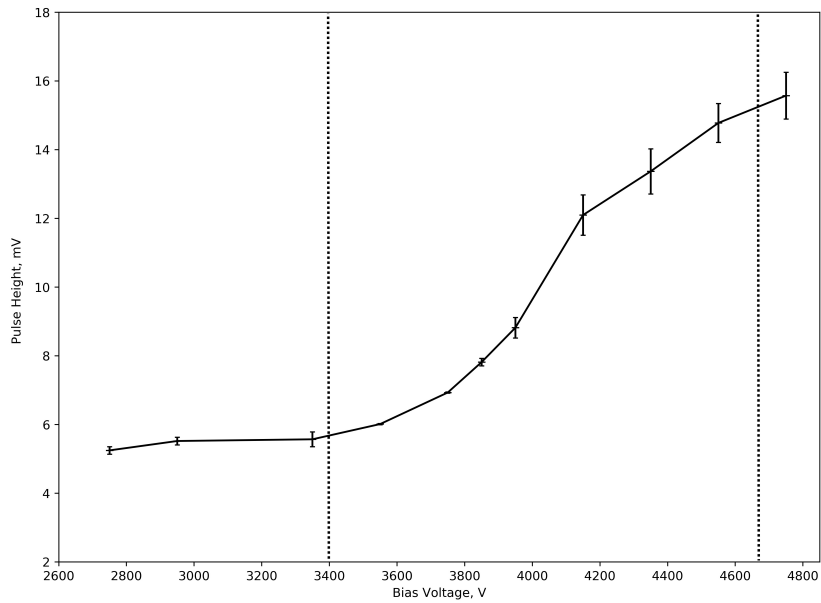


Figure 4.4: Graph of average pulse height against applied bias voltage for Detector V1. All data was taken at a constant threshold. Two distinct regions of operation have been indicated, with a possible 3rd region highlighted from ~ 4500 V onwards. The maximum electric field, in V/cm, can be found by multiplying the bias voltages by 39.33 cm^{-1} .

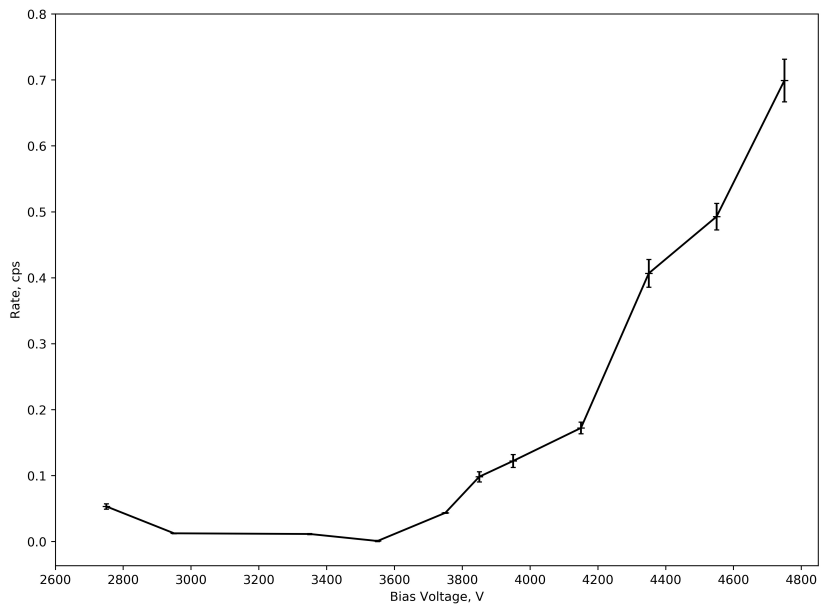


Figure 4.5: Graph of average event rate against applied bias voltage for Detector V1, in counts per second (cps). The maximum electric field, in V/cm, can be found by multiplying the bias voltages by 39.33 cm^{-1} .

voltages used ranged between 2750 V and 4750 V, in 200 V intervals; the range was dictated by the minimum bias required to record any signal and the bias at which electrical breakdown occurred in the signal decoupling circuit box, despite efforts to avoid this i.e. coating circuit boards in protective lacquer.

4.1.2 Detector V1: Results

The results for the average pulse height and rate for each bias voltage are shown in Figure 4.4 and Figure 4.5, respectively. By comparing the pulse height results to correct operations, seen in Figure 4.4 and Figure 2.1, respectively, two operational regions can be differentiated. Without more data, these two distinct regions could be identified one of the following three possible pairs:

- Scenario 1: Noise (no signals) and Recombination Region;
- Scenario 2: Ion Chamber Region and Proportional Region; or
- Scenario 3: Geiger-Müller Region and Continuous Discharge.

By using both the explanation for each of the regions, discussed in Subsection 2.1.1, and the rates shown in Figure 4.5, the pulse height data could show Scenario 1, whereby the increasing bias voltage results in an increasing number of events as less primary electron-ion pairs recombine, however, this is very unlikely.

Scenario 2 is the most likely explanation given that the bias voltages used are significantly high for most GDs; the fact that no preamp could be used at this time, thus any measured signals must be significantly large to be measured; and the breakdown voltage (V_B) of argon is relatively low. At the temperature and pressure of operation, 1 atm and 300°C, V_B^{Ar} is calculated to be ~ 700 V/mm [82]. With the minimum anode wire-enclosure distance at 8.08 mm, and neglecting contributions from the electrically insulating PLA completely, the minimum required voltage for breakdown, and continuous discharge, is ~ 5600 V; making Scenario 3 unlikely.

4.2 The Upgraded SWGD

The first 3D printed GD had been fabricated and some initial operation attempted. Many candidate signals were recorded, yielding somewhat familiar characterisation plots, however, no reasonable conclusions can yet be made with confidence. The

need for detector upgrades and further development were required for more reliable data acquisition and, consequently, conclusions to be made.

4.2.1 Detector V1.1: Design and Data Collection

The most necessary upgrades required regard the RFI protection and signal decoupling circuit. Plastic is notoriously difficult to paint and the silver-coated copper screening compound used for the RFI protection wore off easily over a short time due to handling; see Figure 4.6 compared to Figure 4.2. To fix this matter, a simple solution came from the application of copper tape to the exterior of the detector enclosure and the end caps; a solution of greater cost, but also permanence.

The solution for the decoupling circuit was simply to redesign and rebuild the circuit. The current circuit, located in separate metal box and connected to the detector via a SHV cable, was far from ideal; even while using a short SHV cable, it was suspected that significant attenuation of any signal was occurring before being decoupled from the HV line, and then further attenuation from this box to the amplifier or DAQ. To combat this issue of decoupling the signal from the HV, a circuit was designed to fit inside a detector end cap which takes a HV input and outputs a signal decoupled from the HV. This circuit contains a series of low pass filters, to reduce high frequency noise in the HV line, and is then connected directly to the anode wire. The anode wire is then decoupled from the HV via a capacitor and the signal is left as an output, via a much larger load resistor than previously used, which is connected to ground. The circuit and circuit diagram are shown in Figure 4.7.

Other minor issues resorted from the lack of access to a preamp and reliance on the expensive CAEN V6521P HV power supply board. With the aim of this thesis to create low-cost solutions to instrumentation, the initial goal set was to have 2 small, modular circuits, in addition to the signal decoupling circuit, that could be housed within the end caps of the detector. The first circuit would convert a low-voltage input into a high voltage supply for the electrodes, and the second circuit would amplify the decoupled signal to provide a measurable output.

Building a preamp from scratch appeared to be a cost-effective solution, however, another solution was devised after preliminary Garfield++ simulations [83] of the expected detector signal revealed the time between the rise and 60% fall of the ion peak, to remove the long ion tail, was of the order of 100 ns. This signal length

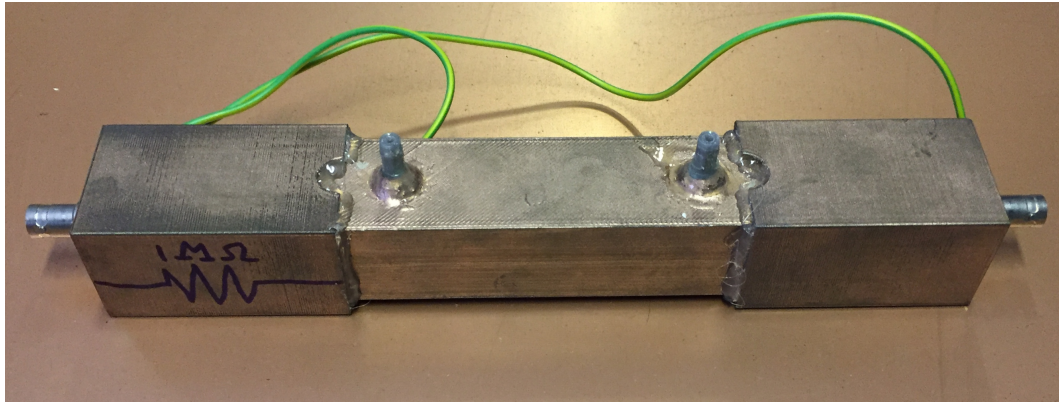


Figure 4.6: Picture of the first detector v1.0, showing the severity of the silver/copper RF protection has worn off over time, due to poor initial adhesion to the PLA.

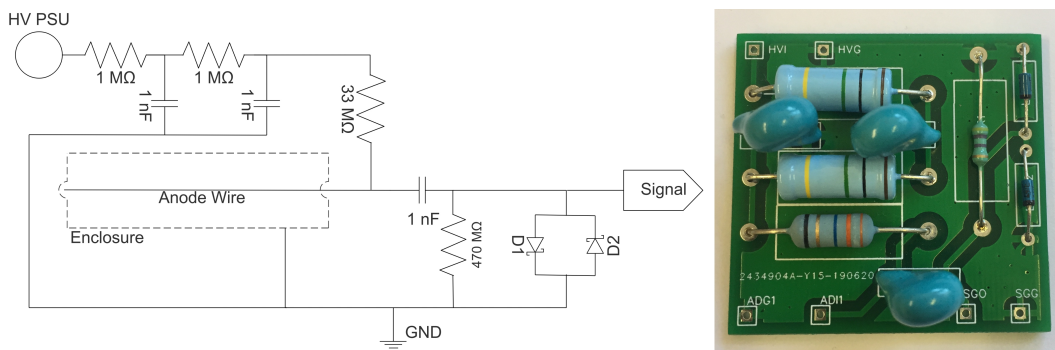


Figure 4.7: (Left) Circuit diagram of the newly developed signal decoupling circuit. Again, D1 and D2 are Schottky Diodes included as a precaution to protect against any large current or sparking. (Right) Picture of the manufactured PCB complete with all components soldered in place.



Figure 4.8: (Left) New decoupling circuit fitting into new end caps. (Middle) Tube end, with SHV connectors for HV supply (bottom right) and signal (top left). A SHV connector was required for the signal out to be passed to the preamp. (Right) Picture of the upgraded detector, V1.1.

corresponds to RF, opening the possibility of using cheap, low-voltage, wide-band RF amplifier boards. Many such RF amplifier boards were tested with generated signals and showed promising results, especially the RF amplifiers by HiLetgo, which require 6 – 12 V and offer low-noise gain ≤ 30 dB (1000 times) for $\sim 2\%$ the cost of application specific, charge sensitive preamplifiers.

Solutions for the low-cost, low-voltage input, high-voltage output module were found to be already on the market, removing the need to develop a circuit from scratch. An example of such is the EMCO AG30P-12 DC-DC Converter; a small (6.8 mm x 11.5 mm x 29.0 mm) module which converts 12 V up to 3 kV using a control voltage.

The use of the RF amplifier and HV modules in the printed detector would mean each printed detector could, potentially, be fully powered via a 12 V power supply, producing the applied bias voltage and primary signal amplification.

While the Tennelec preamp and CAEN V6521P were available, these upgrades were not necessarily vital for the project's development at this time. Consequently, further investigation into the viability of these modules was put on hold indefinitely, yet still remain an exciting area for future development.

The upgraded detector, Detector V1.1, can be seen in Figure 4.8. With the changes made, the next stage was to test whether these upgrades improved operation. A similar experimental setup to the initial characterisation was re-created. The detector output was connected to a Tennelec TC 174 Low Noise Preamp, the output of which was, again, passed to a Tennelec TC 243 Amplifier for further amplification and shaping of the signals. The gain was adjusted accordingly for each of the bias voltages but the shaping was constant throughout using a bipolar shaper, with an 8 μ s peaking time, selected as an output, which was passed to a LeCroy WaveRunner 6100 oscilloscope to observe the signals. The CAEN V6521P HV Power Supply Module was used once again to provide a low current, high voltage to the anode wire, but this time connected straight to the detector via the low pass filters, instead of via the preamp. The detector was also isolated from any vibrations in the near environment to ensure no unnecessary noise was induced in the taut anode wire.

A new gas mixture was used as a drift gas, consisting of 2.5% methane, 5% carbon dioxide and 92.5% argon. The main reason for this change was due to drift gas availability, however, this new mixture offered many benefits. The new gas mixture, when compared to P5, has a lower radiation length, yielding more primary and

total ionisations/cm and larger signals; increases ion mobility and drift velocity; and results in a drift velocity which is, potentially, less variable over the large, possible range of applied bias voltages used while characterising the detector [84][85][86]. The SensorTech EC410 Oxygen Sensor was recalibrated and used once again to monitor oxygen levels, which were maintained between 160 – 190 ppm. The temperature was recorded throughout the experiment, which remained at 300.6 ± 2.4 K.

Initially, the detector was operated between two blocks of plastic scintillator, each connected to a Silicon PhotoMultiplier (SiPM), to act as a muon telescope. A coincidence trigger was set up between all 3 detectors to ensure any signals from the SWGD were indeed from CRMs propagating through the drift gas. 3-fold coincidences were successfully observed at a range of applied bias voltages, arbitrarily chosen, however, the initial rates of detection from this setup, due to the small area of plastic scintillator blocks, were ~ 1 cps (counts per second) and meant acquiring a large dataset would require a significant amount of time. As this preliminary experiment had proven the 3D printed SWGD could detect charged particles, another experiment was setup without the muon telescope, and with a radioactive source, to increase the rate of detection.

A 205 Bq, strontium-90 source was used to subject the detector to a constant flux of beta particles, and increase the rate of detection above that possible before with just CRMs. This strontium-90 source should provide β -particles at a flux of $\sim 15\text{s}^{-1}$ (found experimentally), after absorption due to the thickness of thermo-plastic; these β -particles will have a range of energies < 0.55 MeV; the energy of the emitted β -particle. The bias voltages used ranged between 800 V and 2600 V, in 100 V intervals; the range was dictated by the minimum bias required to record any signal and the maximum voltage the signal decoupling circuit could handle without breakdown. The characterisation was terminated at this bias to ensure the preamp was protected against sparking in the decoupling circuit.

Each trigger saved the signal waveform at a reduced sample rate of 5 MS/s. More than 1000 events per bias voltage recorded, with a much greater number of events recorded for most bias voltages, however, at the lowest bias voltages, which resulted in very low rates, only ~ 1000 events were recorded.

4.2.2 Python: Selection Algorithm

As the operational regions are to be determined, and the signal heights from the new detector are unknown, the appropriate threshold for each applied bias voltage cannot be determined. Instead, a constant low, pre-amplifier (but post-preamplifier) gain, threshold of 8 mV was used throughout, i.e. this would detect all signals of 8 mV, or higher, from the Tennelec TC 174 Preamp. As signals from the preamp were then subjected to shaping and further amplification, which was often higher for lower bias voltages to ensure smaller amplitude signals were detected, the actual threshold used was adjusted proportionally to the gain applied with the Tennelec TC 243 Amplifier.

Using this setup, all signals should be detected, across all operational regions. An unfortunate consequence of this low threshold meant an unknown proportion of the saved waveforms could have triggered due to particularly large levels of noise; the average noise level throughout testing was observed to vary significantly over time, mainly due to sporadic noise on the ground line of laboratory's mains electricity. The source of this noise is unknown and was difficult to account for.

With a large dataset of $\sim 10^5$ events taken for the detector, removal of these instances would require automation via a data processing program. Rigorous selection criteria was required to determine signals from noise, especially during periods of significant noise. The data processing was also required due to the limited range of the Tennelec TC 243 Amplifier output, which saturates at 6 V; high enough gains were required to ensure any low-amplitude signals weren't missed in the data acquisition, however, this did leave the high-amplitude signals restricted to this maximum value, discussed in more detail later in this subsection. As a constant signal shaper was used throughout, a curve-fitting model could be used to determine the actual signal maximum despite the cut-off.

Discrimination

A Python program was written to analyse each of the waveforms, whereby the first stage of the program was to scrutinise the recorded signals against a series of selection criteria to determine whether or not the waveform is a viable, true signal caused by a charged particle propagating through the detector, or a false detection caused by varying noise levels, most likely from the sensitive amplifiers and anode wire.

To create the criteria, a random subset of waveforms was taken from the whole dataset, i.e. 500 waveforms from each bias voltage. These waveforms were individually analysed and divided into 2 groups: those which were definitely signals, and those which were not. The Python script was then written based on characteristic parameters of true signals, not exhibited by false-triggers. This program was applied to the subset of data, which attempted to sort the data back into these groups successfully; the criteria parameters were adjusted and fine tuned until this was successful. The final program considered the following 3 criteria:

- Signal Shape - the signal shape must match the characteristic, bipolar output of the Tennelec TC 243 Amplifier;
- Signal-to-Noise Ratio - the signal must have an amplitude 20% above the noise level of the waveform;
- Singular Signal - the saved waveform, which has a timebase much greater than the signal time, cannot contain any other candidate signals after the triggered signal.

After a long iterative process, the program could correctly analyse and sort the saved waveforms into the correct groups, with a 100% success rate at identifying non-signals; any waveforms that failed the selection criteria were removed from further analysis. A $> 99.9\%$ success rate at identifying signals was achieved. While a 100% success rate of identifying signals is ideal, a small proportional of the saved waveforms did contain multiple signals but were, unfortunately, removed.

The program was tested on subsequent subsets of data to ensure the criteria had not been created to display sample bias. If the program was unsuccessful, new subsets were used and the parameters retuned until the program was successful with all subsets. Figure 4.9 and Figure 4.10 shows waveforms with similar but low, maximum amplitudes to illustrate the selection of signals close to the noise limit, where correct categorisation is the most difficult and the most critical; disregarding all low amplitude signals will skew the final rate measurements, with the low amplitude signals more prevalent in the operational regions at lower bias voltages.

The waveform in Figure 4.9 has been categorised as “Not Signal” due to the secondary peak at $\sim 95 \mu\text{s}$. Considering the initial, almost constant trigger rate, and pulse height distribution, (pre-selection criteria), the probability of two signals, with such low amplitudes, occurring within $50 \mu\text{s}$ is significantly low enough to

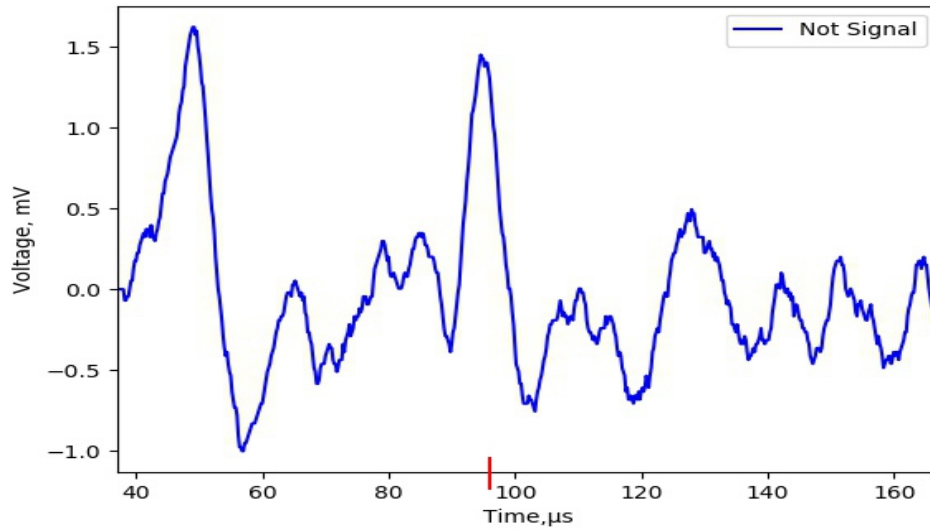


Figure 4.9: A waveform that was categorised as "Not Signal" due to peak amplitude being on 12% greater than that of the secondary peak at $\sim 95 \mu\text{s}$ (marked red). The amplitudes of the data have been adjusted by the final amplifier gain.

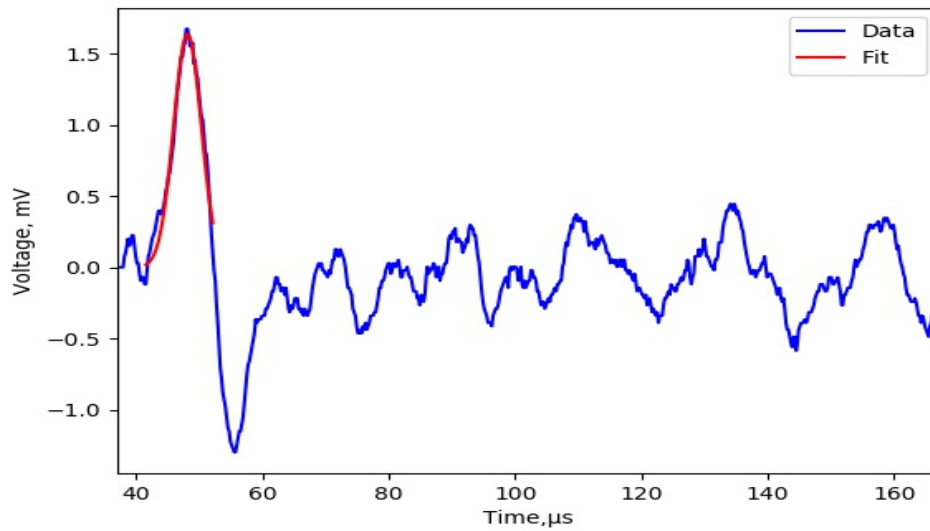


Figure 4.10: A waveform with initial similarities to that seen in Figure 4.9. This waveform was categorised as a signal as the peak amplitude is 276% greater than the maximum recorded noise level in the remaining waveform. A curve is fitted and overlaid over the original data; the process of which is explained later in this subsection.

determine the source of the second peak to be high noise levels. Given the first peak has a maximum amplitude only 12% greater than the maximum amplitude of the secondary peak, this waveform was rejected as too close to the noise level. This signal could be a legitimate particle detection, however, as this cannot be certain given the criteria, it is best to reject the waveform. Compared to Figure 4.9, Figure 4.10 shows a similar waveform, with a low amplitude, bipolar signal expected from the shaper. This waveform, however, was categorised as a signal as this maximum amplitude is 276% higher than the maximum noise level recorded in the rest of the waveform.

Curve Fitting

The second stage of the Python program was to fit curves to the peaks in all waveforms that successfully passed the selection criteria. This was required as the larger signals were saturated by the limited amplifier output. As mentioned, the Tennelec TC 243 Amplifier contains a shaping circuit to produce bipolar signals. These signals either didn't saturate ($< 6\text{ V}$), saturated the positive component of the bipolar

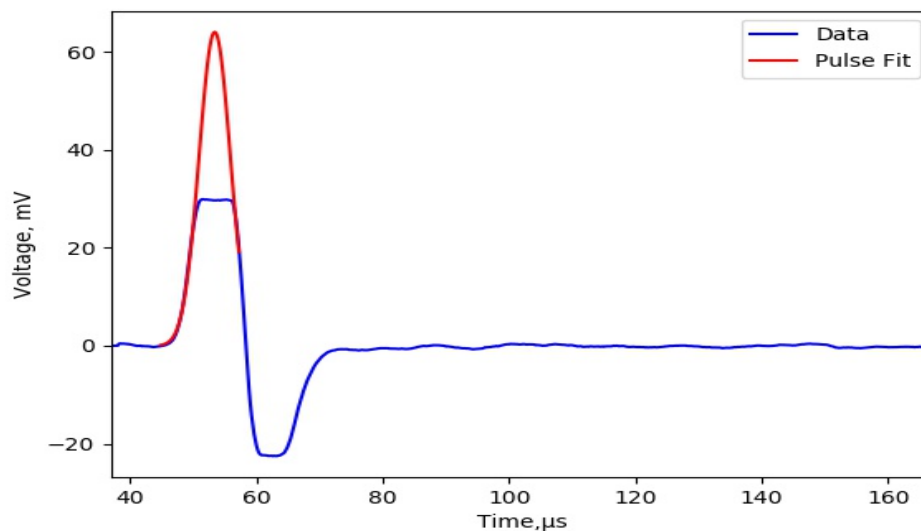


Figure 4.11: Example of a recorded waveform with the saturated signal amplitude, capped by the maximum amplifier output (rescaled for the amplifier gain). A fitted curve has been overlaid over the original data. The fitted curve maximum was used as the signal height for any further analysis of the dataset.

signal, or saturated both the positive and negative components.

Fitting a bipolar shape to the unsaturated and positive-saturated signals was consistent and successful, however, due to insufficient, correct data beyond saturation, fitting a curve to signals with both positive- and negative-saturated components often resulted in poor fits. Instead, the negative component of the signals were disregarded completely during the fitting and a gaussian curve fit was used on the positive component of the signals. This curve fitting was applied to all signal waveforms, including unsaturated waveforms, to ensure the data was treated equally.

The result of the curve fitting can be seen in Figure 4.11. The initial signal would have yielded a maximum amplitude of 30 mV while, after the curve fit, the maximum amplitude is more than double at 64 mV. A fitted curve can also be seen in Figure 4.10 for a signal which has not been saturated.

4.2.3 Detector V1.1: Results

Now that the data has been collected, with the waveforms discriminated and peaks fitted, the final data was used to investigate whether the 3D printed detector operates properly, given the discussion in Section 2.1. As before, the pulse heights have been plotted against bias voltage, as seen in Figure 4.12. In this case, as both a strontium-90 source and CRMs have been used as a source of charged particles, only the largest 10% of pulse heights have been used in this data to ensure only CRMs have been taken into account, rather than a mix of the two sources; this was found experimentally.

By comparing the results of Figure 4.12 to Figure 2.1 (expected results), and given no signals were observed at a bias below 800 V (with the preamp used), the initial sharp increase in pulse heights observed 800 – 1100 V is characteristic of the recombination region. Further increase in bias voltage shows a reduction in this increase and, given the errors, could indicate a move towards a plateau; characteristic of the ion chamber region. An unexpected decrease is observed while operating at 1800 – 2200 V, however, the errors on these measurements do not indicate this is significant.

The above description of the results gives further evidence that the data in Figure 4.4 shows Scenario 2 - the far end of the ion chamber region and the proportional region. This would mean that this first 3D printed SWGD has an extensive voltage plateau up to ~ 2 kV in range; Iarocci tubes tend to also show these large voltage

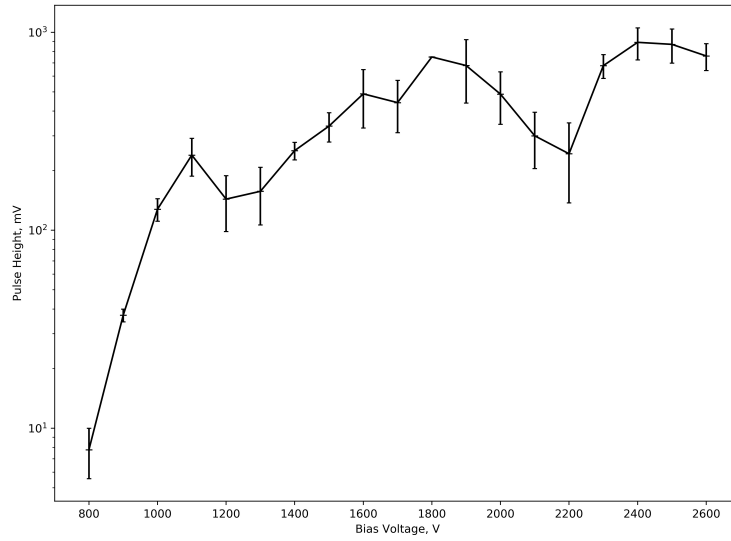


Figure 4.12: Graph of maximum measured pulse heights plotted against applied bias voltage for Detector V1.1. As before, the maximum electric field, in V/cm, can be found by multiplying the bias voltages by 39.33 cm^{-1} .

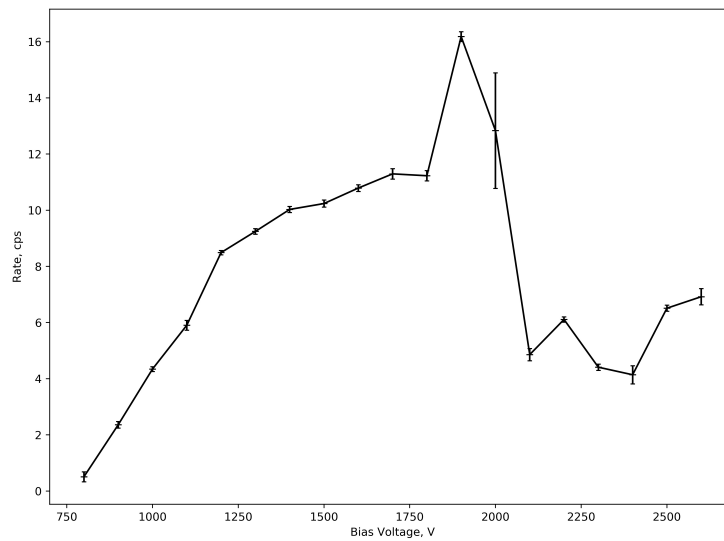


Figure 4.13: Graph of average event rate plotted against applied bias voltage, complete with standard error, for Detector V1.1. Unpredictable behaviour is observed after 1800 V bias. As before, the maximum electric field, in V/cm, can be found by multiplying the bias voltages by 39.33 cm^{-1} .

plateaus (~ 700 V), due to the resistive internal cathode and, as this 3D printed SWGD has a very resistive plastic interior, this large voltage plateau is expected.

The next analysis of detector operation takes into account the detection rate vs. bias voltage, shown in Figure 4.13. Again, given the operation regimes and the corresponding dead-times, the rate graph should increase with bias voltage in the recombination region, as more of the original electron-ion pairs are successfully detected, before plateauing out in the ion chamber region, as all the electron-ion pairs are detected. This plateau should last throughout until the limited proportionality region, whereafter shielding from positive ions starts to become significant, increasing dead-time and reducing rate.

The results shown in Figure 4.13 do initially show the expected rate increase and, by comparing the pulse heights in Figure 4.12, the plateau in rate begins at the corresponding ion chamber region. However, after 1800 V, the rate begins to vary in an unpredictable fashion, increasing at 1900 V before dropping to a rate approximately half that of the initial plateau, and does coincide with the drop in pulse heights observed over this range. A large error is expressed at 2000 V, indicates large variability at this bias voltage. It should be noted at this point, that the bias voltages 800 – 1800 V and 1900 – 2600 V were taken 18 hours apart, with the detector bias voltage was simply increased by 100 V between experiments before being reduced to 0 V overnight and then increased, slowly, to 1900 V to begin recording data again, which has clearly had a significant effect.

Detector Stability

To further investigate the observed rates, the change in rate over operational runtime for each bias voltage were extracted from the data. The data from each bias voltage was divided and the rates over each time segment were calculated and plotted in Figure 4.14.

The expected results, if normal operation had occurred, would show relatively constant rates over time for each of the bias voltages, although different bias voltage would not necessarily have the same rates. This constant rate is observed for the majority of the bias voltages, especially after the first few minutes of operation, with the most abrupt changes in rate observed over the initial operation, especially at 2000 V and 2600 V. From experience with the detectors, this is likely be due to data acquisition occurring too soon after increasing the bias voltage, as some time

is required for the detector to settle.

While the rate for most bias voltages remain relatively constant, with some variation over time, e.g. 2100 V, some bias voltages exhibit a significant change over the operational time. 2400 V, for example, shows an almost constant increase in rate over time, although without further data, it is uncertain whether this is a characteristic fluctuation of operation at this bias using the detector. The rates recorded over the runtime at 800 V do, however, show a $\sim 100\%$ reduction in the first ~ 500 s, which does not recover.

Given the shape of Figure 4.13 and the rate stabilities, the best explanation for the observed rates comes from the absence of an internal cathode. The cathode, as well as creating and shaping the electric field, is required to neutralise the positive ions that have drifted towards the enclosure walls, away from the anode. Without this cathode, a reduced rate of ion neutralisation would occur, causing ions to accumulate and create an increasing positive space charge until an equilibrium is reached. This would result in an a reduction in overall electric field and, if this reduction in electric field is sufficient enough, a reduction in rate could be seen, (as well as a possible reduction in pulse height over time, discussed later), with this effect occurring quicker at higher voltages as the rate increases and produces more positive ions, faster.

This effect could explain the changes in rate observed at 800 V, which shows a significant reduction in rate to almost 0 cps over the operational time. This positive space charge would then remain as the bias voltage is increased up to 1800 V for the experiments ran that day, and resulting in an overall reduction in electric field for each of the bias voltages tested, i.e. the gradient of the initial increase in rate, seen in Figure 4.13, would be much greater.

As the detector was then left at zero bias for an extended period of time, the positive ions could then neutralise in the absence of the electric field. After the bias was reapplied, a significant increase in rate occurred during operation at 1900 V (disregarding the initial increase in 2000 V), before decreasing again as the positive space charge increases to a higher degree at the greater bias voltages.

To find further evidence to support this theory, a similar investigation into pulse heights was performed, whereby the change in pulse heights over time were extracted from the data. If a significant reduction in the electric field has occurred, a similar decrease in pulse heights should also be observed, but only in operational regions of increasing pulse height with bias voltage, i.e. the recombination region

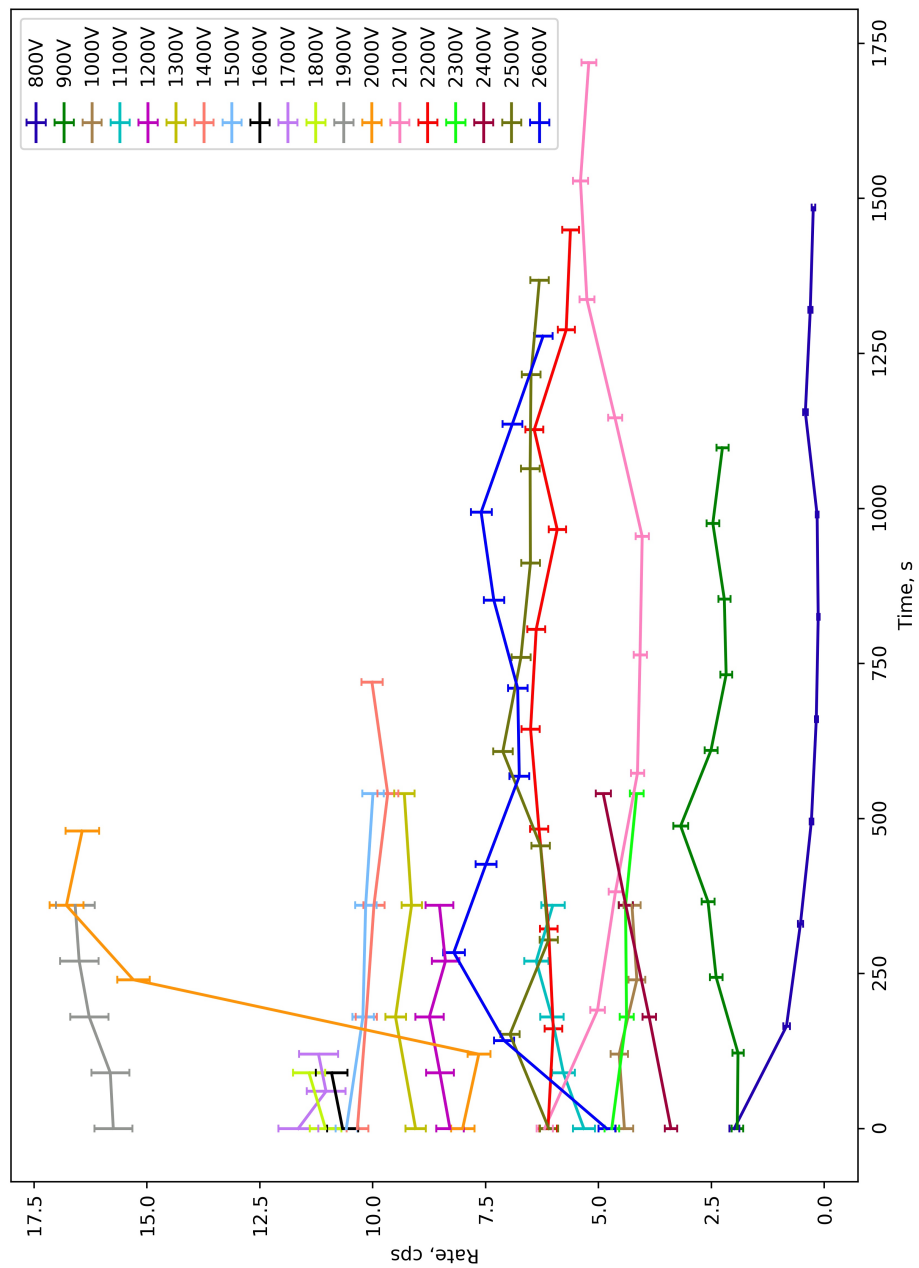
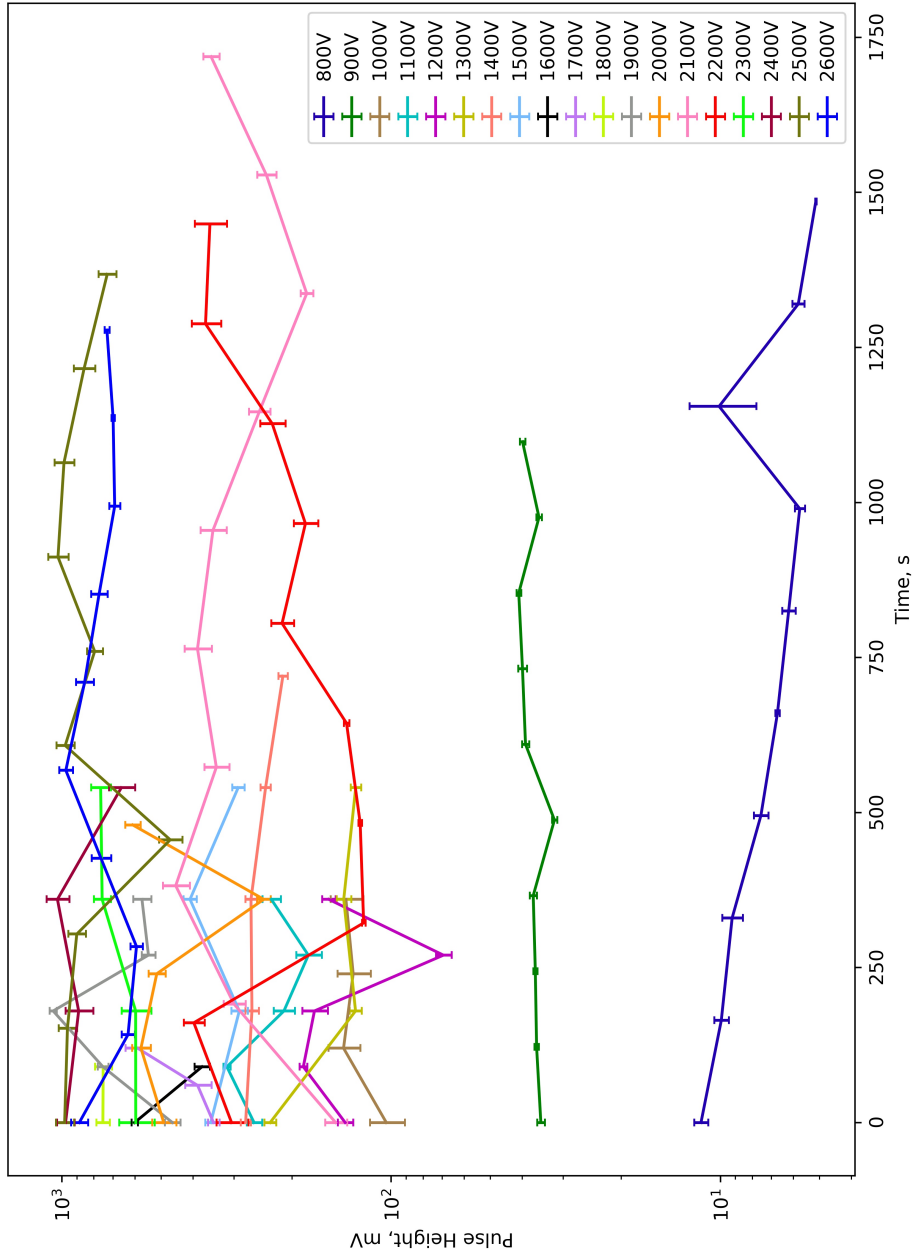


Figure 4.14: Graph showing the change in average event rate over time of operation for Detector V1.1. As before, the maximum electric field, in V/cm, can be found by multiplying the bias voltages by 39.33 cm^{-1} .



and proportional regions, or if the effect is significant enough to reduce the effective bias voltage from one operational region to another. The changes in pulse height over time for each of the tested bias voltages can be seen in Figure 4.15. Unfortunately, only 800 V shows a constant decrease over time, which does correlate with the decrease in rate seen in Figure 4.14, but this phenomenon is not shared by the other bias voltages, which do show significant fluctuations in the pulse height over time.

These large fluctuations in pulse height are, again, most likely caused by variations in effective bias voltage within the detector caused by space charge build-up. More evidence that an internal cathode is required.

4.3 Chapter Summary

A technique to produce the world's first 3D printed SWGD has been developed, with a functional detector produced. The initial tests, while inconclusive, did reveal the requirement for further development and led to the upgraded detector, V1.1. These upgrades led to the successful detection of charged particles while operating over a range of bias voltages and a large dataset was acquired. An algorithm has been created, in Python, to analyse the large dataset; capable of discriminating between genuine signals from charge particles and noise, especially at low amplitudes; and applying curve fits to signal waveforms as a means of measuring the signal pulse heights, compensating for the saturated waveforms produced through the combination of initially large signals and the 6 V maximum output of the amplifier used.

The pulse heights and rates, as a function of applied bias voltage, were calculated and plotted in Figure 4.12 and Figure 4.13, respectively. While the pulse height data in Figure 4.12 reflects the recombination and ion chamber regions, seen in Figure 2.1 the rate data exhibits behaviour which could not be explained.

The time dependence on both the pulse heights and rates were investigated in an attempt to further understand the unexpected changes in rate at higher bias voltages. Unfortunately, no significant changes could explain these peculiar rates, with the exception of the changes seen whilst operating at 800 V.

An explanation could still lie within the fact that the dataset was taken over days, as the separation occurs distinctly as the point at which the rate data begins to deviate from the expected. The positive space charge could have built up whilst

operating at 800 V and extends through to 1800 V, decreasing the effective bias throughout. Unfortunately, no further explanation can be given beyond this without supporting evidence.

While attempting to retake data with Detector V1.1 in a continuous run was a potential option, despite the lengthy experimental time required, the developments made this far were to ensure a 3D printed particle detector is possible and particle detection could be achieved. As aforementioned, a possible solution to the observed operational issues, and a noticeable element missing from the current design, is an internal cathode. To continue with the development of the 3D printed GD, focus should move into the design, fabrication and integration of a cathode into the current work already completed.

Chapter 5

Operational Detectors: Cathode Development and Cylindrical Geometries

The upgrades added to create Detector V1.1 successfully allowed the detection of charged particles, however, it has been proven that constant, reliable operation isn't achievable with the current design. The next stage, to move past this initial proof-of-concept, was to develop an internal cathode; the most noticeable feature missing from the current design. The introduction of an internal cathode should improve detector operation by neutralising positive ions and removing any possibility of positive space charge build-up affecting the applied electric field.

5.1 Available Techniques for Cathode Development

At the time of this particular topic of research, few options of introducing a conductive medium into the detector, especially by means of additive manufacturing, were found to be commercially available. An assessment of the additive manufacturing (AM) market left the following options:

- Metal Inserts - no AM component, similar technique to anode wire introduction;
- Conductive Inkjet Printing - a new AM process;

- Conductive Paste Extrusion - an AM process complementary with FDM; or
- Conductive PLA - a newly developed, composite FDM thermoplastic.

5.1.1 Technique Assessment

Each of the 4 possibilities were researched extensively and assessed as options, with the main points outlined below. Other options beyond this were available, such as metal 3D printing and aerosol jet printing, however, these options were immediately ruled out due to the high cost of these the equipment and operation of the processes.

Metal Inserts

Metal inserts would involve creating metal cathode structures prior and separately to the 3D printing of the detector, and would need to be introduced during printing at the appropriate time, much like the process of inserting the anode wire; a relatively simple solution, once the cathode structures have been made.

The main advantages of using this technique are that the quality of the cathode structure can be easily assessed before being used into the detectors, ensuring rigidity so no changes occur during or after printing; metal is an excellent electrical conductor; and low fabrication costs of basic shapes, such as hollow cylinders.

The disadvantages, however, become significant when moving onto more unique cathode structures: the fabrication of the cathode structures requires the appropriate metalworking equipment; and the complex structures would require significantly higher skill or costs to fabricate, with some of the more unusual geometries beyond the limits of conventional machining and thus impossible to explore.

Conductive Inkjet Printing

Conductive Inkjet Printing (CIP) is a AM technique in which conductive inks, silver nanoparticles suspended in a solvent, are printed directly onto a substrate, such as paper or plastic films, which is then thermally treated or UV cured to form tracks of continuous conduction. Varying degrees of sophistication are available with this technique, from using commercially available inkjet printers (higher quality) and replacing the ink in the standard printer cartridge with conductive ink, achieving track resolutions down to $\sim 100 \mu\text{m}$; to using purpose built CIP inkjet printers which

have programmable settings to control aspects such as inkjet pressure waveforms, with achievable resolutions down to $\sim 5 \mu\text{m}$ [87].

The main advantages of this technique are that any 2-D cathode geometry can be printed; the printing process is simple to use; silver inks are highly conductive; the technique can be used for further circuit development; and the technique could be used to develop electrode structure in other, possible printed gaseous detectors, such as Micro-Strip Gas Chambers and Time Projection Chamber readouts.

The main disadvantages of this technique are that any printed cathodes are effectively 2-Dimensional, making any cathodes difficult to introduce efficiently; the substrates must be flexible, although these can obviously be made more rigid afterwards; the post-processing requires specialist equipment; any cathodes would, like metal inserts, require adding separately; and the conductive ink is relatively expensive.

Conductive Paste Extrusion

Conductive Paste Extrusion (CPE) is an AM technique which occurs alongside FDM as a dual extrusion. In this technique, normal thermoplastic FDM is printed to create a model and a second extruder prints a conductive silver paste throughout the printed model to create 3-Dimensional circuits, which could be utilised to print cathode structures. The paste then dries at room temperature and does not require further processes.

The advantages of this technique are that paste extruders are relatively inexpensive, and are able to be purchased separately and retrofitted to any FDM printer; the cathodes can be printed along with the rest of the detector, minimising the need for further human action; additional circuitry can be printed in the detector, such as printing capacitors for decoupling signals from the high voltage; and almost any supported geometry can be printed.

The disadvantages of this process are that the conductive paste is relatively expensive, similar to the conductive ink; conductive paste is significantly less conductive than metal or silver ink, ~ 5000 times lower; any cathode structure created from the paste must be supported, and so no horizontal overhangs could be printed without a layer of PLA to print onto, adding a resistive layer; and the resolution of paste extruders is quite poor and inconsistent, resulting in non-homogeneous conductive tracks.

Conductive PLA

Conductive PLA is a composite thermoplastic created by Proto Plant [88], which contains ~ 20 wt%¹ carbon black; a highly-conductive, paracrystalline form of carbon produced via the incomplete combustion of hydrocarbons and other organic compounds.

From the initial research, the advantages of using conductive PLA are that the thermoplastic can already be used in the FDM printer, thus not requiring extra equipment; PLA had already been extensively tested and worked with up until this point; the resolution of any cathode structures is dictated by the extruder nozzle, which can be easily changed; the conductive PLA is the cheapest out of all the consumables aforementioned in this section; there is possibility to 3D print components inside the detector, such as capacitors for decoupling signals from the high voltage; the cathodes can be printed along with the rest of the detector, minimising the need for further human action; the ability to 3D printing unique cathode structures remains; and carbon black has a high UV absorption, further increasing the absorption of these photons produced while operating in the recombination region and Geiger-Müller region.

The only disadvantage found was that conductive PLA had the lowest conductivity out of all the options, ~ 20000 times less than CIP silver inks, however, this is not a major disadvantage as resistive cathodes can still be used in SWGDs as previously discussed. High resistive cathodes do pose more risk of space charge build-up of positive ions, reducing the effective bias voltage within the detector; the problem which is meant to be solved by the addition of the developed cathode.

5.1.2 Conclusion

The use of metal inserts, while having some merit, was deemed an unsatisfactory solution, as one of the main advantages of using AM, the ability to create complex structure which are difficult to machine, would be lost. The use of CIP comes with many benefits and possibilities for use in the development of other GDs, however, this technique was also ruled out due to the associated disadvantages, specifically the increased chance of the 2-D cathodes moving inside the detector; the requirements for specialised; and expensive consumables.

¹Percentage by weight.

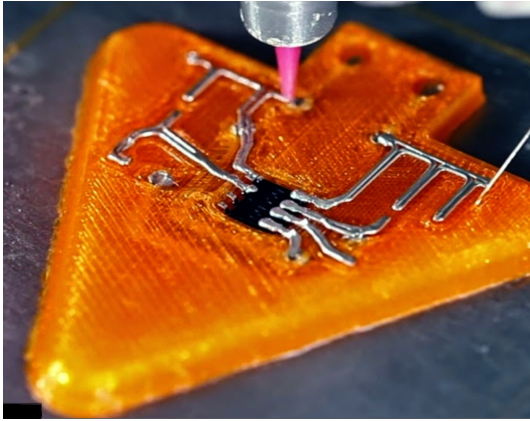


Figure 5.1: Picture of a usable electronic device being printed by the Voxel8 Developer's Kit [89].

Despite the significant disadvantages which come with CPE, it was investigated further as, despite the consumables cost, this was a relatively low-cost solution. Two suitable, commercially-available options were found, the first being the Voxel8 Developer's Kit; a purpose-specific, cost-effective solution to 3D printing usable electronic devices. The Voxel8 was a dual extrusion FDM printer capable of printing thermoplastic from one extruder and Voxel8's patented silver ink from the other.

Voxel8 Silver Ink is a compromise between CIP inks and CPE pastes, delivering high conductivity yet viscous enough to be extruded, making the printer an ideal choice, however, the Voxel8 had a similarly small print volume to the Makerbot, reducing the workable detector model size. Despite the small print volume, a Voxel8 Developer's Kit was initially chosen to be used due to the possibilities that would come from such a system. Unfortunately, at the point of purchase, Voxel8 stopped selling the Developer's Kit ².

The second commercially available option for CPE was the Structur3D Discov3ry; a universal syringe-based paste extruder which can be retrofitted to 3D printers, and is approximately 10 times cheaper than the Voxel8. The Discov3ry was developed for a wide variety of applications, with the aim to print almost any paste material alongside normal FDM, including conductive ink; making the Discov3ry an appealing piece of equipment to explore. Unfortunately, a significantly long time was required to integrate and implement the Discov3ry extruder onto the Gigabot for any research into CPE to occur, and so this technique was left behind.

Given the advantages found with conductive PLA, plus the issues that arose while attempting to explore CPE, conductive PLA was the main avenue investigated as a means of producing an internal cathode. The resistivity of the thermoplastic is a concern, however, resistive cathodes are used in detectors such as Iarocci tubes and,

²Voxel8 only manufactured 100 Developer's Kit before the company transitioned into another company. Many attempts were made to acquire a Developer's Kit but, unfortunately, without success.

thus, conductive filament is an avenue worth exploring. The conductive PLA could already be used with the Gigabot, without any additional expenses or equipment, offering the easiest and most cost-effective solution. As such, the remainder of the work discussed will focus on the development of 3D printed cathode structures using conductive PLA, and the subsequent integration into the printed detector design.

5.2 Printing With Conductive PLA

Given that the enclosure development concluded with the aim of creating triangular, tessellating tracker, the initial test of the conductive PLA was to ensure overhangs can be printed successfully without error. The same overhang test model was printed as that shown in Figure 3.11 and Figure 3.15, with the bottom half removed as this part of the model is redundant when considering the outcome.

Before this could occur, initial experiments were required to determine the optimal print settings for the conductive PLA. Even though the base of the thermoplastic is the same as previously used, the addition of carbon black to the composition significantly changed the properties of the thermoplastic, mainly due to an increase in the mass flow index (MFI); a measure of the ease of flow of a molten thermoplastic. The heater temperature, print speed, and cooling fan speed were the most significant print settings to determine, with some of the more finer settings, such as retraction speed, also needing to be adjusted. Once these settings were fine tuned, the overhang test was printed and the result is shown in Figure 5.2.

The overhang test showed conductive PLA has the best ability to create horizontal structures, when compared to all other thermoplastics tested, with almost no sagging between any of the vertical supports. Unfortunately, however, some flaws with the conductive filament had been observed while testing; the conductive PLA

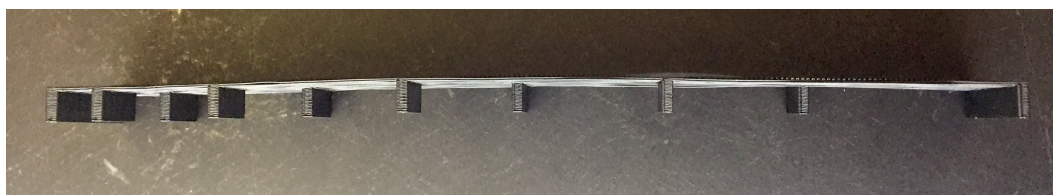


Figure 5.2: Horizontal overhang test, printed in conductive PLA, highlighting the excellent horizontal structure printing.

exhibits poor thermal fusion both line-line and layer-layer fusion, localised to the horizontal overhangs. This effect is clearly visible in Figure 5.3.

Figure 5.3 (*Top*) shows how the majority of the primary overhang layer has separated from those prints above; an issue observed in the overhang tests of previous thermoplastics but not to this extent. Figure 5.3 (*Bottom, Right*) shows the lack of line-line fusion, resulting in a print riddled with holes, again, localised to the horizontal overhang. The conductive filament is already the least conductive solution, given those discussed above, with volume resistivities of $115 \Omega\text{-cm}$ (layer-layer) and $30 \Omega\text{-cm}$ (line-line), and so poor thermal fusion will most likely increase the resistivity of any printed cathodes, but in an inhomogeneous manner which is far from ideal.

Through further observations of conductive filament printing, the cause of this fault appears to stem from the conductive PLA having a greater coefficient of thermal expansion compared to normal PLA. Whilst printing, and the conductive PLA is heated, the issue regarding thermal fusion are not observed, however, as the thermoplastic cools, each printed line contracts and separates from the neighbouring printed lines. This property also appears to be the reason for the superior horizontal overhangs, which print with some sagging and later become taut as the thermoplastic cools. This bulk contraction is highlighted in Figure 5.3 (*Bottom, Left*).

The previous investigation into PLA from various manufacturers found that standard PLA is typically comprised of $> 90 \text{ wt}\%$ PLA, with $\leq 10 \text{ wt}\%$ additives,

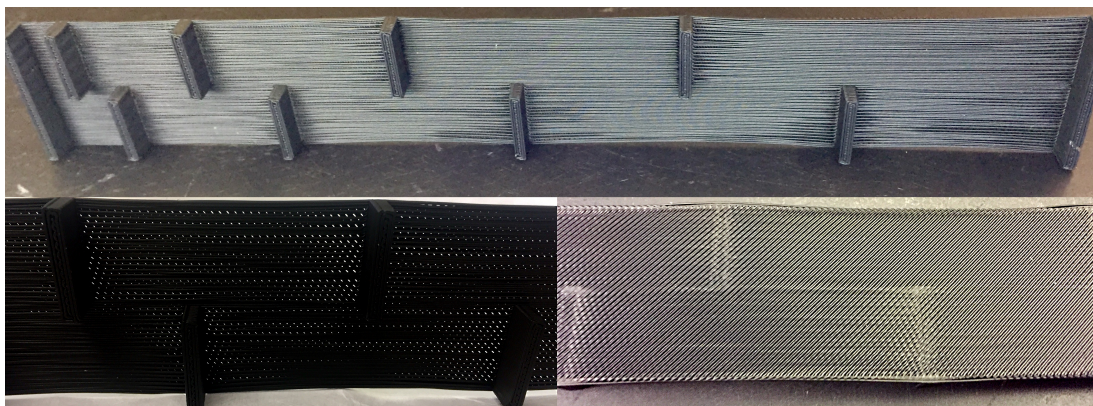


Figure 5.3: Horizontal overhang test, printed in conductive PLA. (*Top*) Visible signs of poor layer-layer thermal fusion. (*Bottom, Right*) Visible signs of poor line-line thermal fusion. (*Bottom, Left*) Visible signs of bulk contraction after cooling.

such as stabilisers or pigments, conductive PLA has a different composition entirely. As previously stated, conductive PLA contains ~ 20 wt% carbon black, however, the remaining components are only ~ 65 wt% polylactide resin (PLA), with the remaining ~ 15 wt% made up of another polymer, which is unstated [90]; presumably retracted by the manufacturer as a key component required for the carbon black to remain in the PLA through heating.

As carbon black has a significantly lower coefficient of thermal expansion when compared to thermoplastics, the addition of carbon black to create a composite material would yield a material with a coefficient of thermal expansion lower than that of the thermoplastic. This is well-documented in cases of other carbon black-composite materials [91][92]. The observed increased coefficient of thermal expansion of conductive PLA must, therefore, originate from the unstated polymer component of the composite thermoplastic.

5.2.1 Preliminary Cathode Structures

Development of 3D printed cathodes continued while taking the initial issues into consideration. The first cathodes attempted took the form of readout strips for a 3D printed TPC (discussed later) as these are simpler structures to print and the techniques learned would feed into the later development and fabrication of SWGD cathodes.

Figure 5.4 shows the first design used to test the limits of incorporating conductive filament structures into normal PLA while using dual extrusion. 22 conductive PLA strips were set to print within a normal PLA substrate, while the thickness of the strip and depth of incorporation into the substrate were varied. As can be clearly seen, very few of the strips began printing at all, and the strips that did printed poorly. A difficult point to notice from Figure 5.4 is that those strips that did begin to print, did not remain intact above the substrate while printing; the printed conductive filament, when printed in thin strips, is very brittle due to the aforementioned poor layer-layer thermal fusion.

The most effective thickness and depth setting for the conductive strips were investigated further in an attempt to print functional readout strips, which can be seen in Figure 5.5. The initial attempts to print these readout strips, once again, consisted of a standard PLA substrate, with the conductive PLA readout strips printed within the substrate, by utilising the dual extrusion feature of the Gigabot.

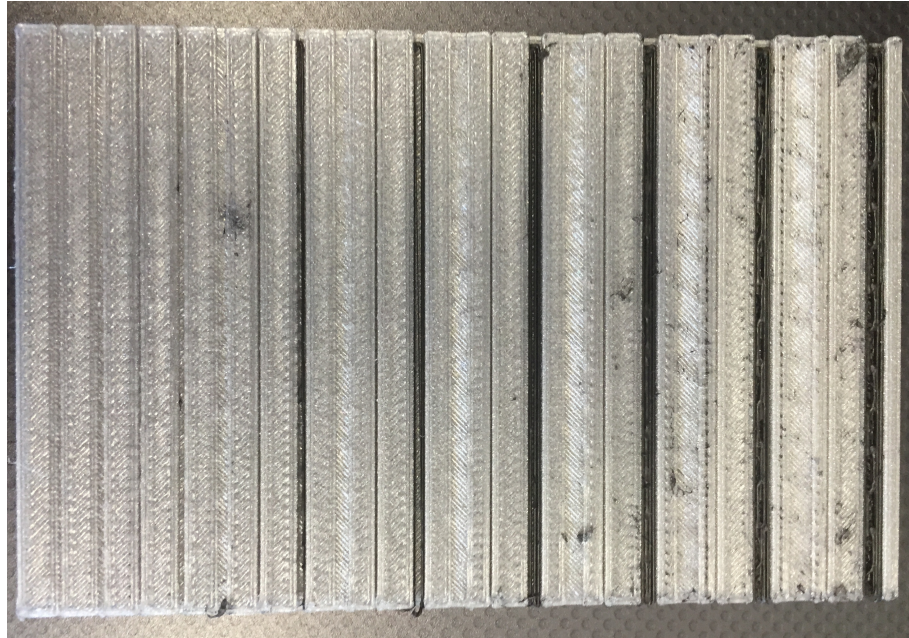


Figure 5.4: Dual extrusion of conductive filament test strips, with the conductive PLA structure incorporated within the normal PLA substrate. 22 different strips were attempted with zero successes.

Dual extrusion FDM is mainly used for multi-colour printing, whereby the same type of thermoplastic is used in both extruders and the process of printing both filaments is relatively simple. Unfortunately, throughout the attempts to find a reliable method of dual printing with standard and conductive PLA, some significant obstacle arose; some of the more notable issues are discussed below. While printing with two thermoplastics, a few options are available to ensure better prints, as issues with intermittent thermoplastic flow can considerably hinder printability. The main solution is for each filament to print a "tower" alongside the model, allowing more frequent flow of thermoplastic from each extruder throughout the print.

While using towers, a significant issue arose due to the higher mass flow index of conductive PLA. During dual extrusion, both extruders maintain the required print temperature, even though only one extruder is used at a time. This meant the conductive PLA tended to flow from the extruder while the standard PLA prints, despite attempts to reduce this occurrence by altering the print settings, e.g. changing retraction speed and length.

Most prints resulted in conductive PLA smeared over the design throughout printing, which can be easily seen in Figure 5.5 (*Left*); other issues also occurred

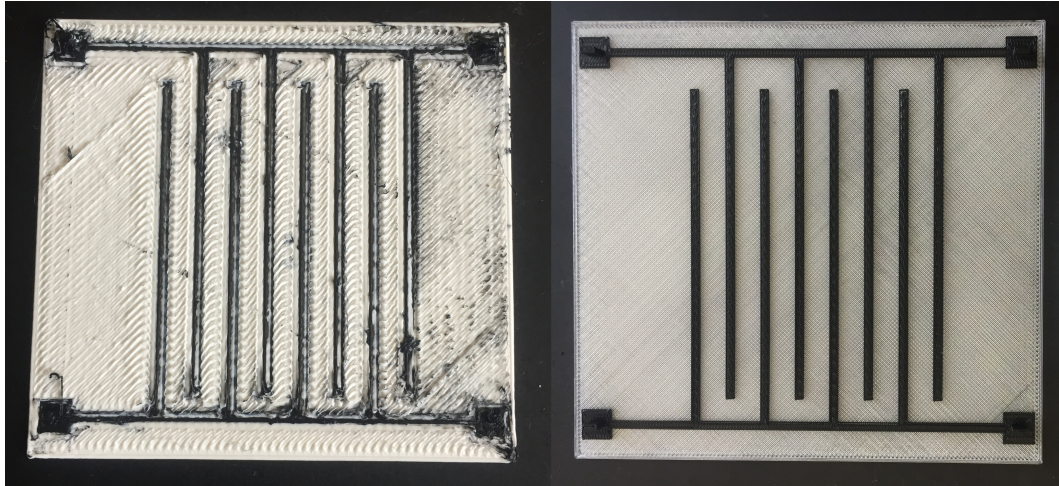


Figure 5.5: Some preliminary attempts to print conductive readout strips. (*Left*) Dual extrusion, with the conductive PLA structure incorporated within the normal PLA substrate. (*Right*) Separate printing, with the conductive PLA structure printed on the normal PLA substrate.

with this print, however, this picture best depicts the stated issues. This is far from ideal and thus could not be used. Printing without towers resulting in insufficient initial thermoplastic flow, and the first layers of the conductive PLA failed to print. Another issue that surfaced from the intermittent printing of the conductive PLA, even while using towers, was due to the conductive PLA being held at high temperatures without flow. Continuously decreasing and increasing the temperature of an extruder throughout a print is not a realistic possibility, and so the conductive PLA must be held at the correct temperature to print throughout the entire print time. Unfortunately, during the extended periods of static heating, the conductive PLA would separate into the individual constituents inside the extruder. The carbon black would coagulate in the extruder, clogging the nozzle and causing print failure.

While the issues discussed were not present in every print, the inconsistency between repeat prints rendered dual printing an ineffective possibility. The only viable solution was to print the conductive filament completely separately to the standard PLA. Figure 5.5 (*Right*) shows the same readout design reprinted with the readout strips no longer embedded within the standard PLA substrate, but instead now printed directly on top of a flat printed surface. The two components are printed as two separate gcode files, where only one of the thermoplastics is used and heated at a time. The figure shown is a scaled version of the design, showing one of the best versions from the developmental stages.

5.3 Cuboidal-Cylindrical Cathodes

Given the verdict of the initial conductive PLA, that dual printing with conductive PLA is not feasible for consistent prints, the development of 3D printed cathodes continued with designing 3D printed cathode inserts. The printed cathode would be printed independently of the main detector and incorporated in a similar manner to the anode wire. Again, this is not an ideal solution as it increases human intervention in the developing method, however, this is difficult to avoid given then progress already made.

5.3.1 Detector V2: Design and Data Collection

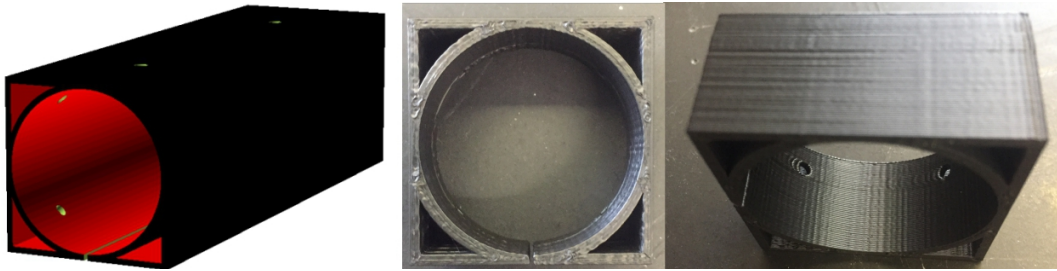


Figure 5.6: *(Left)* OpenSCAD model of the CC cathode to be printed in Conductive PLA. *(Middle and Right)* Printed section of the CC cathode, in conductive PLA. The cylindrical formation is significantly better when printed vertically.

Since the 3D printed cathodes will now be printed separately from the wired enclosure, some of the previously mentioned restrictions of FDM are now removed. The most important consequence of using this method being that the cathodes can be printed in any orientation, removing the need for overhangs, i.e. the cathodes can now be printed vertically where the horizontal cross-section is, mainly, constant; allowing shapes such as cylinders to once again be printed.

As most tubular SWGD are cylindrical, and printing cylindrical cathodes were now a possibility, development continued with the aim to produce a cylindrical-style tube. Cylindrical SWGDs have been tried and tested in many previous HEPP experiments, exhibiting correct operation and having a desirable uniform, radial electric field. Fabricating a 3D printed, cylindrical SWGD should give the best possible results and the best indication that a 3D printed cathode has improved operation. Printing a purely cylindrical cathode, however, will cause issues when it

comes to insertion, and so a modified shape must be made; a cylindrical cathode is combined with a cuboid to produce an Cuboidal-Cylindrical (CC) insert that can fit into a cuboid enclosure. As always, when designing a new detector, a new wire frame was first produced from which accurate dimensions of the detector can be found; ensuring correct anode wire placement. This new wire frame, altered to reduce the amount of thermoplastic needed and reduce costs, is seen in Figure 5.7. The cathode was designed to fill the enclosure and be placed within the detector immediately before the ceiling is printed. The OpenSCAD design can be seen in Figure 5.6 (*Left*); a hollow cuboid with an inner hollow cylinder of radius $r_{cat} = 20.2$ mm. The redundant volumes of the model have been made hollow to decrease print time and the amount of material used. Through-holes which line up with the gas inlets, and interior through-holes to better circulate the drift gas, have been included. A central slit has also been included to allow the insert to fit around the wire, which will already be in position.

The cathode was designed to also have relatively thin walls (1.5 mm) to reduce the amount of contraction upon cooling, which resulted in no significant deviation between the OpenSCAD model dimensions and print dimensions.

A new cuboidal enclosure was designed to accept the printed CC cathode, which was printed using the same method as the previous detector, with one main exception: as mentioned, the gcode was edited further to include a second pause in the print, just before the first ceiling layer, so the cathode can be inserted. Some of the main stages of the detector production are shown in Figure 5.7.

A thin metal wire was fused into the upper side of the cathode prior to insertion, whereby the wire runs along the axis of the cathode, connecting each printed layer to the wire. Using this method, any problems which could arise from the higher layer-layer volume resistivity of the conductive PLA, compared to line-line, are eliminated. When the cathode was inserted, the ends of the wire were secured alongside the anode wire to ensure the enclosure prints over the cathode but leaves the wire free and able to be connected to a HV power supply.

Once the enclosure had finished printing, new end caps were designed. In this detector, the previously used circuit was excluded and reliance on the Tennelec TC 174 Low Noise Preamp for anode HV filtering and signal decoupling resumed. The anode and cathode were each connected to an SHV connector, with the cathode connected via a single low pass filter; a 1 M Ω resistor on the HV supply line, with a 1 nF capacitor to ground. The completed detector, V2, is seen in Figure 5.8.

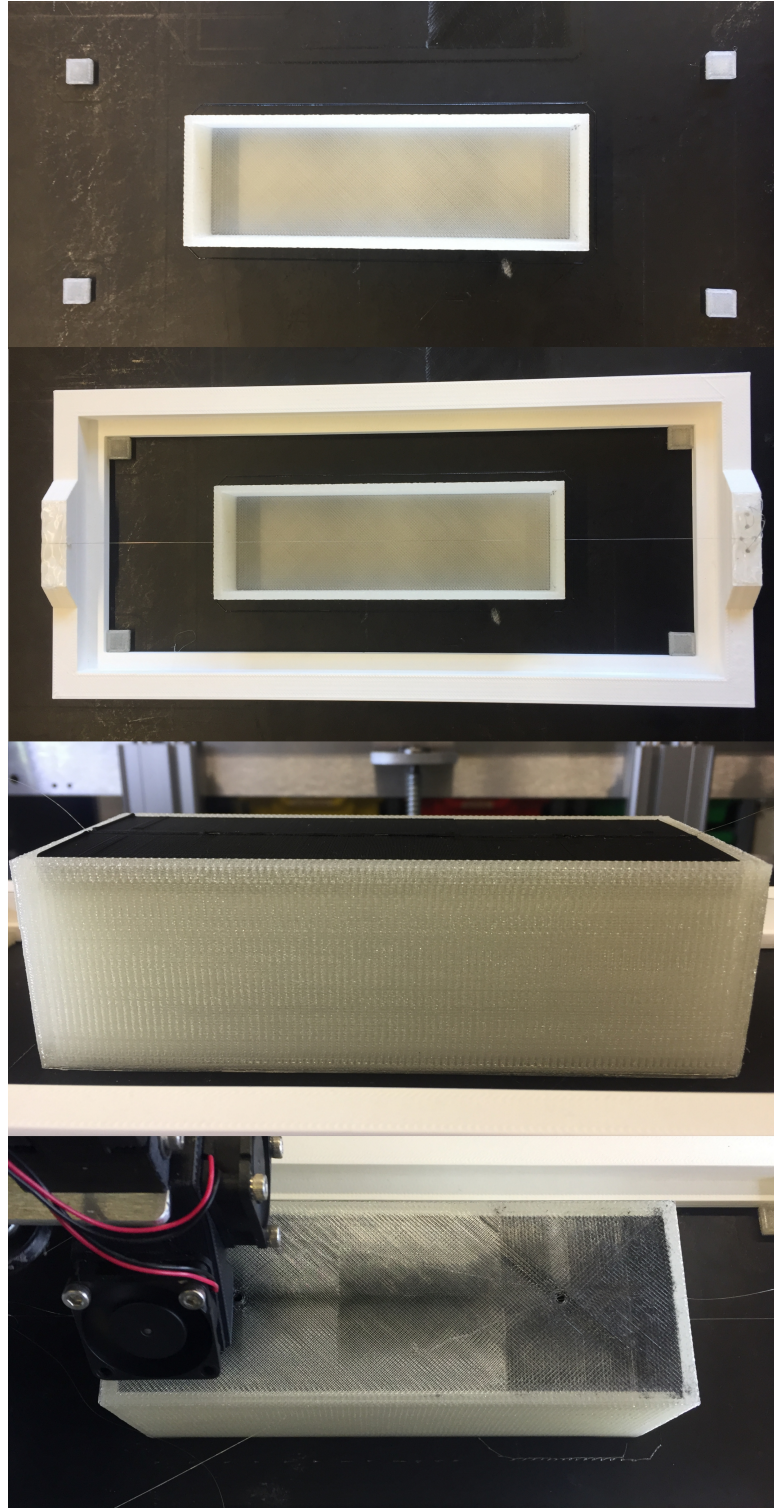


Figure 5.7: A series of photographs showing some of the main stages of detector production: lower layers printed; anode wire introduced; cathode introduction; and ceiling formation.

With the detector assembly completed, the next stage was data acquisition. A similar experimental setup and method as those previously used was adopted once more. The drift gas composition was 2.5% methane, 5% carbon dioxide and 92.5% argon and a low flow rate of 0.05 l/min was used to maintain an oxygen concentration between 85 – 100 ppm. In this case, the CAEN V6521P HV Power Supply Module was connected to the Tennelec TC 174 Low Noise Preamp, which supplied the filtered HV to the detector and handled the signal decoupling and initial amplification. An additional piece of equipment was included to supply a negative potential to the printed cathode; an Ortec 556 High Voltage Power Supply, supplying a constant potential of -100 V to the cathode, via the low-pass filter, throughout the entire data collection.

The detector was operated at bias voltages ranging between 1300 V and 2200 V, in 100 V intervals and, once again, the detector was operated within the aforementioned muon telescope to detect coincidence signals from CRM. Unfortunately, the rate of coincidences from this setup alone was insufficient given time constraints. The bias voltage range was determined by the bias voltage at which the first signals were observed and the maximum rating of the preamp. The final bias voltage of 2200 V was achieved by increasing the negative bias on the cathode, although, without any frequency filter on the power supply, noise from the detector increased significantly at any attempts to go beyond -200 V.

The alternative experimental method was adopted and the strontium-90 source was used to provide a higher rate of charged particles than coincidence CRM alone.



Figure 5.8: Picture of the completed Detector V2, the first 3D printed detector to contain a cathode. The cross-section of the cathode is marked on the detector for identification purposes.

A low threshold, within background, was used once again, and each triggered waveform was recorded and subjected to the selection algorithm, discriminating between signals and non-signals, and fitting curves to the measured peaks.

5.3.2 Detector V2: Results

As before, the pulse heights and rate for each bias voltage are used to determine whether the detector operates correctly and, if so, to determine the voltage ranges for each of the operational regions. Figure 5.9 shows the maximum pulse heights plotted against bias voltage.

The results shown in Figure 5.9 show a constant increase in pulse height with bias voltage. As no signals were observed at a bias voltage < 1300 V, the initial increase gives evidence that the detector had been operated in the recombination region alone. As the inserted cathode has a relatively large radius for a cylindrical SWGD, this result is not surprising, but can be verified by plotting the rates at each bias voltage, which are shown in Figure 5.10

As discussed before, normal operation in the recombination region should result in an increase in rate with bias voltage, as more electron-ion pairs remain separated to become signals large enough to be measured. This increase can be seen in Figure 5.10, further giving evidence that the detector has been operated at bias voltages within the recombination region.

Detector Stability

Once again, to ensure the results shown in Figure 5.9 and Figure 5.10 are representative of the data collected over the operational time of the detector, stability plots have been created for both detection rates and pulse heights, shown in Figure 5.11 and Figure 5.12, respectively. overall average rates used in Figure 5.10 are constant and representative of the entire runtime, further investigation into the recorded rates and pulse heights was performed to ensure no significant changes occur throughout the period of operation.

Both Figure 5.11 and Figure 5.12 show no significant changes in rate or pulse height over the time of operation. Some of the bias voltages, which were operated over a smaller timeframe, do exhibit some larger fluctuations, although this is likely due to the smaller samples taken.

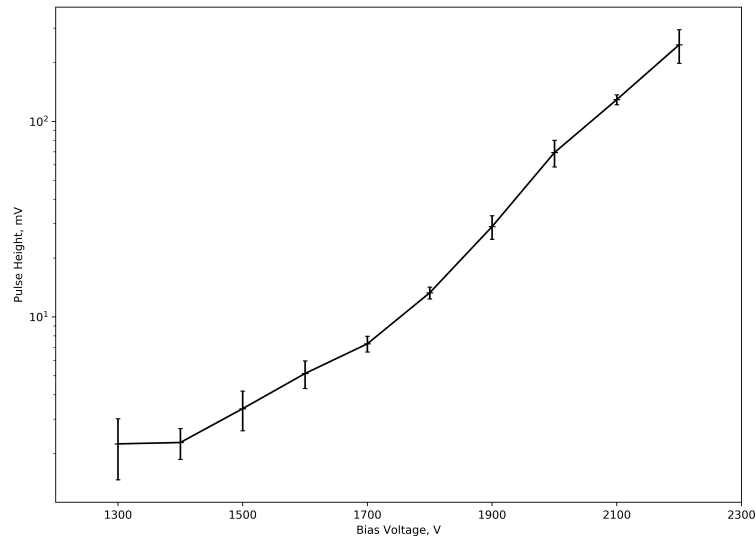


Figure 5.9: Graph of maximum measured pulse heights plotted against applied bias voltage for Detector V2. The maximum electric field, in V/cm, can be found by multiplying the bias voltages by 33.33 cm^{-1} .

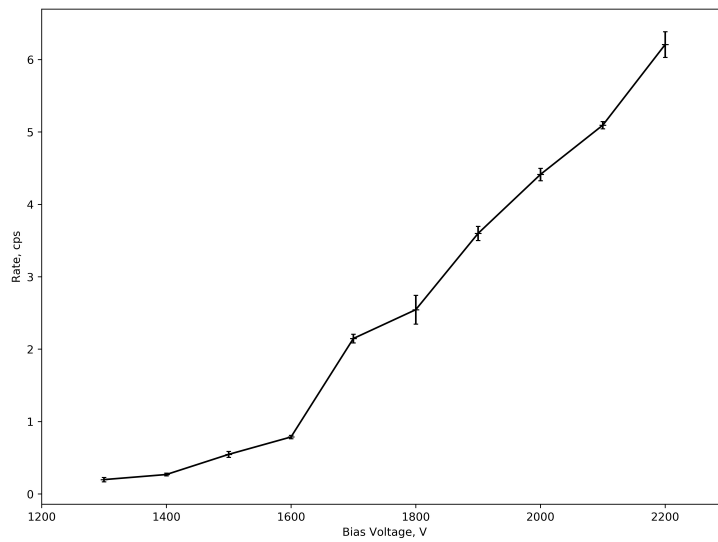


Figure 5.10: Graph of average event rate plotted against applied bias voltage for Detector V2. The maximum electric field, in V/cm, can be found by multiplying the bias voltages by 33.33 cm^{-1} .

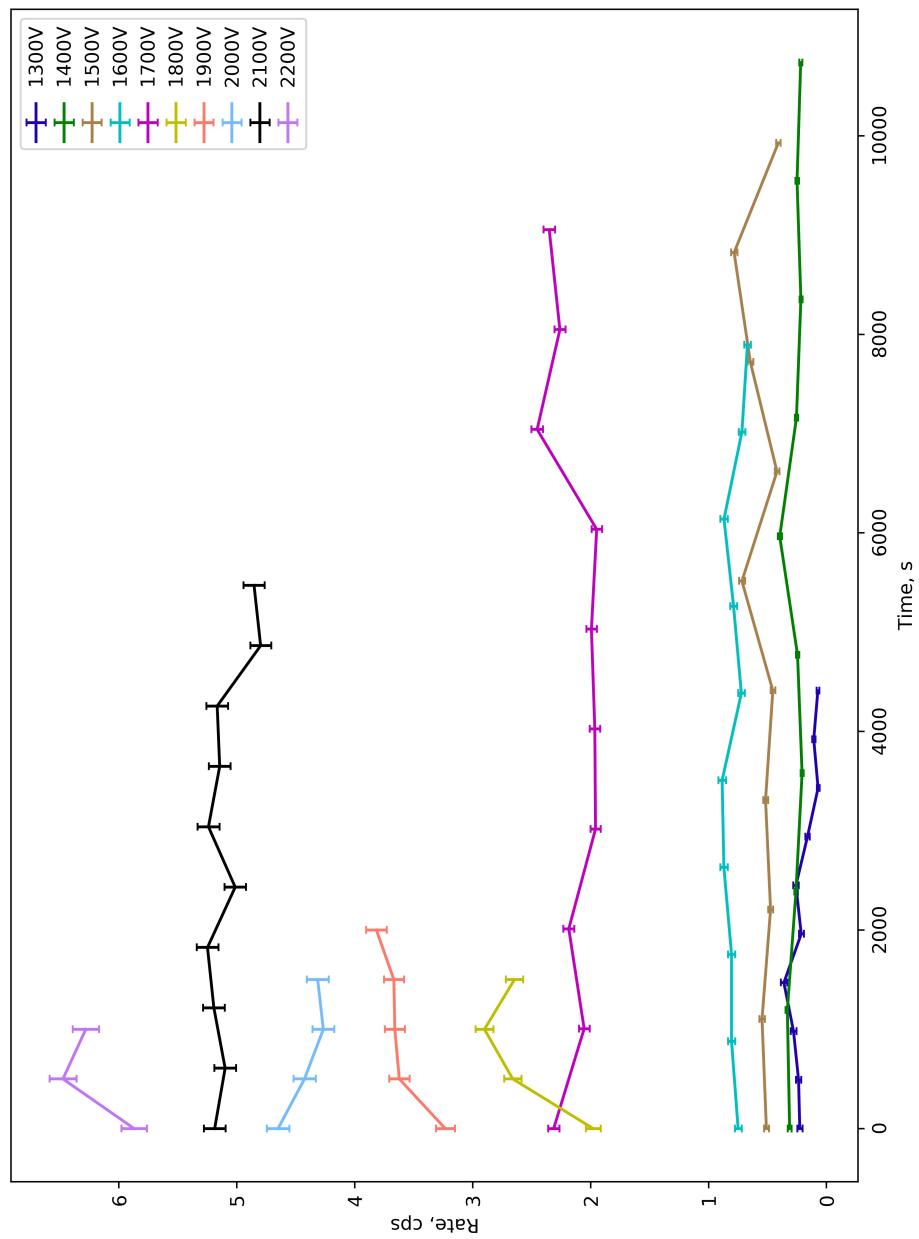


Figure 5.11: Graph showing the change in average event rate over time of operation for Detector V2. As before, the maximum electric field, in V/cm, can be found by multiplying the bias voltages by 33.33 cm^{-1} .

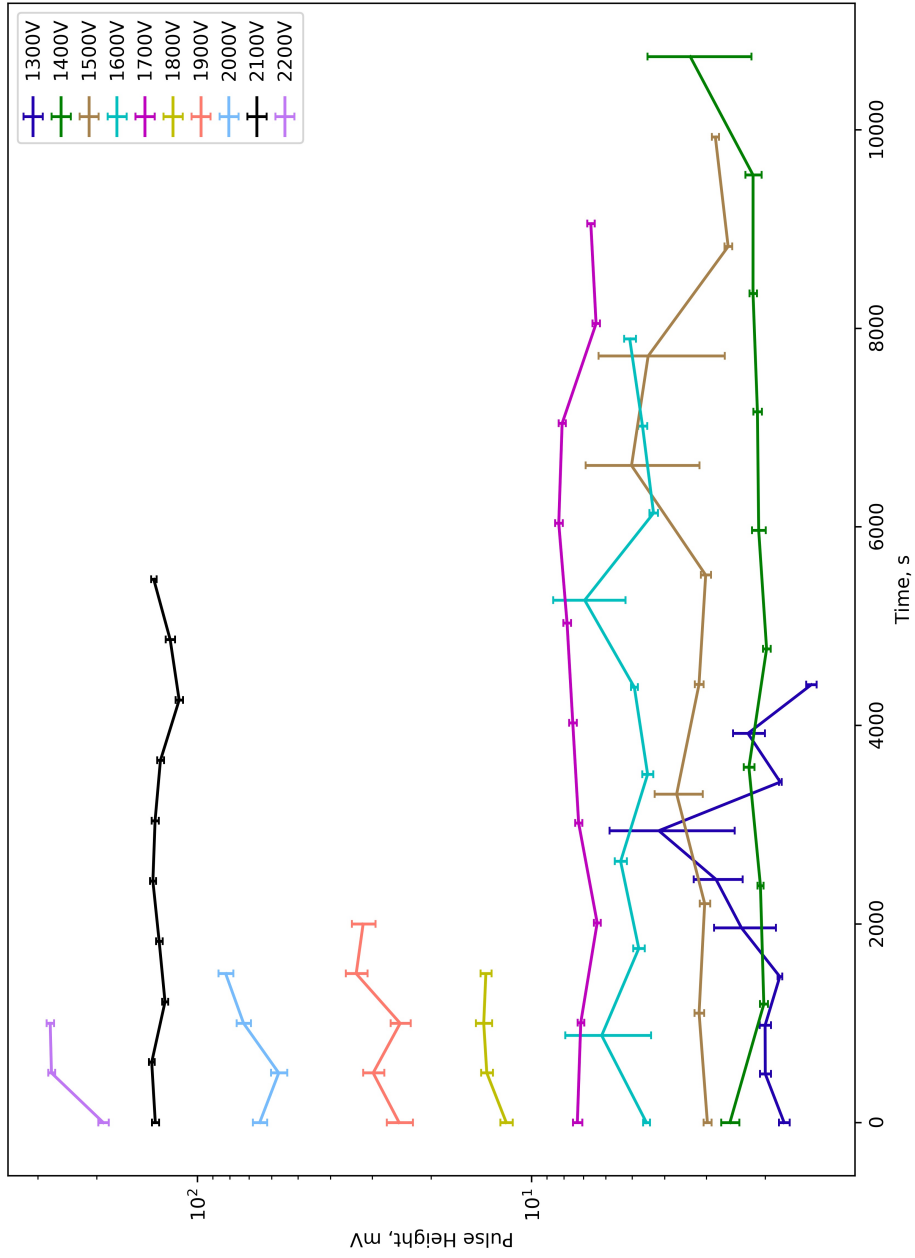


Figure 5.12: Graph of average maximum pulse heights plotted against applied bias voltage for Detector V2. Once again, the maximum electric field, in V/cm, can be found by multiplying the bias voltages by 33.33 cm^{-1} .

As the detector is likely operating solely in the recombination region, given the results in Figure 5.9 and Figure 5.10, any reduction in effective bias voltage due to positive-ion space charge build-up should result in a significant reduction in pulse height and rate observed over the operational time. This has not been observed in Detector V2, which also shows greater stability than that of Detector V1.1, indicating the introduction of the cathode has improved operation. The cathode, however, has a diameter too large to fully characterise the detector over all the operational regions and the development of another detector, with a smaller diameter cathode is desired.

5.3.3 Detector V2: Muon Detection Results

The previous experiments have used a strontium-90 source to produce a higher rate of charged particles but an ideal output of the work carried out in this thesis is to develop a 3D printed muon tracking system. It is therefore desirable to complete a longer experiment in which CRMs are the main source of charged particles.

As mentioned before, relying on coincidences between Detector V2 and the available muon telescope was not ideal as the scintillator blocks used only covered a small portion of the detector, resulting in a low detection rate. However, with signals from CRMs already detected with the coincidence setup, proving detection possible, Detector V2 was left to collect data without coincidence or the strontium-90 source. The same setup as that used in Subsection 5.3.1 was adopted to collect the data, without the Strontium-90 source included and a longer runtime allowed.

If operation has, so far, been unhindered by the use of strontium-90 source, i.e. the increased particle flux at a single point in the detector, the pulse height data from this operational runtime are expected to yield the same results as previously found, whilst the rate data should yield the same overall shape, but scaled down to account for the lower flux of charged particles incident on the detector.

An immediate difference found while operating the detector was the range of bias voltages used. Whereas in the previous operational run, the range of voltages used were 1300 – 2200 V, however, the minimum bias voltage used was 1400 V due to this extremely low detection rate observed at 1300 V.

The maximum operational bias voltage found during this setup varied slightly to 2500 V. This was due to the cathode being able to reach an output of -500 V without large amounts of induced noise.

The higher achievable maximum bias voltage does indicate an issue with having a higher flux of charged particles incident on the detector, presumably as these are mainly focused at one point in the detector. The constant ionisation of the same region could produce a region of free charges in the drift gas, somehow coupling any noise on the cathode to the anode wire.

Previously, the top 10% of pulse heights have been used for the pulse height vs bias voltage graphs, however, this was used to exclude any contributions from the strontium-90 source, which would produce lower amplitude signals. As this source of particles has been excluded from this experiment, an average from the entire dataset has been used in this case.

The pulse heights are plotted against bias voltage in Figure 5.13 and, as expected, the results are indicative of operation in the recombination region, with a steady increase in average pulse height with applied bias voltage. While comparing the results of shared bias voltages in both Figure 5.9 and Figure 5.13, the plotted pulse heights also show little variance in magnitude, extending of the range amplitude range. This is to be expected, however, the result indicates that using the top 10% of pulse heights in previous results as a representative sample of CRMs while disregarding contributions from the strontium-90 source.

The rates are plotted against bias voltage in Figure 5.14 and, expectedly, show the steady increase indicative of operation in the recombination region, with the magnitude of the rates significantly decreased due to the removal of the strontium-90 source. While the observed increase is not as linear as the results from Figure 5.10, this variability is expected from such low rates. The difference in the range of measured rates between Figure 5.10 and Figure 5.14 does allow an approximation to be made for the efficiency of detecting strontium-90 beta particles. As the strontium-90 source emits beta particles into the detector at a rate of $\sim 15 \text{ s}^{-1}$, by using conservative value, the detector can be estimated to be $\sim 25\%$ efficient in this case, although the errors on this approximation are large and this is specific to the source.

The results found in this experiment are similar to those found when a strontium-90 source is present. The ability to apply a greater voltage on the cathode without the strontium-90 source may, however, indicate a higher flux of charged particles has a significant effect on the possible applied bias voltage range.

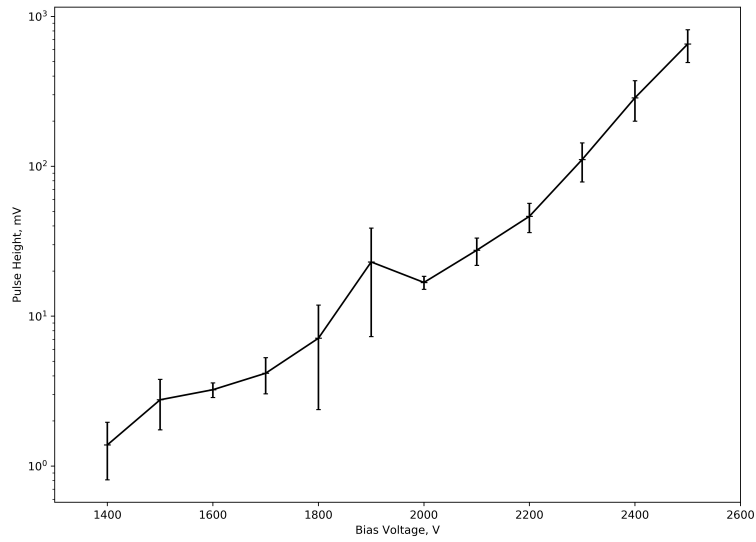


Figure 5.13: Graph of maximum measured pulse heights plotted against applied bias voltage for Detector V2, with no Sr-90 source present. As before, the maximum electric field, in V/cm, can be found by multiplying the bias voltages by 33.33 cm^{-1} .

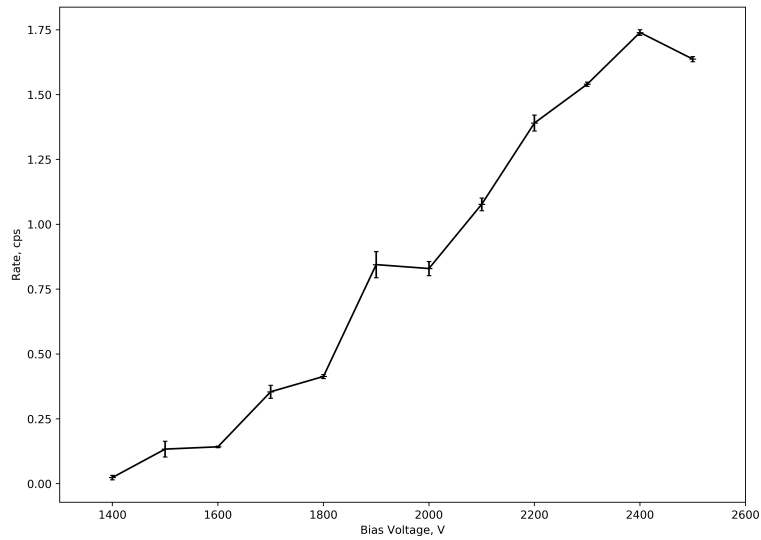


Figure 5.14: Graph of average event rate plotted against applied bias voltage for Detector V2, with no Sr-90 source present. Again, the maximum electric field, in V/cm, can be found by multiplying the bias voltages by 33.33 cm^{-1} .

Detector Stability

For completeness, stability plots for both the rates and pulse heights have been created, as have been done for all other experiments, shown in Figure 5.15 and Figure 5.16. Once again, both graphs exhibit high levels of stability over the time of operation, especially the pulse height data. An initial, constant decrease is observed in the rates for 1500 V, but stabilises over time and does not appear to have any effect on the pulse height data, which would be expected if this decrease was due to a decrease in effective bias voltage.

Some large rate fluctuations are observed while operating at other applied bias voltages, i.e. 1700 V, 1900 V and 2000 V, however, these appear to also stabilise over time and do not have a significant effect on pulse height. Stability while operating at 1900 V may be an exception as fluctuations in pulse height do appear to follow the fluctuations observed in the rate data, indicating a change in effective bias voltage within the detector. This is only observed at 1900 V, and does appear to stabilise towards the end of the operational time, although, without a longer runtime this cannot be said with confidence.

5.3.4 Detector V2: Detector Summary

The first 3D printed SWGD, containing a 3D printed cathode, had been printed using the FDM process while utilising the use of conductive PLA. The need to include a cathode into the detector, while previously determined as significant stage in the development of the printed detectors, was evident due to the operational performance of Detector V1.1, which exhibited uncharacteristic behaviour.

The detector was operated with and without a strontium-90 source present, while measuring background and CRMs throughout; altering the flux and range of charged particles incident onto the detector. Analysis of the results from both experiments yielded the same conclusion, that over the range of applied bias voltages, the detector was being operated in the recombination region; with the rates and pulse heights increasing with bias voltage. While an investigation into higher voltages is desirable, this detector was dependant on the voltage rating of the Tennelec TC 174 Preamp and the radius of the cathode meant these greater electric fields were unachievable.

Despite only being able to characterise the recombination region, this is ideal for initial stability investigations, determining whether the cathode had improved detector operation and decreased any possible space charge build-up; any decrease

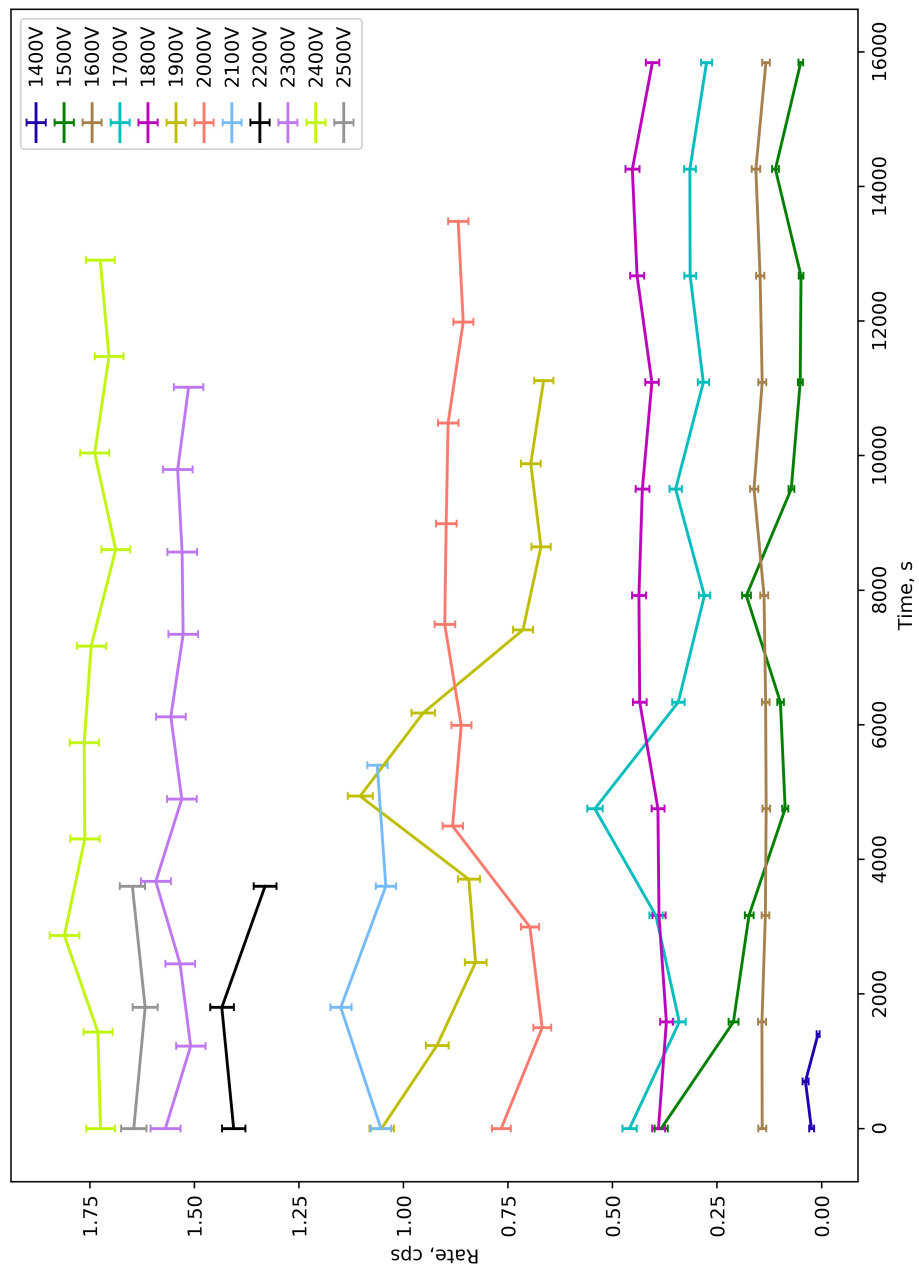


Figure 5.15: Graph showing the change in average event rate over time of operation for Detector V2, with no Sr-90 source present. As before, the maximum electric field, in V/cm, can be found by multiplying the bias voltages by 33.33 cm^{-1} .

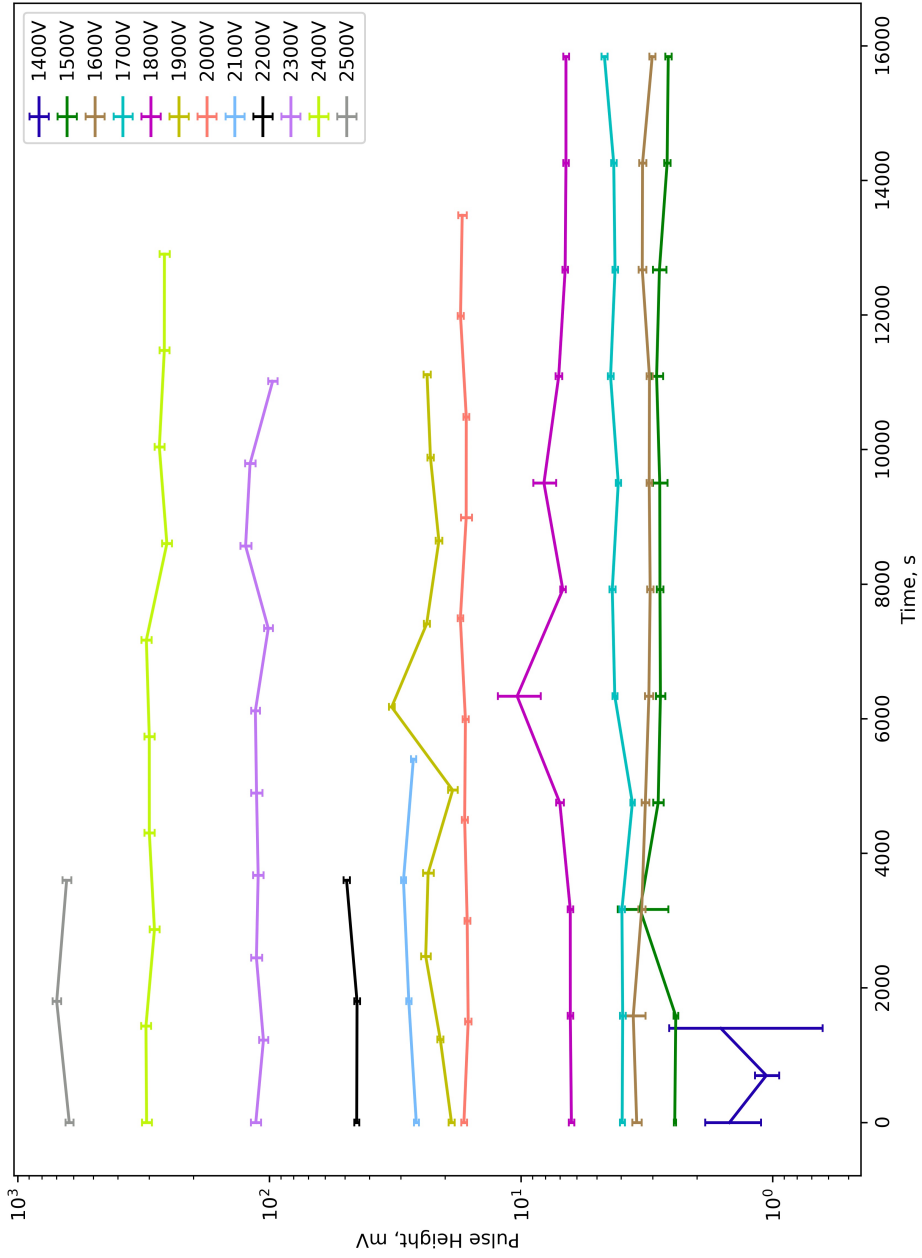


Figure 5.16: Graph of average maximum pulse heights plotted against applied bias voltage for Detector V2, with no Sr-90 source present. Again, the maximum electric field, in V/cm, can be found by multiplying the bias voltages by 33.33 cm^{-1} .

in effective bias voltage would result in a significant, observable reduction in average pulse height and rate.

The results demonstrate the cathode may have improved operation, with stable operation occurring in this highly variable operational region, with no constant decreases in rate or pulse heights observed; indicative space charge build-up. The observed rates are, however, relatively low over operation in the applied bias voltage range, and so no significant space charge build-up could have been created. Increasing the detection rate is required to further investigate whether or not the cathode has improved detector performance.

The operation of Detector V2, while showing positive results for the project, still indicate further development is needed and a new detector is required to be designed, printed and tested, while still using the methods developed beforehand. With each new detector fabricated, the developed method is refined and the reliability of the basic, learned principles of 3D printing GDs is further evaluated.

5.4 Triangular Insert, Cylindrical Cathode

Given the success of the cuboidal-cylindrical cathode used in Detector V2, another cylindrical cathode was designed within a triangular insert. The design of this cathode was for 3 main reasons: to ensure the production steps were successful with a different cathode shape; to make a step towards the desired tessellating, triangular detector, discussed in Subsection 3.4.1; and to test a smaller radius cathode. The smaller cathode radius should result in more operational regions to be observed and higher detection rates to be investigated, to further determine whether the inserted cathode is improving detector performance and decreasing space charge build-up. The smaller cathode radius will, however, result in smaller signals as only shorter ionisation tracks are possible in the reduced detection volume.

5.4.1 Detector V3: Design and Data Collection

An enclosure with an internal triangular volume had already been designed for Detector V1, thus the same design could be used. The current dimensions would result in a cylindrical cathode with a radius of $r_{cat} = 7.36$ mm, resulting in gas volume too small; reducing both the detection rate and the number of initial electron-ion pairs created in the detector. By utilising one of the main benefits of using CAD

to design detectors, the model was simply scaled up in OpenSCAD, resulting in an enclosure that could accommodate a cathode with a cylinder radius $r_{cat} = 13.7$ mm, resulting in electric fields up to ~ 1.58 times greater than those achieved with Detector V2 (at the cathode surface, over the same applied bias voltages). The wire frame design used for V2 was scaled to the appropriate anode wire level and was, once again, printed first to ensure correct positioning would occur.

The Triangular-Cylindrical (TC) cathode, also dubbed the *Deathly Hallows* cathode, was designed to fit inside this scaled triangular enclosure. The design and partial print can be seen in Figure 5.17. Once again, any redundant volumes of the model have been made hollow to decrease print time and the amount of material used; through-holes for gas circulation have been added; and a central slit created to fit around the anode wire. The TC cathode was designed to also have thinner walls than the previous print, at 0.8 mm, minimising the plastic required once more. The same method as V2 was carried out to fabricate the detector, with a wire fused along the axis of the cathode again and inserted prior to the first layer of the enclosure ceiling. New end caps were designed to fit to the detector, as the new design had a rectangular cross-section, whereas V2 has a square cross-section.

The new detector, V3, was also constructed to contain two of the circuits seen in Figure 4.7. One circuit, connected to the cathode wire, contained only the HV filtering components and was housed inside an end cap at one end of the detector, with an SHV feedthrough attached. This addition was to remove the possible noise that could be introduced to the cathode from the unfiltered Ortec 556 HV supply.

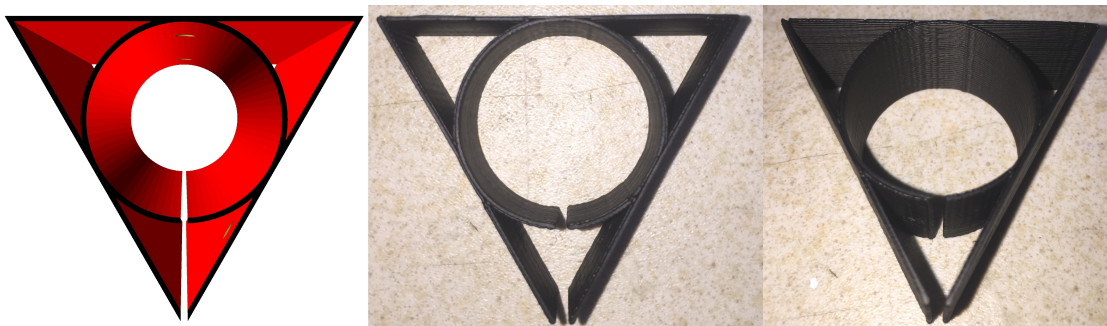


Figure 5.17: (Left) OpenSCAD model of the TC cathode to be printed in Conductive PLA. (Middle and Right) Printed section of the TC cathode, in conductive PLA. The cylindrical cathode has, once again, formed significantly better from being printed vertically.

The second circuit used is the full set of components shown in Figure 4.7, i.e. contains both HV filtering and signal decoupling. The circuit was also modified by adding a resistive coating, to reduce the chance of sparking across components at higher voltages. This circuit was connected at the opposite end of the detector, directly to the anode wire. Two SHV connectors were added to the end cap: one to supply HV to the anode, via the circuit; and another to output the decoupled signal to the Tennelec TC 174 Low Noise Preamp, which is still required to amplify the smaller signals enough to be measured. As the anode HV will be decoupled from the signal prior to the Tennelec TC 174 Preamp, this will increase the range of bias voltages which could be applied; the voltage range will then be dictated by the point at which signals are observed and the breakdown voltage of the circuit. The completed detector can be seen in Figure 5.18.

For the operation and testing of Detector V3, the same setup as that used in Subsection 5.3.1 was adopted once again. A low flow rate of 0.035 l/min was used and the oxygen level in the detector was maintained at 70–90 ppm. The strontium-90 source was, once again, used to supply a higher flux of charged particles.

The detector was operated at bias voltages ranging between 1000 V and 2800 V, in 100 V intervals. Once again, the lower value was dictated by the voltage at which the first signals were observed. The largest bias voltage was determined by the point when breakdown occurred within the detector and constant discharge was observed. A low threshold, within background, was still used and the triggered waveforms recorded. The same selection algorithm which has been used with all other datasets was used once more and the results shown below.



Figure 5.18: Picture of the completed Detector V3; a 3D printed detector to contain a smaller radius cathode than V2. The cross-section of the cathode is marked on the detector for identification purposes.

5.4.2 Detector V3: Results

The pulse heights from Detector V3 have been plotted against applied bias voltage and are shown in Figure 5.19. The graph presented shows the best resemblance of Figure 2.1 out of all the detector results so far, depicting the most operational regions.

The recombination region can be seen in the bias voltage range 1000 – 1400 V from the characteristic increase with bias voltage. A small plateau, indicative of the ion chamber region, is observed between 1400 V and ~ 1700 V, followed by a large increase whilst operating at ~ 1700 – 2100 V, typical of the proportional region.

After the proportional region, a plateau should follow indicating the Geiger-Müller region, however, instead a decrease is observed over the bias voltage range 2200 – 2500 V. Given the larger avalanches and positive ion shielding that can occur in the Geiger-Müller region, a reduction in pulse height is expected, although not to this degree; possibly indicating the resistive 3D printed cathode is not capable of reliable operation at these higher bias voltages. A final increase is observed again, in the range 2500 – 2800 V, at which breakdown began to occur.

Figure 5.20, which has the average rate plotted against applied bias voltage, shows further evidence of correct detector operation; with the exception of the initial dip in rates, which cannot be explained. However, a general increase is observed over the bias voltage range corresponding to the recombination region, which is expected for normal operation. A long plateau in rates then follows over the majority of the remaining bias voltage range which is, once again, the expected result for normal operation.

A slight reduction can be seen to correspond with the suspected Geiger-Müller region; characteristic of operation in this region due to the associated large dead-times. A sharp increase then follows where continuous breakdown begins to occur; while this also has large detector dead-times, this does not rely on a charged particle for the breakdown to occur, which could result in a larger rate seen.

Detector Stability

To further analyse the results, and ensure the rates and pulse heights observed in Figure 5.20 and Figure 5.19, respectively, are constant and representative of the entire data, stability plots have been created once again.

The stability plot for rates, shown in Figure 5.21, show no significant changes

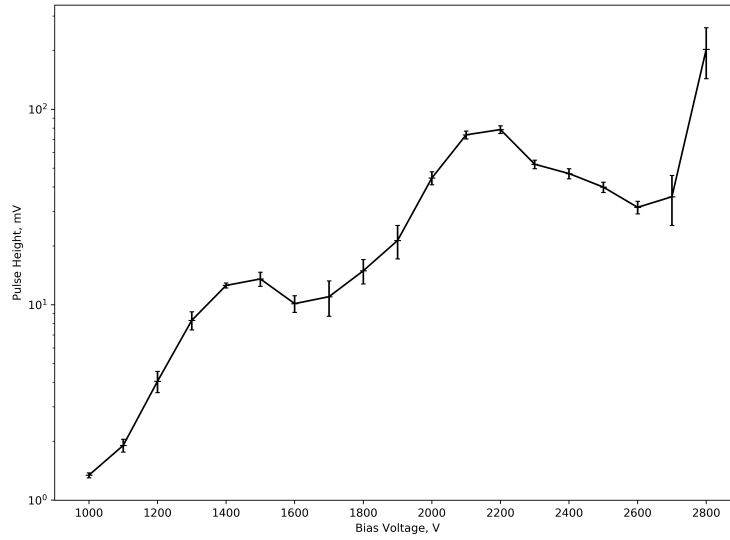


Figure 5.19: Graph of average maximum measured pulse heights plotted against applied bias voltage for Detector V3. The maximum electric field, in V/cm, can be found by multiplying the bias voltages by 35.63 cm^{-1} .

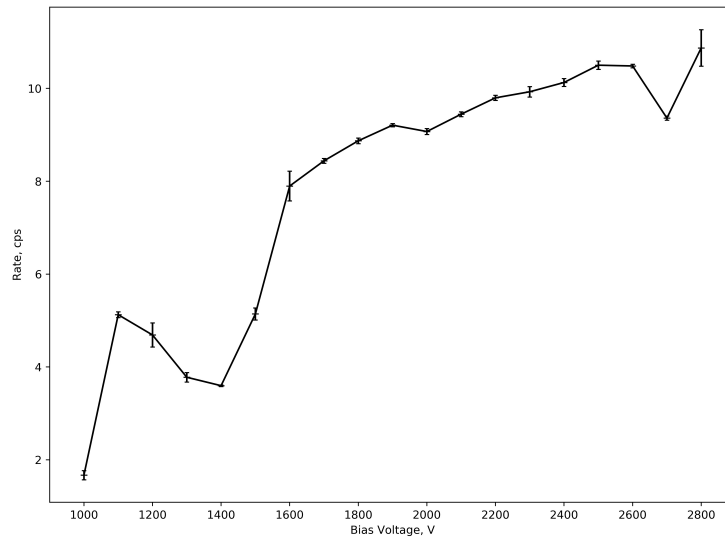


Figure 5.20: Graph of average event rate plotted against applied bias voltage for Detector V3. The maximum electric field, in V/cm, can be found by multiplying the bias voltages by 35.63 cm^{-1} .

in rate occur over time for the applied bias voltages. An increase at 1200 V, and a decrease at 1000 V, are observed initially, however, both voltages stabilise after ~ 200 s of operation. A significant, constant decrease in rate is observed over operation at 2800 V, however, this is expected given the constant breakdown of the detector gas.

The stability of the pulse heights is plotted in Figure 5.22, showing stability over all applied bias voltages, disregarding the results from 2800 V which are not true, particle-induced signals.

5.4.3 Detector V3: Detector Summary

Detector V3 was fabricated, using the same methods as those used for V2, but created to contain a 3D printed cathode of a smaller radius and of a different insertable shape. The ability to produce Detector V3 evaluated the reliability and reproducibility to the basic detector design components and fabrication method while the cathode of a smaller radius was used to increase the possible electric field within the detector; resulting in more operational regions to be investigated.

The fabrication of Detector V3 was completed without any alteration to the previously described technique, indicating the method is fit to produce operational detectors, even with different internal structures and cathode shapes, given the basic components have the required, mentioned features.

The included circuits allowed Detector V3 to be tested over a larger range of bias voltages than Detector V2, revealing correct, characteristic operation over all bias voltages. The data gathered corresponded to the expected results outline in Figure 2.1 and identification of all the operational regions occurred, with stability plots further indicating correct operation.

The introduction of the 3D printed cathode, despite the high resistivity, has significantly improved detector operation when compared to Detector V1.1. The effects, suspected to be caused by space charge build-up, have been successfully removed indicating that FDM is a viable means of producing both detector enclosures and cathode structures. It should be noted, however, that the detectors have only been operated while exposed to a low flux of particles; the limit at which the 3D printed cathode can neutralise positive ions is still yet to be determined.

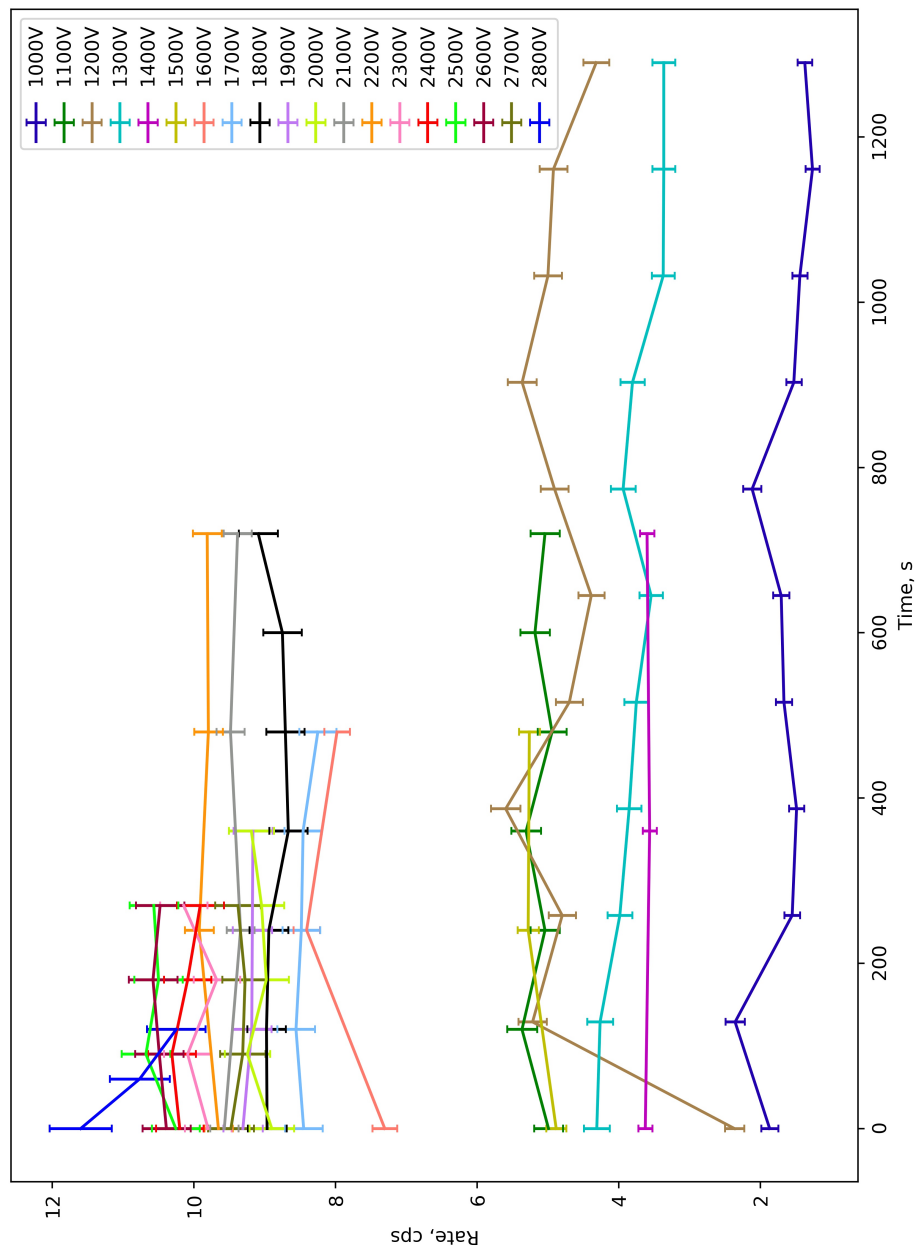


Figure 5.21: Graph showing the change in average event rate over time of operation for Detector V3. As before, the maximum electric field, in V/cm, can be found by multiplying the bias voltages by 35.63 cm^{-1} .

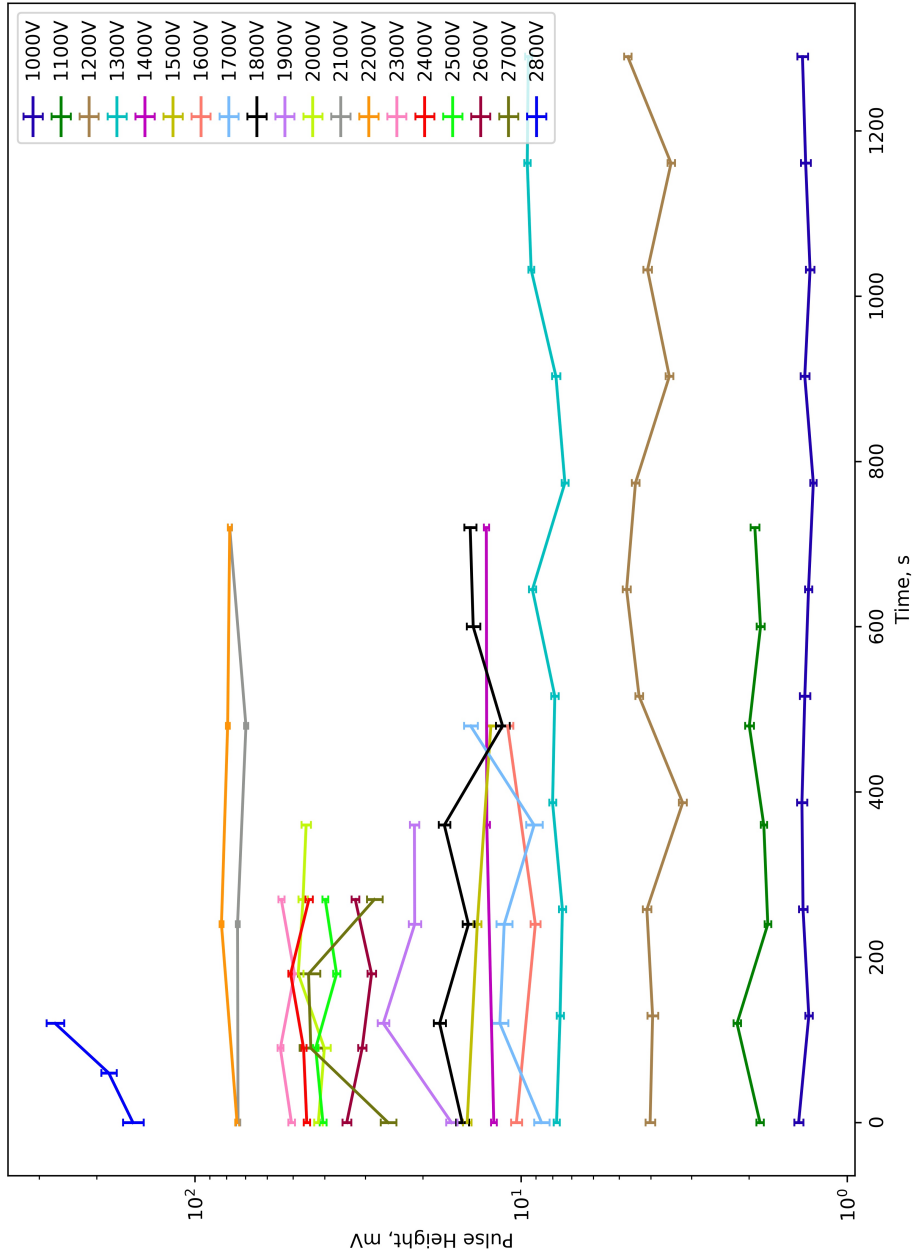


Figure 5.22: Graph of average maximum pulse heights plotted against applied bias voltage for Detector V3. Again, the maximum electric field, in V/cm, can be found by multiplying the bias voltages by 35.63 cm^{-1} .

Chapter 6

Operational Detectors: Novel Triangular Cathode Design and The Muon Tracker

As mentioned throughout this thesis, a conscious effort has been made to direct the work made with 3D printed GDs towards the development of novel detector designs; more specifically, to produce a tessellating, triangular muon tracker which could operate in a similar manner to the MINER ν A scintillating bars, discussed in Subsection 3.4.1.

6.1 Muon Tracker: Concept Design

Early on in this body of work, a simple concept design was created for a fully-scalable, multi-layer, multi-wired muon tracking system, with the aim to create an operational detector. The concept of this tessellating, triangle detector is based on the fact that the number of primary electron-ion pairs created in a drift gas, by a charged particle of a given energy, is dependent on the path length of the particle through the detector. Given this, the ratio of pulse heights between two, neighbouring tessellating, triangular detectors, created from the same muon, could be used to reconstruct the trajectory of a muon, rather than using the commonly used timing method to reconstruct position. The basic concept of operation is depicted in Figure 6.1.

A design was created on OpenSCAD, whereby the number of tessellating tri-

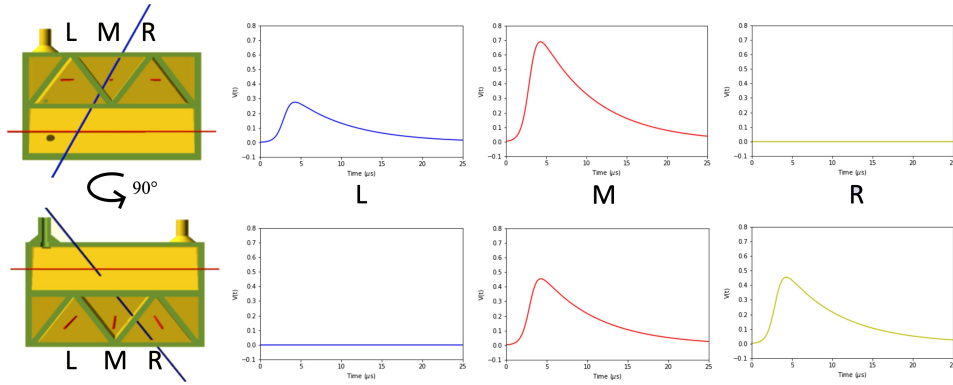


Figure 6.1: Depiction of tracker operation, whereby the muon path length is proportional to measured pulse height, further aiding in track reconstruction.

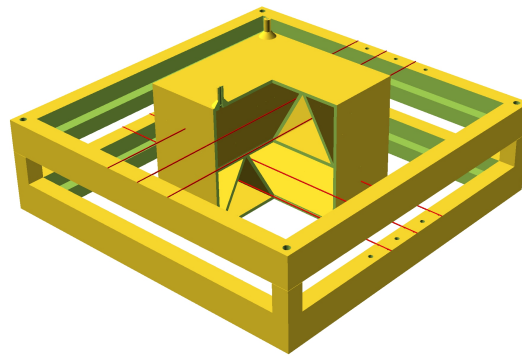


Figure 6.2: OpenSCAD model of the muon tracker concept model, with a segment removed. Wires and stackable wire frame is included

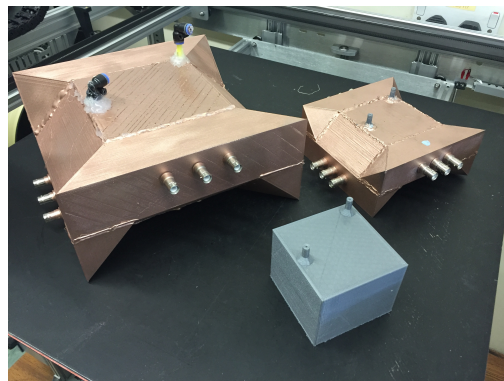


Figure 6.3: The 3 initial prints of the muon trackers, printed using the concept model.

angles per layer (or chambers), and the number of super-layers (2 orthogonal layers), is entered and the tracker is built to that specification, with the wire frames included. The only extra step required is to add the gas inlets and through-holes, as the variables affect the positioning. A design for 3 tessellating triangles per layer by one super-layer can be seen in Figure 6.2.

It should be noted, as this is was a concept design, the wire frame has not been made to realistic specifications. The model was created to ensure a larger enclosure, with multiple wires, could be printed, remain gas-tight and sustain gas flow to all chambers. As the centre of an equilateral triangle is the point equidistant from each corner, rather than half the height, a wire frame of constant height, for a layer of tessellating triangles, will result in each wire being too high or too low depending on the orientation of the triangle.

The design was printed 3 times: a small system of chambers, (85 mm \times 85 mm \times 70 mm), as a preliminary test; the same system with wires, to ensure gas-tightness can still occur; and a system of the same number of chambers and super-layers, but scaled up by a factor of 1.6, so each chamber is larger, to test the limits of size vs gas-tightness. These 3 prints can be seen together in Figure 6.3.

The interesting shape of the detectors is due to the new end caps, whereby 4 of the same shape can house all the anode wires and circuit boards, and can tessellate around the detector to fully encompass each side. This end cap shape can be seen in Figure 6.4. The smaller, wired system printed successfully and could sufficiently hold a gas composition with < 300 ppm at a flow rate < 0.1 l/min. A higher flow rate was required, when compared to the smaller detectors discussed so far, although this was expected due to the increased surface area of the detector and the increased number of wires protruding from the enclosure.

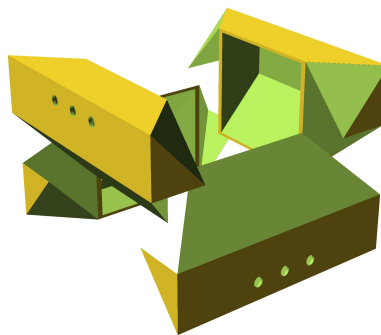


Figure 6.4: The 3 initial prints of the muon trackers, printed using the concept model.

Unfortunately, the larger system did not print as expected, resulting in a periodic loss of filament deposition throughout fabrication. This was detrimental to any gas-tight test attempted and fabricating another larger system would require too much

material. The success of the smaller system was still cause for further development and with the results from the 3D printed cathodes improving, combining the two was the next step.

6.2 Triangular Inserts, Graded Cathodes

While the Triangular-Cylindrical (TC) cathode in Detector 3 is, substantially, the best cathode/detector combination made so far, using the TC in this muon tracker negates the purpose of the tessellating, triangular shape due to the non-overlapping detection volumes. Alternatively, a triangular cathode insert, which produces the same electric field as a cylindrical cathode could be developed; required for regular, consistent avalanches to occur around the anode wire, independent of direction.

The detector could operate in recombination region, however, this is not a reliable region of constant operation due to the variability in rate and pulse height associated with fluctuations in effective bias voltage. The detector would be more stable in the ion-chamber region, where signal height is directly proportional to the amount of primary electron-ion pairs, but the difference in pulse heights for the triggered detectors could be too small to measure accurately, propagating into poor reconstruction. The detector should operate in the proportional region, hence the requirement for consistent avalanches. The pulses from operating in this region will be amplified significantly during avalanche (dependent on the drift gas used) and a greater difference can be measured for a more accurate ratio and, consequently, muon trajectory reconstruction.

Typically, shaping an electric field uses a system of resistors as potential dividers, which is not completely feasible in this case, or a combination of different potentials and electrode size/position, as has been used to shape the field in the barrel muon system of the CMS detector, shown in Figure 3.2. Focussing mainly on using electrode size and position as a means of shaping electric field, a geometric solution was investigated, utilising the ability of FDM to easily fabricate unusual or complicated shapes.

6.2.1 Detector V4: Design and Data Collection

A variety of different possible solutions were designed, some of which proceeded to being turned into OpenSCAD models and attempted to be printed. The designs

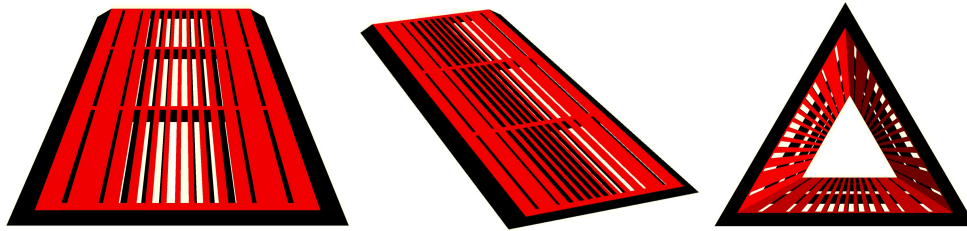


Figure 6.5: OpenSCAD model of the first graded cathode. The horizontal struts are to aid correct formation during printing.



Figure 6.6: Attempt at printing a cathode in conductive PLA. The design featured strips which were too fine to print and poor thermal fusion of the filament occurred.

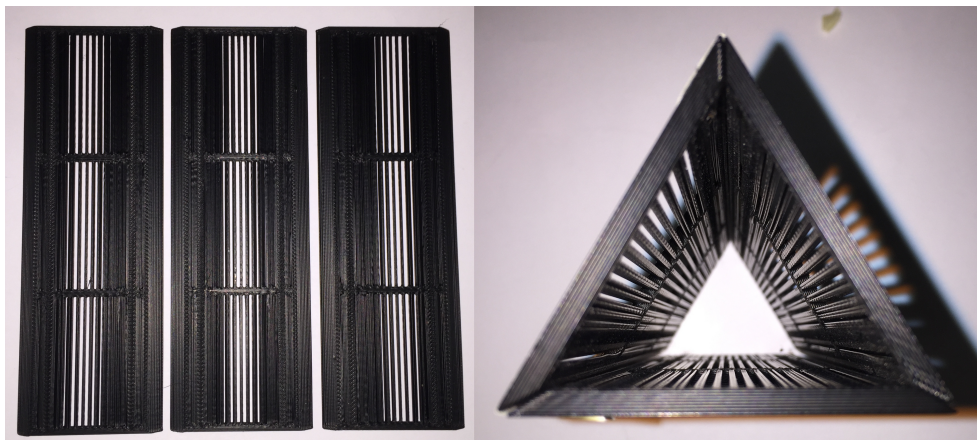


Figure 6.7: Printed cathode in conductive PLA, from the OpenSCAD model shown in Figure 6.5.

focused around a system of cathode strips, which varied in thickness depending on the distance from the anode wire, with the calculations taking into account the desired electric field shape and the inverse square law of the radial electric field that would be produced. Each cathode was designed to fit inside the same enclosure as used in Detector V3, as this minimum anode-cathode distance proved to work exceptionally well. Initial attempts at printing showed the previous method of cathode printing, i.e. printing the cathodes with the axis vertical, was no longer possible due to the fine vertical structures requiring the brief deposition of a small quantity of thermoplastic, which would rarely print successfully.

Instead, the triangular cathode structure was divided into the 3, equal sides to be printed horizontally, as seen in Figure 6.5. The 3 separate pieces are then joined together in the detector at the same point as the previous cathodes were introduced. This method was also a solution to a growing concern, in that currently all the printed triangular detector have been printed pointing downwards, allowing for easier insertion of the printed TC cathode. Obviously, half the tessellating triangle will be pointing up and this current method of cathode insertion will be impossible. Combining 3 separate sides of a triangle within a converging, printing triangle is much easier (with a few additional measures).

While this method of printing the cathodes did improve the accuracy of the prints, some issues were still found due to the same limitation of the conductive filament that have been previously discussed, namely, poor line-line, layer-layer fusion. Some designs also focused around having very fine strips of conductive filament,



Figure 6.8: Picture of the completed Detector V4; containing a graded cathode. The cross-section of the cathode is marked on the detector for identification purposes.

which failed to print successfully. A design that exhibited both these printing issues is shown in Figure 6.6.

The first successfully printed cathode structure can be seen in Figure 6.7 and uses the design shown in Figure 6.5. The cathode was designed to be thicker than is required, to ensure successful print, with the aim to reduce this later. The minimum, reliably printable thickness determined the thickness of the central strip, with the thickness of the remaining strips based around this value. The cathode was designed such that the cross-section of each strip is an obtuse trapezoid, with the lateral sides calculated to be normal to the surface of the anode wire. This can be seen in both the OpenSCAD model and printed design from the different angles used for the images.

With the cathode printed successfully, the same enclosure design as Detector V3 was used, meaning the same wire frame could be utilised once more - the original purpose of the design was based around reusability. As the same method to produce Detector V3 was being repeated, the same, edited gcode file could also be reused. The cathode was, as before, introduced before the first enclosure ceiling layer, however, in this case, some time was taken to manually thermally fuse the 3 sides of the cathode together. Once again, a thin wire was fused to the top of the cathode and secured on the wire frame before printing recommenced.

The detector construction continued using the previous method, and the same two circuits were included to better supply higher, filtered bias voltage to the detector. The completed detector, Detector V4, can be seen in Figure 6.8.

The same experimental setup used for the previous detectors was adopted once again to take data, i.e. the same equipment and drift gas. The lowest flow rate, of 0.035 l/min, was used and the oxygen level in the detector was maintained at < 100 ppm. The strontium-90 source was, once again, used to supply a higher flux of charged particles.

The range of applied bias voltages tested over was 1100 – 2700 V. The maximum bias voltage was determined by the point at which continuous discharge began to occur in the detector, indicated by uncharacteristically shaped, frequent signals being observed. The lowest bias voltage was determined using the observed, apparent detection rates; time restriction meant lower bias voltages could not be tested.

A slight difference did occur in the experimental setup for testing Detector V4, as the initial attempt to characterise the detector at high bias voltages resulted in some components of the Tennelec TC 174 Preamp being rendered useless, leaving

the preamp inoperable. Replacing these components resulted in amplified signals with a much lower baseline noise level.

6.2.2 Detector V4: Results

As has been used before, the average maximum pulse heights and rates for each applied bias voltage was used to determine whether correct operation was occurring within the detector. These are shown in Figure 6.9 and Figure 6.10, respectively. By first considering the pulse height data, and comparing to Figure 2.1, Detector V4 clearly exhibits the first 3 operational regions, with the initial recombination region shown 1100 – 1400 V, the ionisation region in the 1400 – 1900 V range and a large proportional region from 1900 V to 2400 V. These region are succeeded by a slight decrease in pulse heights, most likely due to the increased positive-ion shielding associated with the large breakdown that occurs for operation within the Geiger-Müller region; reducing the effective bias voltage within the detector.

Given that the cathode in Detector V4 was designed to produce an electric field similar to the cylindrical cathode in Detector V3, the pulse height data from both V3 and V4 are remarkably similar, giving some evidence that the graded, triangular cathode is operating as expected to produce a uniform avalanche close to the anode wire.

A noteworthy feature of the pulse height data is the large proportional region associated with this detector. As aforementioned, these tessellating, triangular tubes will be operated in the proportional region to maximise the ability to measure different muon path lengths. A large proportional region is therefore desirable given the proposed tracking function.

By looking at the rate data shown in Figure 6.10, the graph shows the general expected shape, increasing with applied bias voltage before, generally, plateauing. While the increase in rate is expected to occur solely in the recombination region, the increasing rate extends past this into the ionisation region; the reason for has, unfortunately, not been determined. The rate shown for the higher bias voltages exhibit large error bars, this is likely due to the same phenomenon causing the decrease in pulse heights over the same bias voltages; breakdowns resulting in longer dead-times.

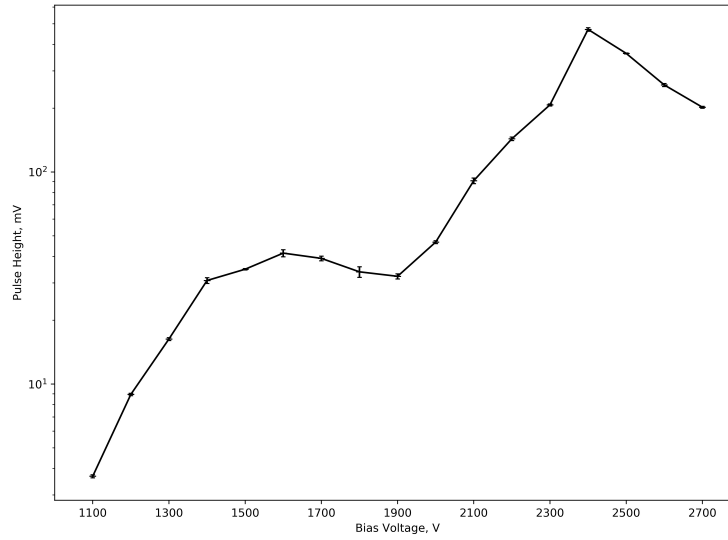


Figure 6.9: Graph of average maximum measured pulse heights plotted against applied bias voltage for Detector V4. The maximum electric field, in V/cm, can be found by multiplying the bias voltages by 35.54 cm^{-1} .

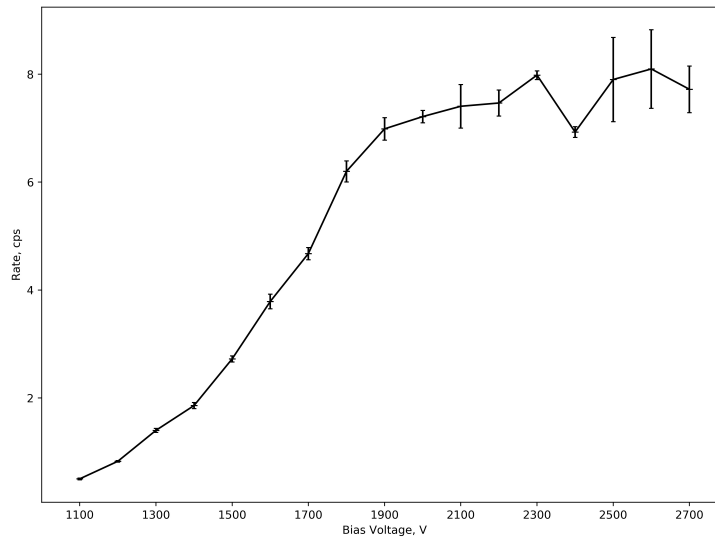


Figure 6.10: Graph of average event rate plotted against applied bias voltage for Detector V4. The maximum electric field, in V/cm, can be found by multiplying the bias voltages by 35.54 cm^{-1} .

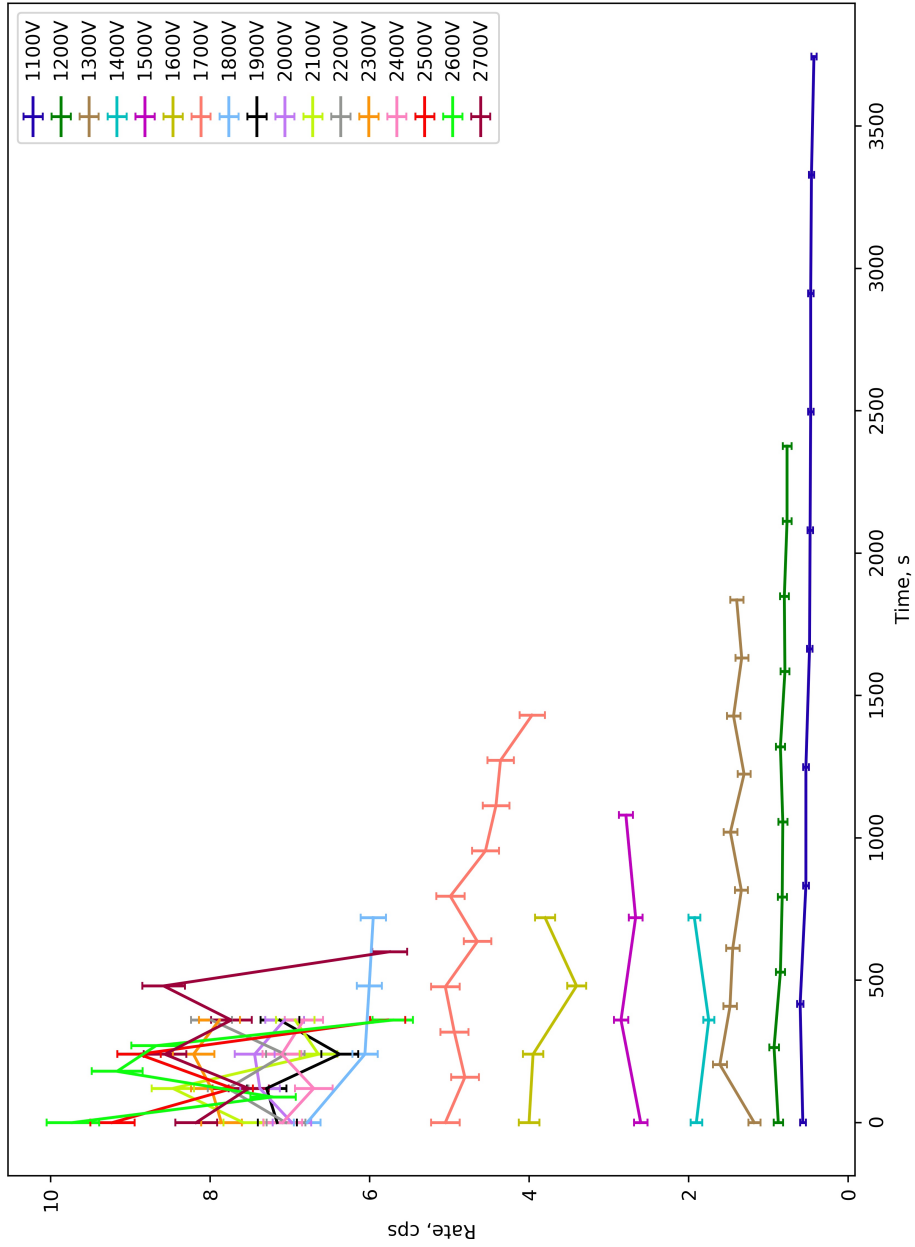


Figure 6.11: Graph showing the change in average event rate over time of operation for Detector V4. As before, the maximum electric field, in V/cm, can be found by multiplying the bias voltages by 35.54 cm^{-1} .

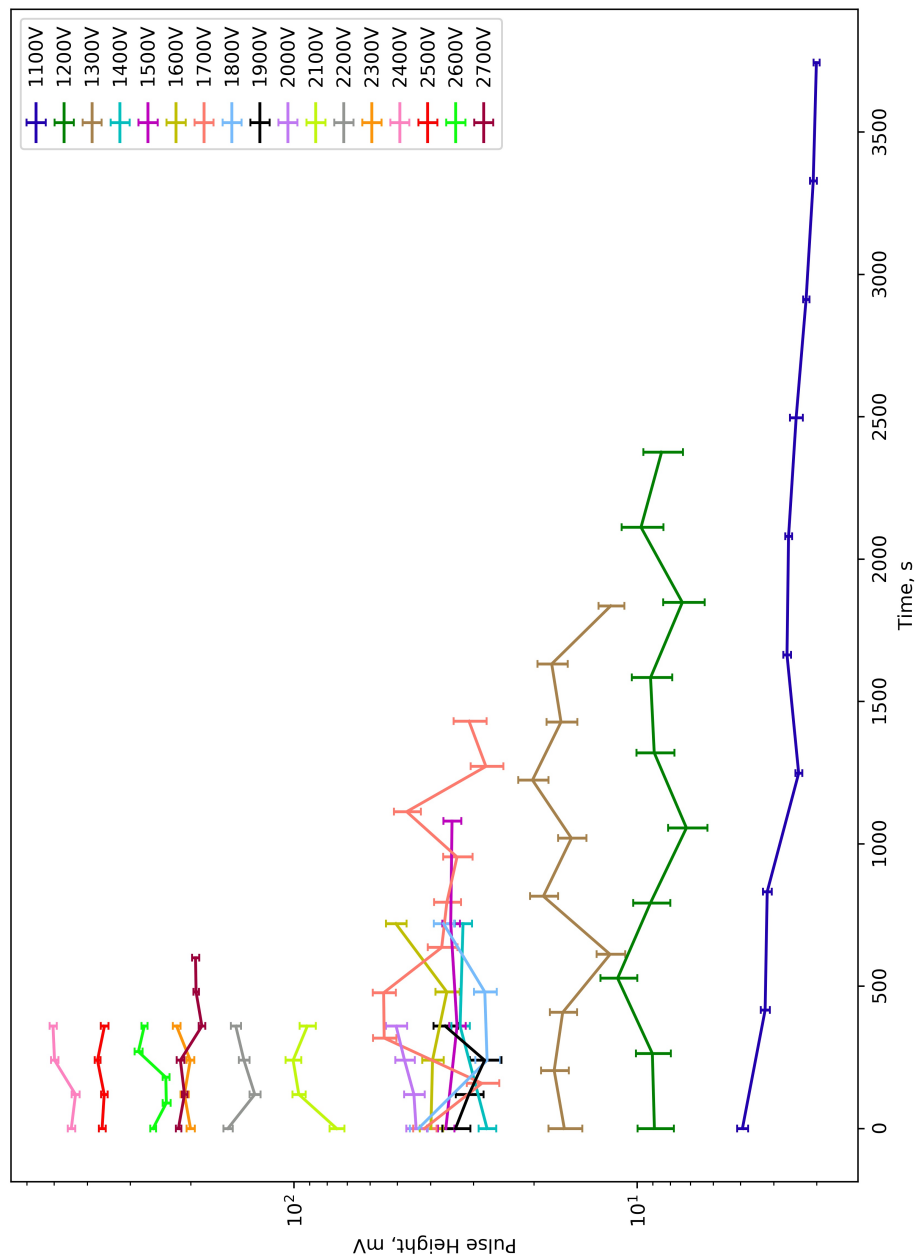


Figure 6.12: Graph of average maximum pulse heights plotted against applied bias voltage for Detector V4. Again, the maximum electric field, in V/cm, can be found by multiplying the bias voltages by 35.54 cm^{-1} .

Detector Stability

Once again, stability plots have been created to investigate whether the rate and pulse heights, for each applied bias voltage, change significantly over the runtime; an indication of space-charge build-up and other operational issues. The rate stability graph in Figure 6.11 shows that general stability occurs over the lower applied bias voltages, however, some decrease in rate over time is observed for 1700 V. A similar decrease is observed during the initial operation at 1800 V, although this does plateau which has been observed in previous detectors and explained due to some time taken for stable operation to occur. Unfortunately, lower runtimes occurred for higher bias voltages, due to the higher detection rates, and thus these decreases cannot be fully investigated further at the higher bias voltages, although it is predicted that space charge buildup would occur less at these higher bias voltages due to the increased electric field. A significant variability is exhibited while operating at bias voltages corresponding to the Geiger-Müller region which, as mentioned previously, is likely due to the breakdown causing large dead-times.

The stability plots for the measured pulse heights are shown in Figure 6.12. The graph shows general stability throughout operation at most bias voltages, although some variability is seen while operating at the lower bias voltages. A clear exception is seen at the lowest bias voltage, 1100 V, whereby a constant decrease in pulse height is observed throughout the operational runtime, likely due to a decrease in effective bias voltage from space charge build-up occurring without a significant electric field to remove positive ions. A corresponding decrease in the rate stability graph would be expected, but given the gradient of the pulse height and rate data for 1100 V, shown in Figure 6.9 and Figure 6.10, respectively, it is clear that a change in effective bias voltage would result in a significantly greater change in the pulse height rather than rate, over time.

6.3 Initial Tracking Tests

As the triangular detector, complete with graded cathode, had been successfully 3D printed, operated and characterised, the next stage of testing regarded an investigation into whether muon track lengths could be determined via pulse height information. In this experiment, a muon telescope was constructed and used in coincidence with detector V4 to measure muon signals from within a finite range of

path lengths, with the aim to compare average signal heights produced from a range of possible path lengths.

Two 18 mm × 18 mm × 250 mm scintillating bars were cut, polished and coated in black out material to create the muon telescope; the scintillator used was the EJ-200 from Eljen Technology. A Silicon PhotoMultiplier (SiPM) was then attached to each bar, with the use of Saint Gobain Crystals BC-630 Optical Coupling Grease for better optical continuity; the SiPMs were connected to bespoke signal amplifier boards. These bars were clamped 415 mm apart to form a muon telescope, as depicted in Figure 6.13. Detector V4 was clamped between the two bars, 100 mm from the bottom bar and 250 mm from the top bar.

As mentioned, V4 was required to be operated in the proportional region to ensure significant signal amplification would occur, therefore, a bias voltage of 2200 V was selected as a compromise between pulse height and rate stability. 2200 V is a bias voltage close to the centre of the proportional region range and showed little variability in pulse height and rate over time although, admittedly, the rate justification comes from observations in a rather small timeframe. While the bias voltage remained constant for this experiment, the remaining setup for Detector V4 remained the same as that used during characterisation.

The signals from the scintillating bars were passed through a CAEN N417 discriminator unit and relatively large thresholds set, such that only muons passing through the majority of both bars are selected, putting a greater constraint on the accepted muon paths. These discriminated signals were then passed through a CAEN N455 coincidence unit and the output used as a trigger to look for signals from Detector V4 on the LeCroy WaveRunner 6100 oscilloscope. The trigger looked for V4 signals $\sim 10 \mu\text{s}$ after the muon telescope as the signals from Detector V4

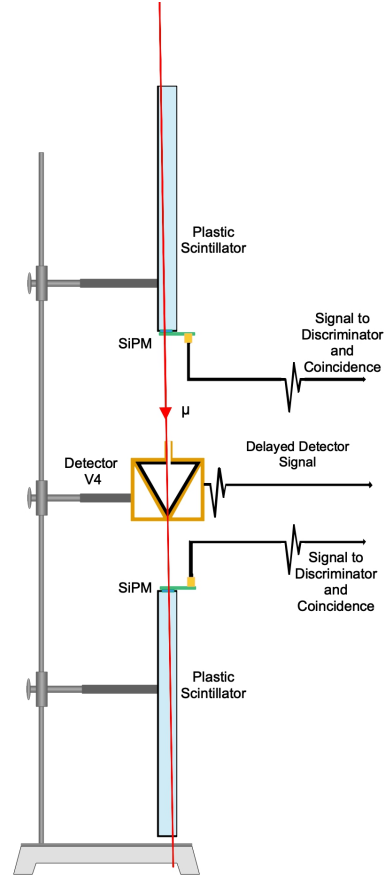


Figure 6.13: Experimental setup of the muon tracking experiment.

arrived a significant time after the coincidence signal, due to the required drift time of the ionisation electrons and the additional amplifier electronics required. The muon telescope coincidences were also counted for an efficiency calculation. Unfortunately, setting up a muon telescope to accept such a narrow range of paths lengths resulted in a low coincidence rate of ~ 0.005 cps which, due to time constraints on the project, meant only two different path lengths could be investigated.

6.3.1 Tracker Test: Results

Detector V4 was rotated about the clamped position to create two average muon path lengths of 14.5 mm and 36 mm through the detector, yielding a path length ratio of ≈ 2.48 . 250 events were recorded for both path lengths and the pulse heights recorded before being subjected to the same signal selection algorithm and curve fitting as has been used throughout the testing of all previous detectors. From the number of successful signals recorded, the detection efficiency of Detector V4 was found to be $78.6 \pm 5.0\%$.

The average pulse height for each of the investigated path lengths were calculated and found to be 44.1 ± 14.6 mV and 95.7 ± 22.1 mV, respectively, with a signal height ratio of $\approx 2.17 \pm 0.88$. Whilst the errors on these measurements are relatively large, and only 2 data points have been acquired, the ratio of the averaged signal heights is within 1 standard deviation of the average path length ratio, yielding a promising result for the detector design and concept and giving justification for development to continue.

6.4 Chapter Summary

The 3D printing of another SWGD, Detector V4, was accomplished using the developed method, described throughout the previous work chapters of this thesis. The detector contained a triangular cathode structure which was printed as 3 identical inserts and then assembled within the detector during printing. The design of each insert was created in an attempt to mimic a cylindrical field within the triangular volume; a symmetrical, radial field is required for consistent avalanche to occur near the anode wire.

The detector was operated over a range of bias voltages to fully characterise the operational regions, as has been done for all previous detectors, with stability plots

created to ensure steady operation can occur and that space-charge build-up is not an issue with the cathode design. The main operational regions of Detector V4 were identified with a significantly large proportional region found, which is desirable for the proposed purpose. The detector was also found to be stable over most bias voltages with exceptions at the lowest bias voltages and throughout operation in the Geiger-Müller region, which is expected.

With Detector V4 successfully characterised, an initial investigation into determining muon path length through the detector, via measured pulse height, was performed using a coincidence method between the detector and a muon telescope constructed from two, thin scintillating bars. While only two data points were found due to time constraints, and thus no sufficient conclusion can be made towards the use of tessellating, triangular tubes as a means of muon tracking, the results found so far bode well for the detector concept and the project remains an exciting area for future development. Future experiments, using a muon trigger, could improve the tracking capability further by utilising the timing measurements also.



Figure 6.14: Picture of three different, untested detectors, each containing a new variation of the graded cathode.

Chapter 7

Thermoplastic Scintillator Filament and Other Additional Gaseous Detectors

The main body of work discussed in this thesis has revolved around the research and design project of 3D printing Gaseous Detectors (GDs), specifically, wired GDs. While this was the main scope of the PhD, alternative uses for Additive Manufacturing (AM) in HEPP instrumentation were also investigated. This chapter will discuss the progress made in these areas.

7.1 Thermoplastic Scintillator Filament

The method of 3D printing novel Single Wire Gaseous Detectors (SWGDS), discussed in the previous chapters of this thesis, was developed with the intention of creating a customisable single-print, muon tracker. As the limitations of FDM, and the associated thermoplastics, became evident, i.e. the inability to print conductive PLA and normal PLA together, the benefits of a dual extruder printer weren't being fully utilised.

Gaseous detector systems, especially used for Cosmic Ray Muon (CRM) tracking, typically use a scintillator trigger panel to initiate the used data acquisition and would be required for the aforementioned detector design. With the range of printable thermoplastics continually expanding, filaments made from Poly(methyl methacrylate) PMMA and High Impact Polystyrene (HIPS) have been developed;

both PMMA and Polystyrene (PS) being plastic scintillator bases. While PMMA does not scintillate, it is a base for scintillators such as anthracene.

By adding the appropriate fluorescent dyes (fluors) to these thermoplastic scintillator bases, a 3D printable, scintillating filament could be produced. This scintillating filament could then be incorporated onto the printed muon tracker, utilising the dual extruders, and creating a complete system in a single print; cathode prints excluded. A photodetector would be added post-print to detect the scintillation light.

Solid, transparent models have already been printed using transparent ABS filament [47], as mentioned in Subsection 1.2.1. While a different thermoplastic was used, this proves the concept is possible and the development of transparent, scintillating filament commenced. Not only would the development of this printable scintillator be beneficial for printed detector system, Additive Manufacturing also has the advantage of being able to produce designs that are difficult or impossible to create while using conventional fabrication methods, in this case, for example, injection moulding.

The applications of the technology are vast, from being able to print new, interesting scintillator geometries for increased light collection; to creating application specific designs, such as a lightweight and flexible plastic scintillator mesh which could be worn by law enforcement officers as mobile radiation detectors.

7.1.1 Initial Developmental Stages

As mentioned, both PMMA and HIPS have been turned into printable filament and so these thermoplastics were the focus of the research. The initial plan for the development of printable scintillator revolved around acquiring transparent PMMA and transparent HIPS; developing a method of printing transparent models using these filaments; and adding fluors/scintillator to the thermoplastics to create the desired plastic scintillator.

Research into commercially available PMMA and HIPS yielded two initial hurdles to overcome; transparent HIPS does not exist and only one company distributes transparent PMMA compatible with the Gigabot printer.

Printable Poly(Methyl Methacrylate)

As transparent PMMA was commercially available, this was the first thermoplastic to be investigated further. Results of transparent models, printed in PMMA, are not well-documented, however, the difficulty in achieving such prints is well-known.

With the PMMA acquired, developing a method of creating transparent prints commenced, but with little success. The investigation varied most print settings, such as print temperature, layer height, infill overlap, etc., however, each experimental method yielded highly opaque prints after the initial print layer. The best print achieved is shown in Figure 7.1. Post-print processing, i.e. acetone polishing, would yield a more transparent final print, however, this additional step is not ideal with regards to the final application and poor optical clarity between layers would still be an issue.

Development of a PMMA-based plastic scintillator was ended at this point. Not only did the thermoplastic yield opaque results, but the material is extremely difficult to work with, often separating from the print bed mid-print, failing to complete the printed model. There was also awareness of a significant issue with regards to the next stage, if a transparent PMMA model could be developed; the introduction of scintillator.

As mentioned, PMMA is a plastic base and does not scintillate. This means PMMA requires the addition of a scintillator to be incorporated into the polymer matrix. Such scintillators can pose significant risks which would intensify when heated. Anthracene, for example, has a low flash point of 121°C, which is significantly below the required print temperature of PMMA and, upon heating, decomposes to produce acrid, toxic fumes which increase the risk of fire and explosion. These risks were previously known but the investigation continued as a means of determining the viability of using the PMMA base with possibly safer scintillators.

Printable Polystyrene

As PMMA posed significant issues, and transparent HIPS is not available, alternative strategy was taken. Existing polystyrene (PS) scintillator pellets were used to create crude, printable filament pieces. These PS pellets had been developed for a previous project, to produce injection-moulded plastic scintillator and contained the fluors: 0.04 wt%¹ 1,4-bis(5-phenyloxazol-2-yl) benzene (POPOP) and 1.5 wt%

¹Percentage by weight



Figure 7.1: Picture of the best transparent PMMA print. The increase in transparency for a single layer print can be seen on the corner tabs (added for easier removal from the print bed).

p-Terphenyl. The filaments ranged in length from $\sim 30 - 60$ cm, but varied significantly in diameter; the production method was not created to produce such uniform filaments.

The filament diameter required for use with Gigabot can range between 2.75 – 3.00 mm, however, each filament used must be relatively uniform for consistent printing, with typical tolerances of $\pm 3.5\%$ accepted. Unfortunately, the current method used to produce filaments varied, in some cases, by $> 100\%$. Some of the more uniform filaments are shown in Figure 7.2.

The created filaments also posed significant issues with linearity, in that the filaments were not perfectly straight. This is not a significant problem with most thermoplastic filaments, which are supplied in spools for printing. This was not possible with PS filaments as the material is inflexible, brittle and glassy. Despite these issues, some preliminary prints were attempted and extrusion was achieved. Unfortunately, the irregularity in the filament diameter caused non-uniform extrusion and reliably printing models was not possible.

As the PS pellets were available, an alternative method of producing uniform filaments was adopted, i.e. using the Filastruder [93], shown in Figure 7.3. The Filastruder is a filament extruder which accepts thermoplastic pellets (and additives)

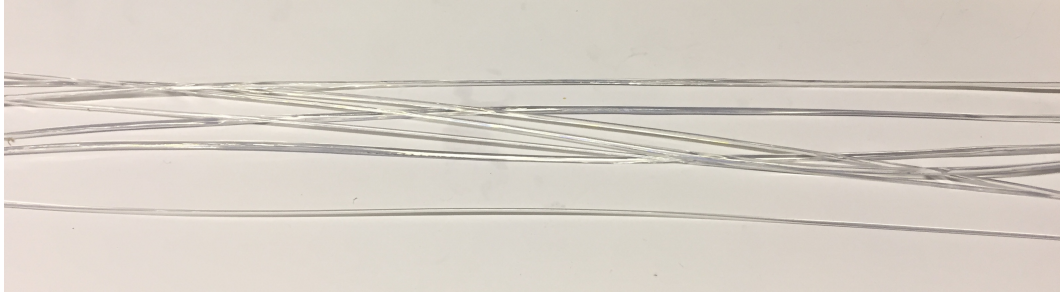


Figure 7.2: Picture of the initial PS scintillator thermoplastic filaments.

to produce customisable filaments; a very desirable piece of equipment to develop new composite thermoplastics.

Using the Filastruder did yield uniform, thermoplastic filaments, however, contamination posed a significant complication, mainly originating from the Filastruder itself. The Filastruder did undergo some modifications in an attempt to eliminate this issue but, unfortunately, was done so without success.

Despite the uniformity issues of the original PS filaments, some small sample prints were created but many initial problems were found. All sample prints were fibrous and opaque, with poor optical clarity achieved between the layers. This was due to poor line-line, and layer-layer, thermal fusion occurring; the cause of which was determined to be from the high glass transition temperature of the PS, which turned glassy too quickly post-extrusion for adequate fusion. The brittle nature of the PS scintillator often resulted in the filament breaking inside the extruder, which then could no longer print and solidified. This rendered the Gigabot unusable, requiring a significant amount of downtime to fix. The PS filament also required significantly higher printing temperatures, causing concern for the thermal degrading of the added fluors. The short filament lengths also meant, even if prints could occur, only small models could be achieved.

Given the initial issues found with the PS scintillating filaments, development shifted towards creating a more flexible, less brittle filament that would print at lower temperatures, have a lower glass-transition temperature, and could be produced in longer filament lengths.

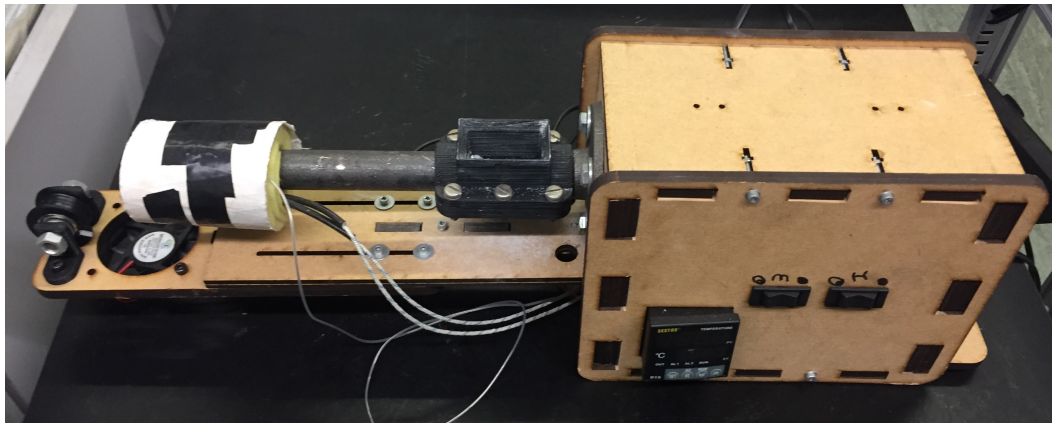


Figure 7.3: Picture of the Filastruder used to create uniform PS filament.

7.1.2 Flexible Plastic Scintillator

Through collaboration with the Polymer Physics group at The University of Sheffield, it was determined that the best strategy to create a more flexible PS filament, with a lower melting point and glass-transition temperature, would be to incorporate a plasticiser into the scintillator mixture. Plasticisers are additives used to increase flexibility and reduce brittleness in plastics, with evidence already existing that these additives can reduce the glass-transition temperature of PS [94][95].

Diocetylphenyl phosphonate (DOPP) is a common, relatively cheap plasticiser and so was selected as an appropriate plasticiser to use for the development of the flexible plastic scintillator, although the use of DOPP with PS is not well-documented. It was assumed the used of DOPP would decrease the scintillator performance, as the composition is altered, and so the first test would be to vary the amount of DOPP used and assess the effects on both the scintillator performance as well as the mechanical and thermal properties.

The ideal outcome would be to achieve a scintillating thermoplastic with the required thermal and mechanical properties for printing, while minimising the effect on scintillator performance. Before this test could be performed, the different samples needed be produced; incorporating the DOPP into the PS scintillator is not a trivial task and so methods for creating and processing the resultant flexible scintillator were required.

As the samples would need to be compared against unaltered PS scintillator

(original), the aim was to produce scintillating disc samples of diameter 20 mm and height 5 mm. The diameter was selected to cover a significant portion of the active area of the Photomultiplier Tube (PMT) which would be used. The thickness was selected as this is the thickness of the plastic scintillator tiles moulded from the same PS scintillating pellets.

At first, the already existing PS scintillator was dissolved into an appropriate solvent, Tetrahydrofuran (THF), and varying percentages of DOPP were added: 40 wt%, 20 wt%, and 10 wt%. These were then cast into appropriate moulds to



Figure 7.4: The flexible PS scintillator sample containing 40 wt% DOPP. The sample has been stretched beyond the moulded shape to better illustrate the excessive viscosity of this particular composition.

produce the desired scintillating discs, and the solvent left to evaporate in a low heat oven. Initial observations ruled out the flexible PS containing 40 wt% DOPP as the resultant material was severely viscid; not appropriate for 3D printing, seen from Figure 7.4.

The remaining samples exhibited a desirable level of flexibility, however, these did contain many bubbles of solvent vapour. This is due to the polymer re-solidifying before all the THF solvent could evaporate, trapping bubbles within the samples. The solution to this issue, unfortunately, negated the use of the aforementioned moulds, as the samples were required to be heated to remove the bubbles. This method resulted in more bubbles to appear as the higher temperature caused previously unevaporated solvent, trapped between polymer chains, to expand within the samples.

A new method was adopted, whereby the samples were hot-pressed into thin sheets to increase the removal of the solvent. The temperature required to hot press the samples, i.e. turn the samples molten, was significantly lower than the temperatures required to print the initial PS scintillating filament, although the actual temperature used cannot be given due to the crude temperature controls of the hot press. The sample containing 20 wt% DOPP became too viscous and tacky to process in this way and so was eliminated as an option.

The method was successful at removing the solvent from the scintillator with

10 wt% DOPP but, despite measures put in place to avoid this, the constant folding and hot pressing of the samples caused a great deal of contamination to occur. The sample was able to be cast into the previous mould and was compared against an original scintillator disc (using the experimental method described below). This experiment found the addition of 10 wt% DOPP to the PS scintillator, and the required processing, reduced the light output and detection efficiency of the scintillator by a factor of 2. Unfortunately, this value comes from a severely contaminated sample, and thus a better method of producing the samples was required.

Four new methods were assessed as possibilities which altered:

- (a) the method of solvent extraction to better remove solvent from the sample;
- (b) the solvent used, to see if another solvent would evaporate better;
- (c) PS polymer chain length, to investigate whether a smaller chain length would trap less solvent; and
- (d) casting and evaporating method, to determine whether thinner casting and slower evaporation would yield better samples.

The first method, (a), involved using a vacuum oven to evaporate the solvent from the samples, while heating the samples enough to remain molten, thus allowing the solvent to escape the polymer matrix which would then solidify afterwards. Unfortunately, the temperature and pressure required for this to occur was sufficient enough for the DOPP to also evaporate, resulting in samples of $\sim 100\%$ PS scintillator once more.

The second method, (b), swapped THF for chloroform (CHCl_3) but the same initial issues, concerning trapped solvent in the polymer matrix, occurred. As the boiling point of CHCl_3 is comparable to that of THF, this solvent could not be used with the vacuum oven method for the same reason mentioned.

The third method, (c), investigated the remaking of the PS scintillator from the separate components, where PS polymer, known to have small chains lengths, was mixed with the aforementioned percentages of POPOP and p-Terphenyl, and 10 wt% DOPP. Unfortunately, the resultant samples did not appear to have much affect on solvent evaporation. The use of even smaller chain lengths was investigated, however, initial research revealed that low molecular weight plastic scintillators, i.e. plastic scintillators with small polymer chains, showed significantly lower light

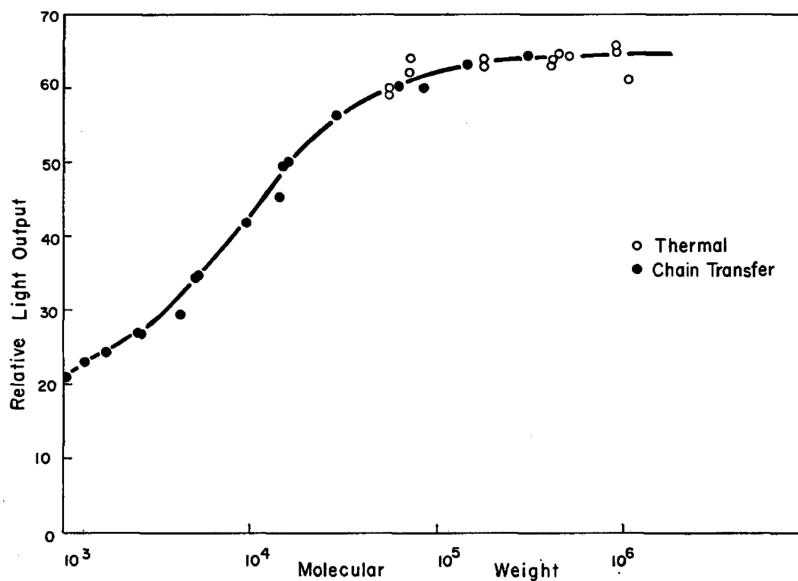


Figure 7.5: The effect of molecular weight, i.e. chain length, on relative light output of plastic scintillator. The two different datasets refer to methods of controlling chain length [96].

output than plastic scintillators of a higher molecular weight, as shown in Figure 7.5 which shows relative light output² as a function of plastic scintillator molecular weight [96].

The final method, (d) involved a simpler, yet more time consuming method, whereby the same initial steps were taken but the solutions were cast into a larger mould and left to slowly evaporate without the use of the oven. This produced ~ 1 mm thick samples containing no bubbles, indicating this method was by far the best out of those tested. As, from the initial samples, 20 wt% DOPP was found to become too viscous when heated, 4 samples were created by adding: 15 wt%, 10 wt%, 5 wt% and 0 wt%; the final sample was created to investigate if the processing method also had an effect on the scintillator, rather than the DOPP. Two of the samples can be seen in Figure 7.6.

With a desired sample thickness of 5 mm for testing, the scintillator could be melted and recast into the previous mould or cut into discs and stacked; for time efficiency the latter option was chosen, with 5 layers of each scintillator assembled

²Relative to a plastic scintillator standard using a Cs¹³⁷ source with a conventional scintillation counter assembly. The assembly consisted of a Dumont 6292 PMT, a cathode follower, a linear amplifier, a differential discriminator and scaler.

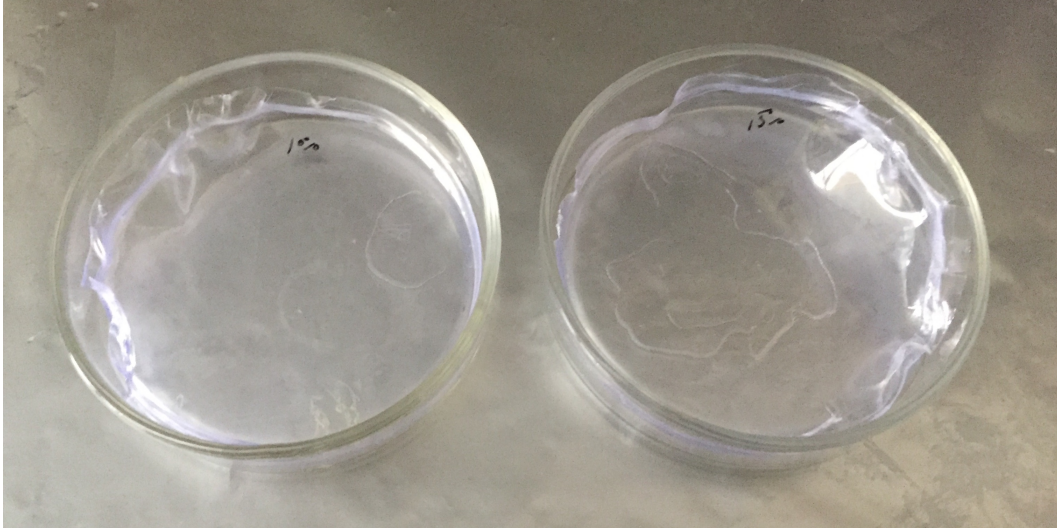


Figure 7.6: Two scintillator samples containing 10 wt% (*Left*) and 15 wt% (*Right*) DOPP. Scintillation can be seen occurring in both samples. The areas which appear to be large bubbles are in fact where the sample has adhered more to the glass dish.

into the required cylindrical shape, coupled together with Saint Gobain Crystals BC-630 Optical Coupling Grease to ensure better optical continuity within the sample. This process did reveal that the 5 wt% DOPP sample was still extremely brittle, as was the 0 wt% which was expected.

Data and Results

With the samples ready, comparison against the original scintillator could commence. Each of the 4 samples were individually coupled to the active surface of a ET-Enterprise 9902B Series PMT using the aforementioned optical coupling grease, and a strontium-90 source was used to provide β -particles for detection. This same experimental setup was also used for a disc of original scintillator, cut from a tile, and a 5 mm thick opaque plastic sample; the strontium-90 source was still used to ensure signals from any β -particles incident on the PMT would be accounted for in the scintillator data. The lowest threshold possible, above dark current, was used for all samples.

10,000 signals were recorded for each of the the samples, with the light output of each event measured. The measured rates and light output, relative to the original scintillator, for each of the samples are shown in Figure 7.7 and Figure 7.8, respect-

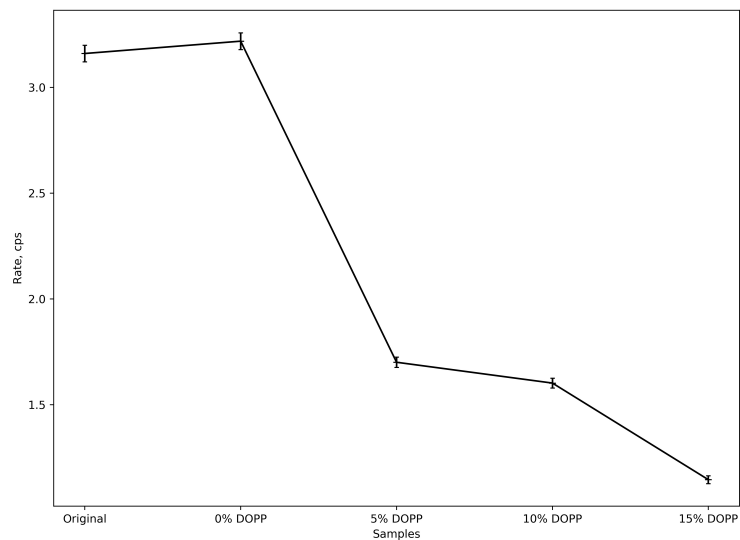


Figure 7.7: Graph of the detection rates for each sample of the scintillator samples, corrected for non-scintillator signals.

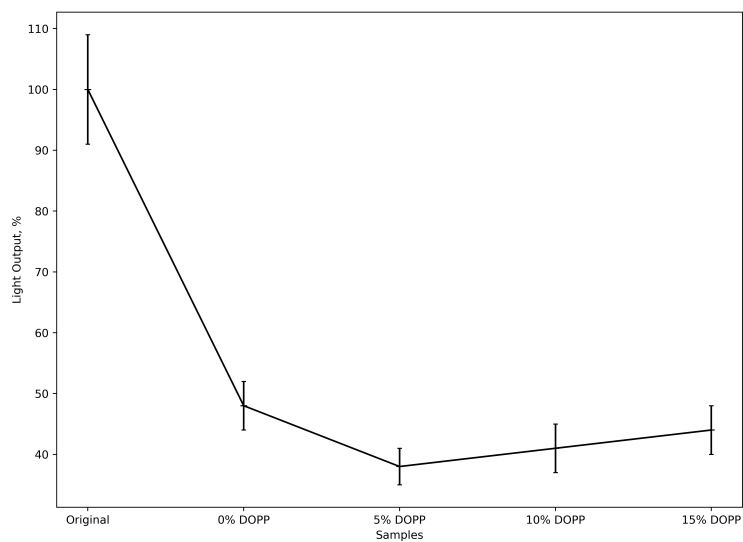


Figure 7.8: Graph of the relative light output for each sample of the scintillator samples, corrected for non-scintillator signals. The values are relative to the original sample.

ively. The data for the opaque sample was used to account for non-scintillation signals in the data shown.

The rate data indicates that processing the scintillator does not effect the detection efficiency, with significantly similar rates shown between the original scintillator and the processed scintillator with no DOPP added. The addition of DOPP does affect the rate, with the more DOPP added, the lower the detection rate.

The light output data indicated the processing method does drastically reduce the light output of the scintillator by a factor of 2, although the stacking of the thin scintillator discs could have an effect. Comparing only the processed scintillator, the inclusion of DOPP does not appear to affect the light output, with no significant difference between the processed sample containing 0 wt% DOPP and those containing DOPP.

7.1.3 Flexible Scintillator Summary

Two different plastic scintillator bases, PMMA and PS, were assessed as materials to produce a scintillating thermoplastic filament. PMMA was ruled out due to the difficulties with producing optically transparent prints and the issues that would come along with incorporating a scintillator into the printable material.

PS became the focus of the printable scintillator, however, some of the material properties required altering for better printing to occur, i.e. lower melting point, lower glass transition, greater flexibility and less brittle. Through collaboration with Polymer Physics Group at The University of Sheffield, it was determined that adding the plasticiser, DOPP, to the scintillator composition would result in the required property changes.

Many methods of introducing DOPP into the scintillator composition were investigated, with the most successful method used to produce flexible scintillating samples. Initial tests on these samples indicate that DOPP does cause a significant affect on the detection rate of the scintillator, whilst the method of introducing the DOPP appears to severely affect the light output of the scintillator, indicating a better method of creating a flexible scintillator is still required.

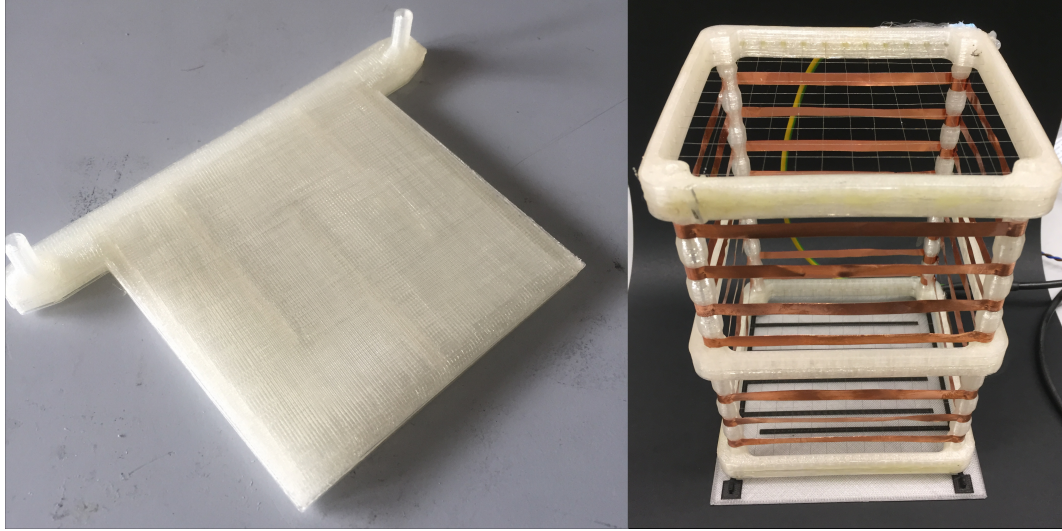


Figure 7.9: Picture of the 3D printed RPC design (*Left*) and the partially 3D printed TPC (*Right*).

7.2 Time Projection Chambers, Readout Strips and Resistive Plate Chambers

The initial work with the conductive filament was done so as to produce internal cathodes for the 3D printed Single Wire Gaseous Detectors (SWGDs). While the developments made in this area have already been discussed, another use was investigated; 3D Printed Readout Strips.

As incorporating conductive filament inside normal PLA was proven to be unreliable and unsatisfactory, producing separate conductive elements or printing conductive filament onto normal PLA was achieved with great success, after being constantly developed throughout this PhD; the most successful version of the readout strips can be seen in Figure 5.5 (*Left*).

While developing a process of 3D printing readout strips was done successfully, allowing for novel readout patterns to be investigated, a means of testing any readout strips was not available; this led to the development of 3D printed Resistive Plate Chambers (RPCs) and a Time Projection Chambers (TPCs).

Unfortunately, work in this area has been limited. The RPCs require a level of gas-tightness much greater than that of the SWGD enclosures discussed throughout this thesis. This is due to the thinner enclosure walls required for optimal RPC function. While a simple design has been created and successfully printed, as seen

in Figure 7.9 (*Left*), the development of new FDM techniques have been required to go beyond the current limitations of the AM process.

A partially 3D printed TPC was determined to be a more promising method of testing readout strips, as it could be placed into a gas-filled environment to be operated. The TPC was developed via the Rapid Prototyping method and the final version is shown in Figure 7.9 (*Right*). Unfortunately, data is still yet to be taken with this setup and further work in this area remains of great interest.

Chapter 8

Concluding Remarks

In recent years, Additive Manufacturing (AM), or 3D printing, technologies have developed sufficiently to be considered as viable fabrication methods for functioning devices, beyond the capability of merely producing prototype models, which had been the main use for the technology. With the rising demand for cheap, numerous particle detectors, AM has been investigated as a production method, with possibilities of novel detector designs, which are typically difficult to produce, emerging from the use of the technology. Fused Deposition Modelling (FDM) was the AM technology available for the project.

With Single Wire Gaseous Detectors (SWGDs) assessed as the simplest and most viable detector to re-create, the first task involved 3D printing gas-tight, hollow enclosures that would sufficiently hold an anode wire at the required tension for correct operation; one of the key components of the detector. Chapter 3 investigated multiple FDM printers, thermoplastics, enclosure designs and print settings to develop a reproducible, printable SWGD enclosure capable of holding and maintaining the drift gas composition necessary for optimal function, while gripping a central anode wire at high tension.

The Makerbot Replicator 2X - Experimental Printer, and the Gigabot GB3 from re:3D, were both tested as possible FDM printers suitable for the project, with severe limitations observed through the work carried out on the Makerbot and the required, associated software. The Gigabot was proven to have the most desirable features for the project, however, most large scale, open-source printers could reproduce the work discussed in this thesis, given the appropriate side-fans are present to generate horizontal overhangs, and the optimal settings given in this thesis are used

as guidelines; these values are expected to slightly vary between machines and slicing software.

While Polylactic Acid (PLA) was found to be the best thermoplastic available, additives which are often included in the thermoplastic composition were found to have significant effects on the printed result. Additives such as stabilisers and antistatic agents can result in smooth, glossy thermoplastics incapable of gripping a thin anode wire, unless excessive material is used. Thermoplastics with significant amount of these additives should be avoided.

Gamma spectrometry was also performed on differently coloured PLA to deduce the effect pigments and dyes can have on the radioactive isotopic content of the detector material used. The investigation showed that these additives can cause a significant increase in the radioactive isotopes present in the final SWGD enclosures. Further investigation into the possibility of 3D printing parts for ultra-low background experiments is already set to continue.

The work done on enclosure design was done so to find a reproducible, hollow design which would eventually be able to contain a cathode, however, many different enclosure designs could be possible and this still remains an area for further development.

The print settings for gas-tight enclosures, whilst minimising the materials used, were found to be using 3 continuous walls, 50% infill, 4 top and bottom layers and 25% infill-wall overlap. Models with wall thicknesses of 4 mm also produced the best results out of those tested. These settings could be further refined to increase the level of gas-tightness, however, given the level of gas-tightness achieved, this was not required. While the above settings worked sufficiently, these should only be used as guidelines when attempting to reproduce these results on different printers using different slicing software, as these are expected to deviate slightly.

A technique of printing an enclosure around an anode wire was developed by using variable wall thicknesses and creating a multi-gcode method of printing. This method was also used to increase gas inlet integrity but the fragility of these components is still an issue that surround the printed detectors; the breaking of the gas inlets can render the detector unusable.

The available methods of fabricating internal cathodes were assessed, with some attempted. FDM with conductive PLA was the most viable, creating insertable cathode structures. These cathode structures were successfully inserted into printed SWGDs, improving detector operation. Chapters 4 and 5 document the stages of

SWGD development, with 3 detectors created and characterised, 2 of which contained cylindrical cathodes.

Chapter 6 documents the work completed on the final printed detector, which includes a novel cathode structure, designed in an effort towards creating a triangular, tessellating muon tracking system. This detector was successfully characterised over a wide range of voltages, with all desired operational regions found and exhibiting a large proportional region, which is desirable for the proposed function. Detector V4 went on to be operated in coincidence with a small-area muon telescope, and biased within the proportional region, to investigate whether signal heights could be used to aid muon path reconstruction. Whilst the low event rate, associated with the required small-area muon telescope, meant only two data points could be obtained within the timeframe of this PhD, the measurements taken yielded promising results for the detector concept, warranting the continued development of the tracker design.

For characterisation of these detectors to occur, a signal selection algorithm was created to analyse large datasets. Each waveform was subjected to selection criteria and a curve fit used to determine the pulse heights of detector signals.

Chapter 7 outlines the initial work done towards creating a printable plastic scintillator, with poly(methyl methacrylate) and polystyrene (PS) both tested as possible scintillator bases. PS was found to be the most appropriate thermoplastic, however, the properties of such a thermoplastic need to be altered before transparent, large volume scintillator can be successfully printed. Plasticiser was added to the scintillator, which did alter the properties of the thermoplastic in the desired manner, however, this additive did reduce the detection rate of the scintillator significantly, although this was expected as the plasticiser would alter the polymer structure. The method of creating this flexible thermoplastic reduced the achievable light output of the scintillator. Further work is needed in this field, requiring a new method of adding plasticiser to scintillator, and more ways of creating a flexible scintillator investigated; possibly using polymer blends.

Work towards 3D printed readout arrays has been performed, although the operation of an appropriate detector to use with these is still required for testing to begin. Some potential solutions have been created, though more work is needed for development to continue; this field could yield some interesting and novel readout patterns.

This project was created to assess the viability of using FDM to produce particle

detectors. While the first 3D printed detectors have been created using the techniques developed, the limitations of the processes have been evident throughout this PhD. A main issue which has not been well-documented in this thesis, yet remains significant, is the maintenance needed to operate large-scale FDM printers and the propensity towards breakage, especially mid-print. While the models, gcode and techniques developed can produce the desired detectors, the success is completely dependent on constant printer performance, which is a major concern.

The proneness of FDM printer breakage is an operational consequence and, largely, difficult to predict. There are many causes for printer breakage, such as the extended periods of heating and frequent heating cycles which degrade vital components; moving drive belts at constant high tension, supplying large stresses to stepper motors; constant removal of models adhered to the heated bed, resulting in bed movement and degradation, etc. These are just a few examples of the associated problems with the FDM process, many of which can result in a range of issues difficult to diagnose, even with the expertise and experience in printer operation and maintenance acquired during this PhD. Throughout this body of work, a conservative estimate would give a cumulative 6 month period of FDM printer downtime, which required diagnostics tests, printer dismantling, complicated cleaning methods developed throughout, and frequent replacements of vital components. Each time, requiring a full recalibration of the system.

Despite the aforementioned issues, it must be remembered that AM is still growing as a technology with 3D printers, superior to those used for this research, having already been created since this work began, and new composite thermoplastics being continually developed to increase the scope of 3D printing. While it has already been outlined that current 3D printers are yet to reach the required performance goals for the fabrication of more complex detectors, given in Table 1.1, the technology was investigated as a means of producing more basic detectors. An updated version of Table 1.1, as of 2020 when this work concluded, is shown in Table 8.1. It has been documented throughout this thesis that the technology can produce SWGDs, but it is the reliability of the fabrication method that needs to be improved before the technology can truly be considered as a viable means of detector production on any significant scale. It could be concluded that the investigation into 3D printing particle detectors has occurred prematurely in the technologies development, with greater success achievable with upcoming generations of FDM printers which will not only meet the minimum required performance goals but are also constructed with

	Capability (2020)	Performance goal
Printing resolution in x-y	$\sim 10 \mu\text{m}$	$\sim 1 \mu\text{m}$
Layer thickness in z	$\sim 0.1 \mu\text{m}$	$\sim 1 \mu\text{m}$
Print speed	50 cm/s	$> 100 \text{ cm/s}$
Materials	Polymer-metal composites	Polymer-metal composites
Object size	$(200 \times 200 \times 150) \text{ cm}^3$	$(200 \times 100 \times 10) \text{ cm}^3$

Table 8.1: An updated version of Table 1.1 for the best capabilities in 2020, taking into account Fused Deposition Modelling and Aerosol Jet Printing techniques. The best values found have been presented, although these are not yet available on the same printer. [97][98][99][100]

better components, less prone to breaking, and come with inbuilt calibration and error detection systems, able to self correct problems mid-print, reducing the rate of fatal occurrences. The availability of AM technologies is increasing constantly and can still offer a lot towards the field of particle detectors, for example, allowing test detectors to be printed for the development of detector electronics; printing smaller, bespoke components for much larger detectors, rather than attempting to print the whole system; or even allowing simple detectors to be fabricated within schools, further increasing access to HEPP instrumentation for students from an earlier time in their education.

Bibliography

- [1] W. C. Röntgen. *Über eine neue Art von Strahlen*. Springer-Verlag, 2013.
- [2] Anonymous. The edison x-ray experiments, apparatus and fluoroscope. *Scientific American*, 74(14):219–219, 1896.
- [3] G. Shiers. Ferdinand braun and the cathode ray tube. *Scientific American*, 230(3):92–101, 1974.
- [4] J. J. Thomson. Xl. cathode rays. *The London, Edinburgh, and Dublin Philosophical Magazine and Journal of Science*, 44(269):293–316, 1897.
- [5] P. Radvanyi and J. Villain. The discovery of radioactivity. *Comptes Rendus Physique*, 18(9-10):544–550, 2017.
- [6] L. Gerward. Paul villard and his discovery of gamma rays. *Physics in perspective*, 1(4):367–383, 1999.
- [7] T. K. Derry and T. I. Williams. *A short history of technology from the earliest times to AD 1900*, volume 231. Courier Corporation, 1960.
- [8] R. G. A. Fricke and K. Schlegel. 100th anniversary of the discovery of cosmic radiation: the role of g unther and tegetmeyer in the development of the necessary instrumentation. *History of Geo-and Space Sciences*, 3(2):151–158, 2012.
- [9] C. Grupen and B. Shwartz. *Particle detectors*, volume 26. Cambridge university press, 2008.
- [10] E. Rutherford and H. Geiger. An electrical method of counting the number of α -particles from radio-active substances. *Proceedings of the Royal Society of London. Series A, Containing Papers of a Mathematical and Physical Character*, 81(546):141–161, 1908.

- [11] F. N. Flakus. Detecting and measuring ionizing radiation- a short history. *IAEA bulletin*, 23(4):31–36, 1982.
- [12] C. T. R. Wilson. On an expansion apparatus for making visible the tracks of ionising particles in gases and some results obtained by its use. *Proceedings of the Royal Society of London. Series A, Containing Papers of a Mathematical and Physical Character*, 87(595):277–292, 1912.
- [13] A. H. Compton. A quantum theory of the scattering of x-rays by light elements. *Physical review*, 21(5):483, 1923.
- [14] C. D. Anderson. The apparent existence of easily deflectable positives. *Science*, 76(1967):238–239, 1932.
- [15] S. H. Neddermeyer and C. D. Anderson. Cosmic-ray particles of intermediate mass. *Physical Review*, 54(1):88, 1938.
- [16] G. D. Rochester and C. C. Butler. Evidence for the existence of new unstable elementary particles. *Nature*, 160(4077):855, 1947.
- [17] W. Bothe. Coincidence method. *Science*, 122(3175):861–863, 1955.
- [18] P. M. S. Blackett and G. P. S. Occhialini. Some photographs of the tracks of penetrating radiation. *Proceedings of the Royal Society of London. Series A, Containing Papers of a Mathematical and Physical Character*, 139(839):699–726, 1933.
- [19] R. L. Sime. Marietta blau: pioneer of photographic nuclear emulsions and particle physics. *Physics in Perspective*, 15(1):3–32, 2013.
- [20] D. A. Glaser. Bubble chamber tracks of penetrating cosmic-ray particles. *Physical Review*, 91(3):762, 1953.
- [21] B. Zipprich. über einen proportionalverstärker zum nachweis einzelner korpuskularteilchen. *Zeitschrift für Physik*, 85(9-10):592–617, 1933.
- [22] J. W. Keuffel. Parallel-plate counters. *Review of Scientific Instruments*, 20(3):202–208, 1949.

- [23] PG. Henning. *Die Ortsbestimmung geladener Teilchen mit Hilfe von Funkenzählern und ihre Anwendung auf die Messung der Vielfach-Streuung von Mesonen in Blei*. PhD thesis, Verlag nicht ermittelbar, 1956.
- [24] G. Danby, J.M. Gaillard, K. Goulios, L.M. Lederman, N. Mistry, M. Schwartz, and J. Steinberger. Observation of high-energy neutrino reactions and the existence of two kinds of neutrinos. *Physical Review Letters*, 9(1):36, 1962.
- [25] H. Friedman. Geiger counter tubes. *Proceedings of the IRE*, 37(7):791–808, 1949.
- [26] G. Charpak, R. Bouclier, T. Bressani, J. Favier, and C. Zupancic. Some read-out systems for proportional multiwire chambers. *Research on Particle Imaging Detectors. Edited by Charpak G. Published by World Scientific Publishing Co. Pte. Ltd., 1995. ISBN# 9789812795878, pp. 100-103*, pages 100–103, 1995.
- [27] A. H. Walenta, J. Heintze, and B. Schürlein. The multiwire drift chamber a new type of proportional wire chamber. *Nuclear Instruments and Methods*, 92(3):373–380, 1971.
- [28] J. N. Marx and D. R. Nygren. The time projection chamber. *Phys. Today*, 31N10:46–53, 1978.
- [29] A. Oed. Properties of micro-strip gas chambers (msgc) and recent developments. *Nuclear Instruments and Methods in Physics Research Section A: Accelerators, Spectrometers, Detectors and Associated Equipment*, 367(1-3):34–40, 1995.
- [30] F. Sauli. Gem: A new concept for electron amplification in gas detectors. *Nuclear Instruments and Methods in Physics Research Section A: Accelerators, Spectrometers, Detectors and Associated Equipment*, 386(2-3):531–534, 1997.
- [31] V. K. Zworykin, G. A. Morton, and L. Malter. The secondary emission multiplier-a new electronic device. *Proceedings of the Institute of Radio Engineers*, 24(3):351–375, 1936.

- [32] H. Iams and B. Salzberg. The secondary emission phototube. *Proceedings of the Institute of Radio Engineers*, 23(1):55–64, 1935.
- [33] B. K. Lubsandorzhev. On the history of photomultiplier tube invention. *Nuclear Instruments and Methods in Physics Research Section A: Accelerators, Spectrometers, Detectors and Associated Equipment*, 567(1):236–238, 2006.
- [34] S. E. Derenzo, M. J. Weber, E. Bourret-Courchesne, and M. K. Klintenberg. The quest for the ideal inorganic scintillator. *Nuclear Instruments and Methods in Physics Research Section A: Accelerators, Spectrometers, Detectors and Associated Equipment*, 505(1-2):111–117, 2003.
- [35] M. Deutsch. Naphthalene counters for beta-ray and gamma-ray. *Nucleonics*, 2(3):58–59, 1948.
- [36] P. R. Bell. The use of anthracene as a scintillation counter. *Physical Review*, 73(11):1405, 1948.
- [37] W. S. Koski and C. O. Thomas. Scintillations produced by α -particles in a series of structurally related organic crystals. *Physical Review*, 76(2):308, 1949.
- [38] J. B. Birks. Scintillations from naphthalene-anthracene crystals. *Proceedings of the Physical Society. Section A*, 63(9):1044, 1950.
- [39] R. C. Sangster and J. W. Irvine Jr. Study of organic scintillators. *The Journal of Chemical Physics*, 24(4):670–715, 1956.
- [40] M. G. Schorr and F. L. Torney. Solid non-crystalline scintillation phosphors. *Physical Review*, 80(3):474, 1950.
- [41] I. Maskery, N. T. Aboulkhair, A. O. Aremu, C. J. Tuck, and I.A. Ashcroft. Compressive failure modes and energy absorption in additively manufactured double gyroid lattices. *Additive Manufacturing*, 16:24–29, 2017.
- [42] H. Fan, J. Fu, X. Li, Y. Pei, X. Li, G. Pei, and Z. Guo. Implantation of customized 3-d printed titanium prosthesis in limb salvage surgery: a case series and review of the literature. *World journal of surgical oncology*, 13(1):308, 2015.

- [43] M. Heilemann, J. Beckmann, D. Konigorski, and C. Emmelmann. Laser metal deposition of bionic aluminum supports: reduction of the energy input for additive manufacturing of a fuselage. *Procedia CIRP*, 74:136–139, 2018.
- [44] M. Hohlmann. Printing out particle detectors with 3d-printers, a potentially transformational advance for hep instrumentation. *arXiv preprint arXiv:1309.0842*, 2013.
- [45] 3d printed electronics - aerosol jet technology. <http://www.optomec.com/printed-electronics/aerosol-jet-technology/>. Accessed: 17 March 2016.
- [46] A. Sidambe. Biocompatibility of advanced manufactured titanium implants? a review. *Materials*, 7(12):8168–8188, 2014.
- [47] Fennec Labs. 3d printing transparent parts using fdm/fff printer. <http://fenneclabs.net/index.php/2018/12/09/3d-printing-transparent-parts-using-fdm-fff-printer/>. Accessed: 11 December 2018.
- [48] Openscad - the programmers solid 3d cad modeller. <http://www.openscad.org/>. Accessed: 19 March 2019.
- [49] Ö. Şahin, I. Tapan, Emin N. Özmutlu, and R. Veenhof. Penning transfer in argon-based gas mixtures. *Journal of Instrumentation*, 5(05):P05002, 2010.
- [50] S. N. Ahmed. *Physics and engineering of radiation detection*. Academic Press, 2007.
- [51] R. Alfaro. Construction and operation of a small multiwire proportional chamber. In *Journal of Physics: Conference Series*, volume 18, page 362. IOP Publishing, 2005.
- [52] W. Blum, W. Riegler, and L. Rolandi. *Particle detection with drift chambers*. Springer Science & Business Media, 2008.
- [53] G. D. O’Kelley. *Detection and measurement of nuclear radiation*. Subcommittee on Radiochemistry, National Academy of Sciences-National Research Council, 1962.

- [54] R. Oliveira, V. Peskov, and P. Picchi. Further developments and tests of microstrip gas counters with resistive electrodes. *arXiv preprint arXiv:1101.3727*, 2011.
- [55] W. H. Toki. Review of straw chambers. Technical report, Stanford Linear Accelerator Center, 1990.
- [56] Vasiliki A Mitsou. The atlas transition radiation tracker. In *Astroparticle, Particle And Space Physics, Detectors And Medical Physics Applications*, pages 497–501. World Scientific, 2004.
- [57] E. Iarocci. Plastic streamer tubes and their applications in high energy physics. *Nuclear Instruments and Methods in Physics Research*, 217(1-2):30–42, 1983.
- [58] G. F. Knoll. *Radiation detection and measurement*. John Wiley & Sons, 2010.
- [59] F. Sauli. Principles of operation of multiwire proportional and drift chambers. Technical report, Cern, 1977.
- [60] F. Muleri, R. Bellazzini, A. Brez, E. Costa, F. Lazzarotto, M. Minuti, M. Pinchera, A. Rubini, P. Soffitta, and G. Spandre. X-ray polarimetry in astrophysics with the gas pixel detector. *Journal of Instrumentation*, 4(11):P11002, 2009.
- [61] T. Tanimori, A. Ochi, S. Minami, and T. Nagae. Development of an imaging microstrip gas chamber with a $5\text{ cm} \times 5\text{ cm}$ area based on multi-chip module technology. *Nuclear Instruments and Methods in Physics Research Section A: Accelerators, Spectrometers, Detectors and Associated Equipment*, 381(2-3):280–288, 1996.
- [62] F. Sauli and A. Sharma. Micropattern gaseous detectors. *Annual Review of Nuclear and Particle Science*, 49(1):341–388, 1999.
- [63] W. R. Leo. *Techniques for nuclear and particle physics experiments: a how-to approach*. Springer Science & Business Media, 2012.
- [64] J. B. Birks. *The theory and practice of scintillation counting: International series of monographs in electronics and instrumentation*, volume 27. Elsevier, 2013.

- [65] D. L Dexter. A theory of sensitized luminescence in solids. *The Journal of Chemical Physics*, 21(5):836–850, 1953.
- [66] K. A. Olive. Review of particle physics. *Chinese physics C*, 38(9):090001–090001, 2014.
- [67] S. O. Flyckt and C. Marmonier. *Photomultiplier Tubes: Principles & Applications*. 2002.
- [68] CMS collaboration et al. Performance of the cms drift tube chambers with cosmic rays. *Journal of Instrumentation*, 5(03):T03015, 2010.
- [69] NASA. Outgassing data for selecting spacecraft materials system. <https://outgassing.nasa.gov/>. Accessed: 13 August 2018.
- [70] L. Aliaga, L. Bagby, B. Baldin, A. Baumbaugh, A. Bodek, R. Bradford, W. K. Brooks, D. Boehnlein, S. Boyd, H. Budd, et al. Design, calibration, and performance of the minerva detector. *Nuclear Instruments and Methods in Physics Research Section A: Accelerators, Spectrometers, Detectors and Associated Equipment*, 743:130–159, 2014.
- [71] R. Asfandiyarov, P. Bene, A. Blondel, D. Bolognini, F. Cadoux, S. Debieux, F. Drielsma, G. Giannini, J. S. Graulich, C. Husi, et al. The design and construction of the mice electron-muon ranger. *Journal of Instrumentation*, 11(10):T10007, 2016.
- [72] e3d. Volcano hotend. <https://e3d-online.com/volcano-hotend>, 2019. Accessed: 12 August 2019.
- [73] Ninjatek. Ninjaflex. <https://ninjatek.com/ninjaflex/>. Accessed: 29 July 2019.
- [74] Taulman. Taulman 910 features. <http://taulman3d.com/910-features.html>. Accessed: 29 July 2019.
- [75] Polymaker. Store. <https://eu.polymaker.com/product/polymax-pla/>, 2019. Accessed: 29 July 2019.
- [76] G. Gilmore. *Practical gamma-ray spectroscopy*. John Wiley & Sons, 2011.

- [77] Takashi Nakagawa, Takuo Nakiri, Ryuichi Hosoya, and Yoshiro Tajitsu. Electrical properties of biodegradable polylactic acid film. *IEEE Transactions on Industry Applications*, 40(4):1020–1024, 2004.
- [78] COEX. *CX02 PLA Series 3D Printing Filament - Technical Data Sheet*. TSD Rev 1.0.
- [79] Sgx sensortech ec410 oxygen sensor. <https://www.sgxsensortech.com/>. Accessed: 29 June 2019.
- [80] Vgtlin Instruments GmbH. Red-y smart series, thermal mass flow meters and controllers, 2019. <https://www.voegtlin.com/en/mass-flow-meters-and-controllers-for-gases/red-y-smart-series/>. Accessed: 29 June 2019.
- [81] Analog.com. Ltpice - design center - analog devices, 2019. <https://www.analog.com/en/design-center/design-tools-and-calculators/ltpice-simulator.html>. Accessed: 19 July 2019.
- [82] L.G. Christophorou. Insulating gases. *Nuclear Instruments and Methods in Physics Research Section A: Accelerators, Spectrometers, Detectors and Associated Equipment*, 268(2):424 – 433, 1988.
- [83] H Schindler. Garfield++ ? simulation of ionisation based tracking detectors. <https://garfieldpp.web.cern.ch/garfieldpp/>, 2010.
- [84] P. R. Burchat, J. Hiser, A. Boyarski, and D. Briggs. Studies of helium gas mixtures in drift chambers. *Nuclear Instruments and Methods in Physics Research Section A: Accelerators, Spectrometers, Detectors and Associated Equipment*, 316(2-3):217–222, 1992.
- [85] G. Schultz, G. Charpak, and F. Sauli. Mobilities of positive ions in some gas mixtures used in proportional and drift chambers. *Revue de Physique Appliquée*, 12(1):67–70, 1977.
- [86] A. Peisert and F. Sauli. Drift and diffusion of electrons in gases: a compilation (with an introduction to the use of computing programs). Technical report, Cern, 1984.

- [87] H. Meier, U. Löffelmann, D. Mager, P. J. Smith, and J. G. Korvink. Inkjet printed, conductive, 25 μm wide silver tracks on unstructured polyimide. *physica status solidi (a)*, 206(7):1626–1630, 2009.
- [88] Conductive pla. <https://www.proto-pasta.com/pages/conductive-pla>. Accessed: 01 Sep 2016.
- [89] Developer’s kit. <http://www.voxel8.co/printer>. Accessed: 24 Aug 2016.
- [90] Proto Plant. *CDP!xxxx Composite Conductive Fibre PLA - SafetyData Sheet*. Date of Issue: 05 Oct 2018.
- [91] L. Shen, Z. D. Lou, and Y. J. Qian. Effects of thermal volume expansion on positive temperature coefficient effect for carbon black filled polymer composites. *Journal of Polymer Science Part B: Polymer Physics*, 45(22):3078–3083, 2007.
- [92] L. Nikiel, H. Yang, M. Gerspacher, and G. Hoang. Electrical resistivity and thermal expansion coefficient of carbon black filled compounds around tg. *Kautschuk Gummi Kunststoffe*, 57(10):538–540, 2004.
- [93] Filastruder. Filastruder: The world’s premier diy filament extruder/maker, 2019. <https://www.filastruder.com/>, 2019.
- [94] M. Worzakowska. Thermal and mechanical properties of polystyrene modified with esters derivatives of 3-phenylprop-2-en-1-ol. *Journal of Thermal Analysis and Calorimetry*, 121(1):235–243, 2015.
- [95] J. Csernica and A. Brown. Effect of plasticizers on the properties of polystyrene films. *Journal of chemical education*, 76(11):1526, 1999.
- [96] B. L. Funt and A. Hetherington. The influence of chain length on the luminescent output of plastic scintillators. *The International Journal of Applied Radiation and Isotopes*, 4(3-4):189–195, 1959.
- [97] Blb industries - the box, large 2. <https://blbindustries.se/the-box-large-2/>. Accessed: 01 Mar 2020.
- [98] Tractus3d - t2000. <https://tractus3d.com/products/t2000#specsheat>. Accessed: 01 Mar 2020.

- [99] Wasp - delta wasp 2040 turbo2. <https://www.3dwasp.com/en/fast-3d-printer-delta-wasp-2040-turbo2/>. Accessed: 01 Mar 2020.
- [100] 3d printed electronics - aerosol jet technology. <https://optomec.com/printed-electronics/aerosol-jet-technology/>. Accessed: 01 Mar 2020.